# Investigating the impact of onion-like carbons on the supercapacitance of $Ti_2CT_X$ MXene


Irfan Habib

February 23, 2019

# Dedications

This dissertation is dedicated to my loving family, my Mom Fatima and my Dad Adam, and to my brother Zidaan for all the love and support they showed me throughout this MSc. Their support and advice both kept me grounded and helped me persevere when the going got rough. To Sabica for being so patient, loving and understanding, I know having a boyfriend who spends many a weekend in the labs is not easy! And finally a big thanks to my friend Yusuf for his constructive criticism and many (ill-advised) late nights of gaming, who, despite losing his bet with me, still featured in this dedication.

# Acknowledgements

There are so many people whom I need to thank for their assistance with this dissertation that I am terrified of leaving out someone's name, but I'll give it a go.

First of all, prior to this dissertation I had zero experience in the field of Materials Science, despite having a passion for the energy science field. My background is in Physics and Astrophysics, so I was diving head first into a field which I knew nothing about, and I want to start by giving a many hats off to Dr Phil Ferrer, my supervisor from the Wits School of Physics, and Prof Ken Ozoemena, my co-supervisor from the School of Chemistry, for sticking it out with me. Their input and gentle (and sometimes not so gentle) nudging was instrumental to me completing my MSc in the reduced time I had set for myself. A big thank you for this.

The Ozoemena research group really welcomed me to their family with open arms and I want to thank every single one of the students and post docs who I had the fortune of engaging with throughout this MSc. Special mention goes to Rasmita who was the post doc assigned to helping me get my feet under me in a completely new workspace. You were brilliant at just about everything, and your (strict!) lessons are one of the main reasons I was able to complete this MSc. To Thokozani and Thapelo for sufferring through the trenches with me as part of the newbie supercapacitor group, we had quite a year. To Patric, the only other physicist in the group, thanks for the solidarity in our attempts to convert the chemists to Python. To Nkosi, Lesego, Aderemi, Adewale, Suhail, Siwa, Refiloe, and Itumeleng, thank you so much for all the banter, fun, and the lots and lots of help you all gave me. Suhail I am sorry but there will be no one else sharing the blame for missed lab clean ups anymore!

I also found an unexpected kinship with the crystal physics group within the School of Chemistry. Thank you to Prof Dave and Dr Caren Billing for the many chats and philosophising, and of course all the XRD and electrochemistry assistance! A special mention to Adam and Sikhumbuzo for kind words and always being there to complain to!

I would also like to thank Prof Ray Sekhar from the UNISA Department of Physics for taking the XPS measurements that are present in this work.

Finally a little closer to home, many thanks to Prof Naidoo, Prof Keartland, and Gerard for all the administrative help! A big thanks to Prof Bhattacharyya from the Nanotransport Lab within the School of Physics for letting me use their Electron Microscope. Special mention goes to Siphe for the many hours spent assisting me with taking images and teaching me to use the instrument.

I will be a very fortunate individual if I manage to keep even a tenth of these friendships and connections alive in the years to come. I am truly grateful to everyone on this list, and to those not on it, for all the kindness and friendship you have shown me this past year.

# Contents

# List of Figures

# List of Tables

# List of Acronyms

| | |
|---|---|
| **2D** | two dimensional |
| **Al** | aluminium |
| **BET** | Brunauer–Emmett–Teller |
| **C** | carbon |
| **CD** | constant current charge/disharge |
| **CV** | cyclic voltammetry |
| **DMF** | dimethyl fluoride |
| **EDL** | electric double layer |
| **EDLC** | electric double layer capacitor |
| **EIS** | electrochemical impedance spectroscopy |
| **ESC** | equivalent series circuit |
| **ESR** | equivalent series resistance |
| **F** | fluorine |
| **GC** | Guoy-Chapman |
| **HCl** | hydrochloric acid |
| **HF** | hydrofluoric acid |
| **LHS** | left hand side |
| **LiF** | lithium fluoride |
| **MAX** | material with the chemical formula $M_nAX_{n-1}$ |
| **MNR** | MXene nanoribbon |
| **MNS** | MXene nanosheet |
| **MX** | Mxene |
| **ND** | nanodiamond |
| **NMP** | N-methyl-2-pyrrolidone |
| **O** | oxygen |
| **OH** | hydroxyl |
| **OLC** | onion like carbons |
| **PC** | pseudocapacitor |
| **PVDF** | polyvinylidene fluoride |
| **PZC** | point of zero charge |
| **SC** | supercapacitor |
| **SEM** | scanning electron microscopy |
| **SFC** | split flat cell |
| **SSA** | specific surface area |
| **TEM** | transmission electron microscopy |
| **Ti** | titanium |
| **XPS** | X-ray photoelectron spectroscopy |
| **XRD** | X-ray diffraction |

# Abstract

Increasing energy demands in contemporary society have driven research in energy storage to create devices which emphasize both energy density and power density. The supercapacitor is a key example of such a device. It is a broad category of devices that occupies the middle ground between batteries and capacitors. The purpose of this work is to present a detailed understanding of supercapacitors via an investigation into a new class of 2D materials called MXenes as an active electrode material for supercapacitor applications. More specifically, the titanium carbide MXene, $Ti_2C$, was investigated as a supercapacitor active material, as well as the influence of another nanomaterial, carbon onions or onion-like carbons (OLCs), as a dopant. The materials were characterised by a number of physical techniques; including X-ray Diffraction (XRD), Raman Spectroscopy, Scanning Electron Microscopy (SEM), Transmission Electron Microscopy (TEM), X-ray Photoelectron Spectroscopy (XPS), and Brunauer–Emmett–Teller surface area analysis (BET). The materials were also characterised using electrochemical techniques such as Cyclic Voltammetry, Constant Current Charge/Discharge, and Electrochemical Impedance Spectroscopy. It was found that the introduction of OLCs into the layered MXene structure increases the long term cycling stability of the material from $\sim 80\%$ to $> 95\%$ when used in 5% and 10% weight percentages. It was also found to increase the supercapacitance of the MXene in the 5% quantity from $\sim$ 104 F/g to $\sim$ 148 F/g, but decreased the supercapacitance in the 10% quantity from $\sim$ 104 F/g to $\sim$ 92 F/g. This power and energy density also improved in the 5% OLC doped sample compared to the pristine sample for current densities between 0.5 A/g and 5 A/g. Overall, this study showcased the ability of OLCs to improve electrochemical performance of a $Ti_2C$ based supercapacitor.

# Chapter 1

# Introduction

## 1.1 Landscape of Energy Storage

The African continent, and more generally the developing world, is plagued by deficiencies in many areas; health care, good governance, civil infrastructure, connectivity, security, clean water, and energy to name a few. Of these, energy access can be considered to be an enabling factor. Having access to energy paves the way to have access to many of the other areas listed above, and similarly not having access to energy removes the possibility of achieving success in the same areas. As such, research in energy technologies is key in order to enable inclusive development in the developing world. This is supported by the fact that energy is indicated as a national priority for development in most countries, both developed and developing. 'Affordable and clean energy' and 'Sustainable cities and communities' are also two of the United Nations Sustainable Development Goals, furthermore emphasizing the importance of research in the energy sciences.

In addition to this, the 21st century has been marked by the exponential growth of technology. Recent advancements in numerous fields, including artificial intelligence, big data, robotics, aeronautics, electric smart grids, and many more, are all key examples of this extremely rapid technological advancement. Many of these advancements are strongly correlated with another, and one of these key linkages is a strong dependence on energy availability. As our capacity to do more with our technology increases, so too does the energy we need to power our devices. Figure 1.1 illustrates this point by depicting the battery capacity of progressive Samsung Galaxy smartphone models. From the time of release of its first model in 2010 to the current latest model in 2018, the battery capacity has increased by 2000 mAh, an increase of over 130%. Even though this analysis is simplistic, as there are other factors to consider such as slimmer form factors and smarter use of processing power in modern phones which can explain the plateau in energy capacity from 2016 to 2018, it still demonstrates the steep rise of necessary energy capacity with an example that is easily accessible.

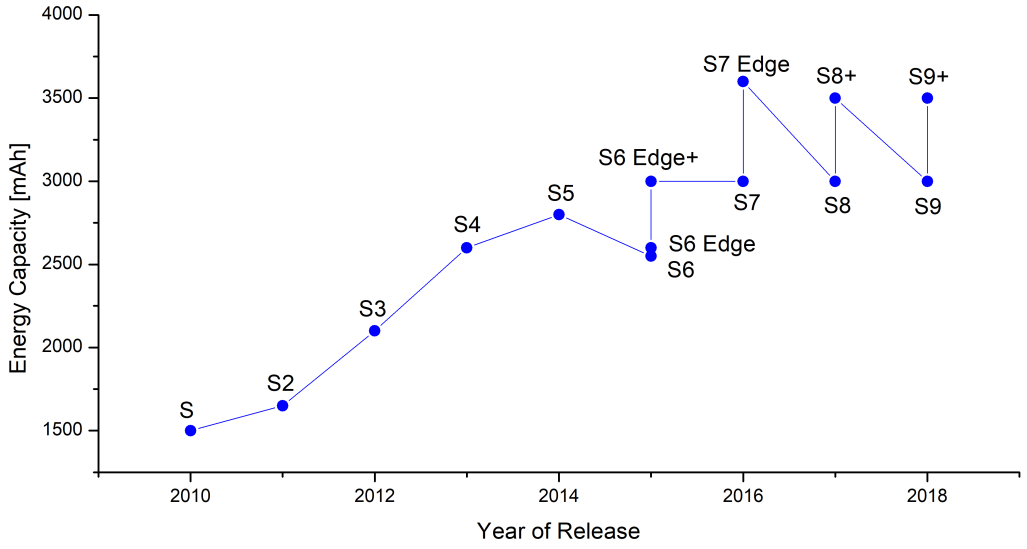


Figure 1.1: Battery capacity trend of subsequent Samsung Galaxy smartphone models [1].

Here it becomes important to distinguish between energy capture and energy storage. Energy capture refers to systems which work on converting energy from nature into a form which is useful for society, for example photovoltaic systems (like solar farms) which convert sunlight into electricity. Energy storage deals with what comes next. In renewable energy systems, it is often necessary for this energy to be transferred to a storage system, like an energy reservoir, before being transmitted along the main grid to households or other nodes of consumption. This is because sometimes renewable sources cannot always be relied on for a constant supply. For example, a solar farm can only capture energy during the day, and at night will effectively capture no energy. These storage processes vary widely and often involve converting the energy captured into another form, usually chemical. The focus of this dissertation will be on energy storage.

When dealing with an energy storage system, it is necessary to distinguish between energy density and power density. Energy density relates to how much energy a system can store per some normalisation constant like mass or volume, whereas power density is how quickly this energy can be charged or discharged (again normalised). In addition to an increasing demand for energy capacity in most modern systems or devices, there is also an increasing demand for having higher power systems. Again we can return to the smartphone for an example of this. Consumers want phones that charge faster and last longer. The charging faster part of this relates to the need for increased power density in energy storage materials, and the lasting longer part relates to an increased energy density of these materials. We can use these two measures of storage to plot a Ragone plot (Figure 1.2), which allows us to visualise the landscape of the energy storage devices.

In Figure 1.2 we can see that energy dense storage devices like fuel cells and batteries typically have poorer power densities. This means that devices which store a lot of energy are typically have much slower charge and discharge times. On the other hand, devices on the power dense storage devices like capacitors have extremely high power densities, but have very low energy densities. This means that devices which can charge and discharge very fast usually cannot store a significant amount of energy. There is a class of devices which occupy the region in between, however. These are supercapacitors, also sometimes called ultracapacitors. They are neither as energy dense as batteries nor as power dense as capacitors, however, they a significantly more energy dense than capacitors and more power dense than batteries. This makes them useful in many fields; power machinery like forklifts or lifts, automotives, smart grid control, and capturing peak flows in renewable energy systems.

The aim of this dissertation is to successfully create a 2D material, the MXene $Ti_2C$ which has undergone onion-like carbon doping, which exhibits sufficient electrochemical performance to function as the active material in a supercapacitor. This investigative process will also assist in the understanding of energy

storage mechanisms within supercapacitors.

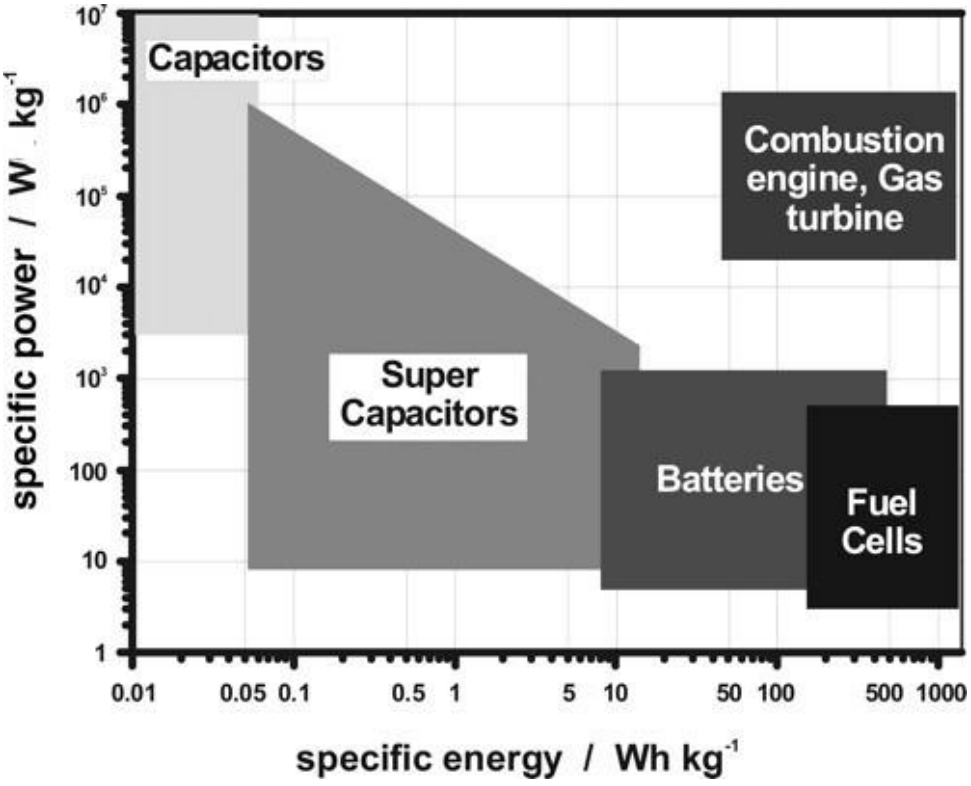


Figure 1.2: Ragone plot of various different energy storage technologies [2]

## 1.2 Supercapacitors

Supercapacitors are essentially capacitors with a significantly larger capacitance. Standard capacitors range from picofarads to microfarads, but supercapacitors can go up to a couple thousand Farads [3]. There are two key physical processes which are responsible for this vastly superior capacitance; the Electric Double Layer (EDL) effect which occurs at the interface between an electrode material and the electrolyte, and Pseudocapacitance which is the faradaic storage of charge at the electrode surface. There are many different types of supercapacitors but they can generally be grouped into three categories, shown in Figure 1.3, depending on which physical process dominates the charge storage:

1. Electric Double Layer Capacitors (EDLCs)
2. Pseudocapacitors (PCs)
3. Hybrid or asymmetric capacitors

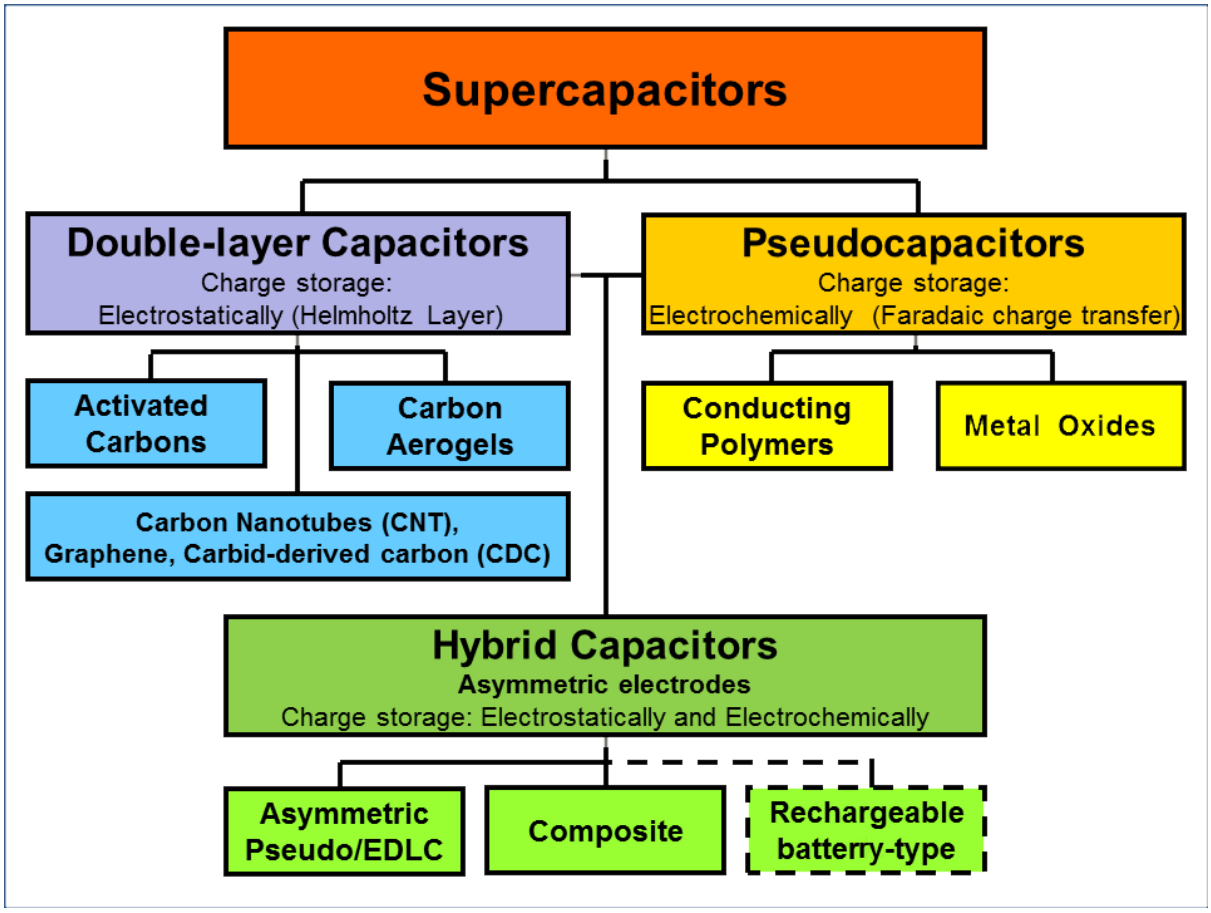


Figure 1.3: Different categories of supercapacitors.

Broadly speaking, every supercapacitor utilises both the EDL and pseudocapacitance, however, one process is usually dominant in the case of EDLCs and PCs [3]. Before we dive into detail regarding these categories, however, it will be useful to go through some capacitor basics.

### 1.2.1 Capacitors

A conventional capacitor consists of two parallel plates. When connected to some current source, a charge will build up on one plate and an equal but opposite charge on another. A charge build-up on the plates results in the increase of an electric field between them. Eventually the potential buit up between the plates wil be equivalent to the potential of the power supply, and current will cease to flow. The ratio between the charge on the plates and the potential between the plates is called capacitance:

$$C = \frac{Q}{V} = \frac{\epsilon_0 \epsilon A}{d} \tag{1.1}$$

where Q is the magnitude of the charge on each plate, V is the voltage across the plates, $\epsilon_0$ is the permittivity of free space and $\epsilon$ is the permittivity of the material, and $d$ is the separation distance between the two plates. Equation 1.1 is true for parallel plate capacitors only.

Often, a material is inserted between the plates. This is illustrated in Figure 1.4. Usually this can be a polar material (a dielectric), or an electrolytic solution (or solid).

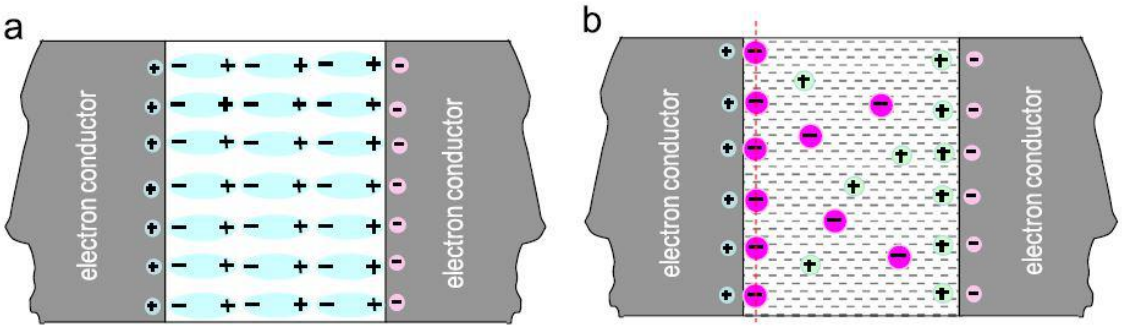


Figure 1.4: Illustration of a) dielectric and b) electrolytic media in electrochemical capacitors [4].

In the dielectric case (a) the electric field set up by the immobile polar molecules will oppose the external field applied by the plates, resulting in a weaker net electric field between the plates. This will decrease the voltage between the plates, and thereby increase the capacitance as per the above equation.

In the electrolytic case, the plates attract an opposite charge. An electric double layer is set up at the electrode interface; the process through which capacitance is realised in this case is slightly more complicated than the dielectric case and will be discussed in the next section. However, in a liquid electrolyte solution we can see that we can achieve a greater charge density at the electrode/electrolyte interface than at the electrode/dielectric interface due to the mobility of ions in solution vs the immobile polar molecules in a dielectric. We will see in the next section that supercapacitors are usually of this type[4].

There are a number of useful parameters to look at to assess the performance of a capacitor, and these will hold for a supercapacitor as well. These are[3]:

- Specific Capacitance
- Operating Voltage
- Energy Density
- Power Density
- Equivalent Series Resistance
- Time constant

The specific capacitance of a capacitor is simply the total capacitance divided by some normalisation constant. In this dissertation we will use the mass of our sample for our normalisation constant:

$$C_S = \frac{C_T}{m}$$

where $C_S$ is the specific capacitance and $C_T$ is the total capacitance. It is useful to use normalised parameters since different publications often use different mass loadings during their experiments.

The energy in a capacitor is stored in the electric field between the plates. When a voltage is applied to the capacitor, it takes a small amount of work dW to move a charge dQ on to the plate:

$$dW = V \cdot dQ$$

If we assume no or insignificant heat loss to occur, then dW is also the energy stored in the electric field set up by the charge on the plate. We can also replace the voltage term V with the expression from the Equation 1.1:

$$dW = \frac{Q}{C} dQ$$

This means that the total energy is given by the following integral:

$$W = \int dW = \int_0^Q \frac{Q}{C} dQ = \frac{1}{2}\frac{Q^2}{C} = \frac{QV}{2} = \frac{CV^2}{2}$$

It is useful to express the energy stored by the capacitor in terms of C and V since these are readily available experimental quantities, as opposed to charge which is often hidden away in the current term. If we look at the above expression it is clear that the energy stored in a capacitor is dependent on the voltage applied across it. There is always a limit on the system, however. There is a maximum voltage $V_0$ that can be applied to the system and is determined by the dielectric used, after which the dielectric will break down and/ or a short circuit will occur. This $V_0$ is also called the operating voltage or the potential window. The maximum energy stored on the system is therefore given by

$$W_{max} = \frac{C_T V_0^2}{2}$$

and conversely the maximum energy density is found by using the specific capacitance as opposed to the total capacitance:

$$E_D = \frac{C_S V_0^2}{2}$$

The power output for a capacitor can be found by dividing the total energy by the discharge time t, and this discharge time is dependant on discharge current of the system. The peak or maximum output is found by using the shortest discharge time:

$$P = \frac{W}{t} = \frac{C_T V_0^2}{2t}$$

The problem with the above equation is that we cannot derive the shortest discharge time using any equations mentioned thus far. The next useful parameter which can assist with this problem is the equivalent series resistance $R_{ES}$ which can allow us to derive an expression for the peak or maximum power output. Any power source connected to a load will have an internal resistance that can be modelled by placing a resistor in series with that source, so the total resistance in a circuit will be $R = R_{ES} + R_L$, where $R_L$ is the resistance of the load. The power delivered to the load is then $P = I^2 R_L$, and $I$ is the total current in the circuit and is equivalent to $\frac{V}{R}$. Putting these two expressions together will give the following expression:

$$P = \left(\frac{V_0}{R}\right)^2 \cdot R_L = \frac{V_0^2 R_L}{(R_L + R_{ES})^2}$$

It is clear from the above equation that the maximum power occurs when $R_L = R_{ES}$:

$$P_{max} = \frac{V_0^2 R_{ES}}{4R_{ES}^2} = \frac{V_0^2}{4R_{ES}}$$

And the maximum power density is then given by:

$$P_D = \frac{V_0^2}{4R_{ES}m}$$

Assuming the model of an RC circuit gives the following relationship between the supply voltage and the voltage across the capacitor:

$$V_{supply} = V_{capacitor} \cdot e^{\frac{t}{\tau}}$$

where the time constant $\tau$ is given by:

$$\tau = R_{ES} C_T \tag{1.2}$$

This gives us an idea of the responsivity of the cell. At time $t = \tau$ the voltage across the capacitor would have changed by 36.8%, and at $t = 4\tau$ the voltage would have changed by 98%.

### 1.2.2 Electric Double Layer Capacitors

Now that we have some understanding of the standard behaviour of capacitors we can discuss Electric Double Layer Capacitors (EDLCs).

The double layer capacitance is best explained by considering the evolution of the three models which arose to detail it: Helmholtz model, Guoy-Chapman Theory, and the Stern modification [5].

An EDL in a supercapacitor is the structure that forms when a working potential is applied across an electrode and an adjacent electrolyte. The Helmholtz model assumed that given that the electrode is a good conductor, that the charge would all lie on the electrode surface giving rise to the surface charge $\sigma_e$. He assumed that this would create a plane of counter charge in the solution, giving rise to two layers of equal but opposite charge, i.e. the double layer. The surface charge density is given by:

$$\sigma_e = \frac{Q}{A} = \frac{CV}{A} = \frac{\epsilon\epsilon_0 AV}{(d)(A)} = \frac{\epsilon\epsilon_0 V}{d}$$

In this discussion it is convenient to denote a differential capacitance, $C_d$, given by:

$$C_d = \frac{\partial\sigma_e}{\partial V} = \frac{\epsilon\epsilon_0}{d}$$

This model leads to the implication that the differential capacitance is constant with potential in a supercapacitor, as it is in an ideal capacitor, however experiments invalidate this implication. This can be seen in Figure 1.5.

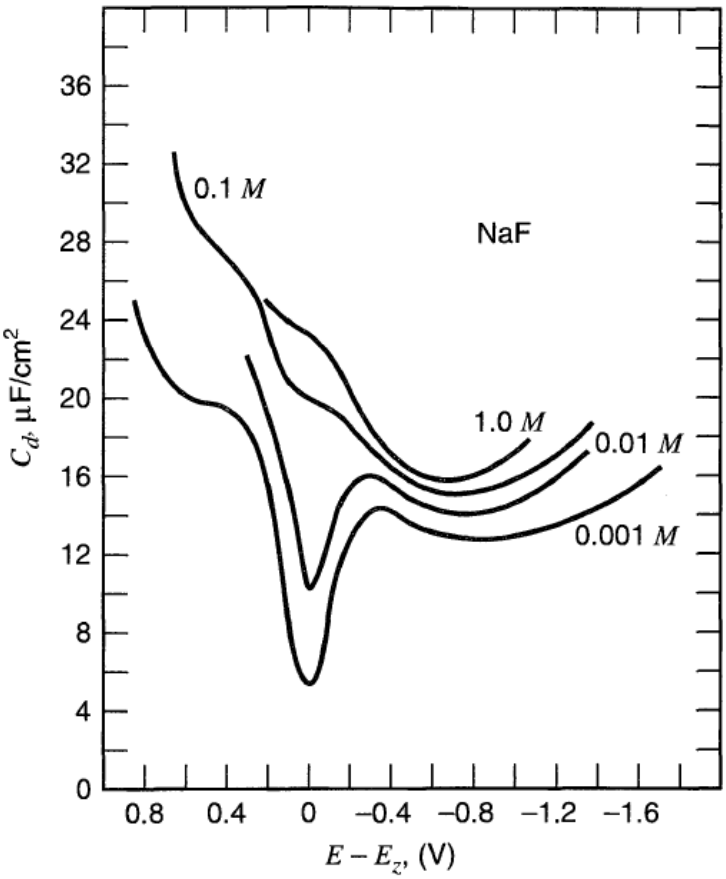


Figure 1.5: Differential capacitance vs. potential for NaF solutions in contact with mercury at 25°C. Taken from [6].

The failure of this model is that it assumes the solution charge all resides in a single layer, but neglects that the ions in solution form a potential distribution that varies with distance from the electrode.

The Guoy-Chapman Theory proposed that we consider a diffuse layer to explain the potential distribution in the solution. The derivation is protracted but we will summarise the theory here. The potential function they proposed for a symmetric electrolyte (containing one anodic and one cathodic ion species) is given by:

$$\frac{d\phi}{dx} = -\Big(\frac{8kTn^0}{\epsilon\epsilon_0}\Big)^{1/2} sinh\Big(\frac{ze\phi}{2kT}\Big)$$

where $\phi$ is the potential profile of the solution, $k$ is the Boltzmann constant, $T$ is the temperature of the solution, $n^0$ is the bulk concentration of the ionic species (same for both anodic and cathodic species), $z$ is the atomic number of the ion and $e$ is charge of an electron.

Through this potential function we can find an expression for the surface charge density and given the potential at the electrode $\phi_0$ we can calculate the differential capacitance:

$$C_d = \frac{d\sigma_e}{d\phi_0} = \Big(\frac{2z^2e^2\epsilon\epsilon_0 n^0}{kT}\Big)^{1/2} cosh\Big(\frac{ze\phi_0}{2kT}\Big) \tag{1.3}$$

This model predicts the trend depicted in Figure 1.6.

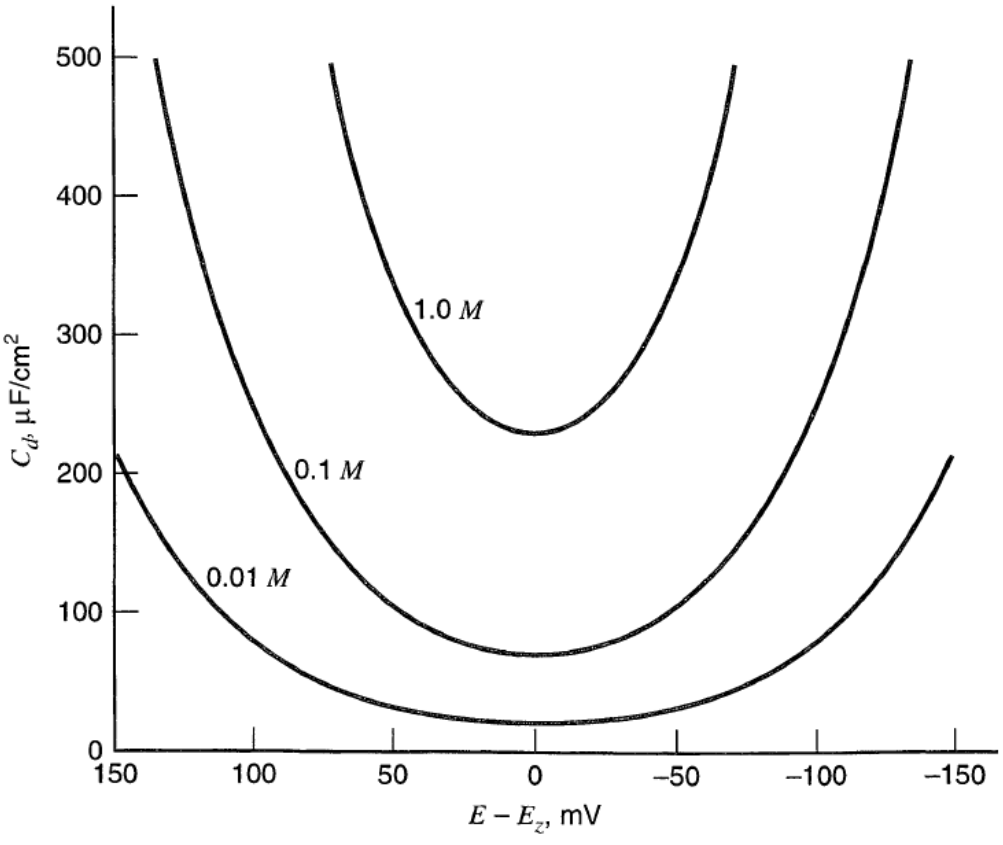


Figure 1.6: Predicted differential capacitances from the Gouy—Chapman theory. Calculated from Equation 1.3 for the indicated concentrations of a 1:1 electrolyte in water at 25°C. Note the very restricted potential scale. The predicted capacitance rises very rapidly at more extreme potentials relative to $E_Z$. Taken from [5].

This shows an improvement over the Helmholtz model, particularly at the point of zero charge (PZC, 0 on the x axis) and at low concentrations. but still fails to predict the correct capacitance. The differential

capacitance predicted is too high, and it rises steeply at regions close to the electrode surface. This is because the model fails to take into account the finite size of ions.

The Stern model takes this into account by assuming a plane of closest approach at $x = x_2$, called the outer helmholtz plane, and effectively combines the helmholtz model from $x = 0$ to $x = x_2$, and the GC model from $x_2$ onwards. It assumes that the differential capacitance is given by two capacitors in series, one given by the Helmholtz model and the other by the GC model. This is more clearly depicted in Figure 1.8. The differential capacitance is given by Equation 1.4 and is illustrated in Figure 1.7. The Stern modification is still does not perfectly reproduce the experimental findings found in Figure 1.5, however, provides the basic foundation upon which system specific modifications should be made. Examples of these include the structure of the dielectric in the compact layer, saturation of that dielectric in the strong interfacial field, and solution differences for anionic and cationic excesses, to name a few [5].

$$C_d = \frac{(2\epsilon\epsilon_0 z^2 e^2 n^0/kT)^{1/2} cosh(ze\phi_2/2kT)}{1 + (x_2/\epsilon\epsilon_0)(2\epsilon\epsilon_0 z^2 e^2 n^0/kT)^{1/2} cosh(ze\phi_2/2kT)} \tag{1.4}$$

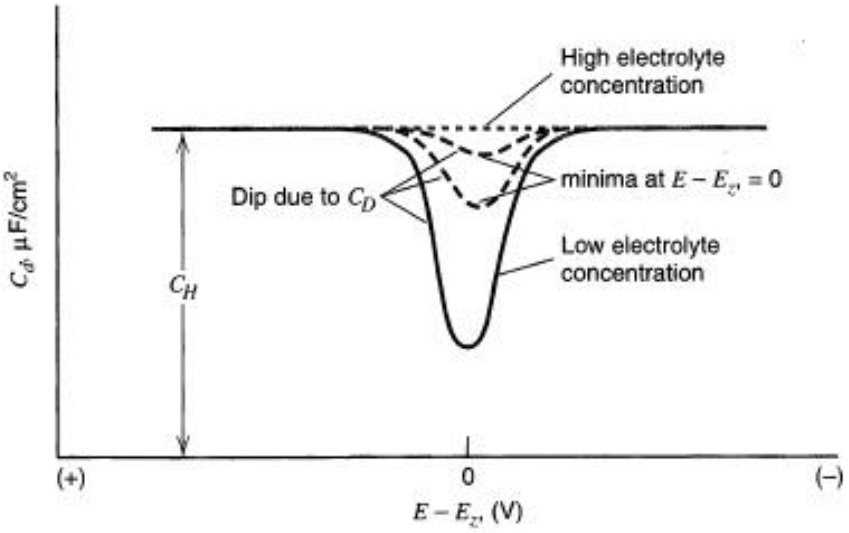


Figure 1.7: An illustration of Equation 1.4, which produces a differential capacitance constant with voltage at higher ionic concentrations, and with a symmetric peak at lower concentrations at the PZC, as expected. Taken from [5].

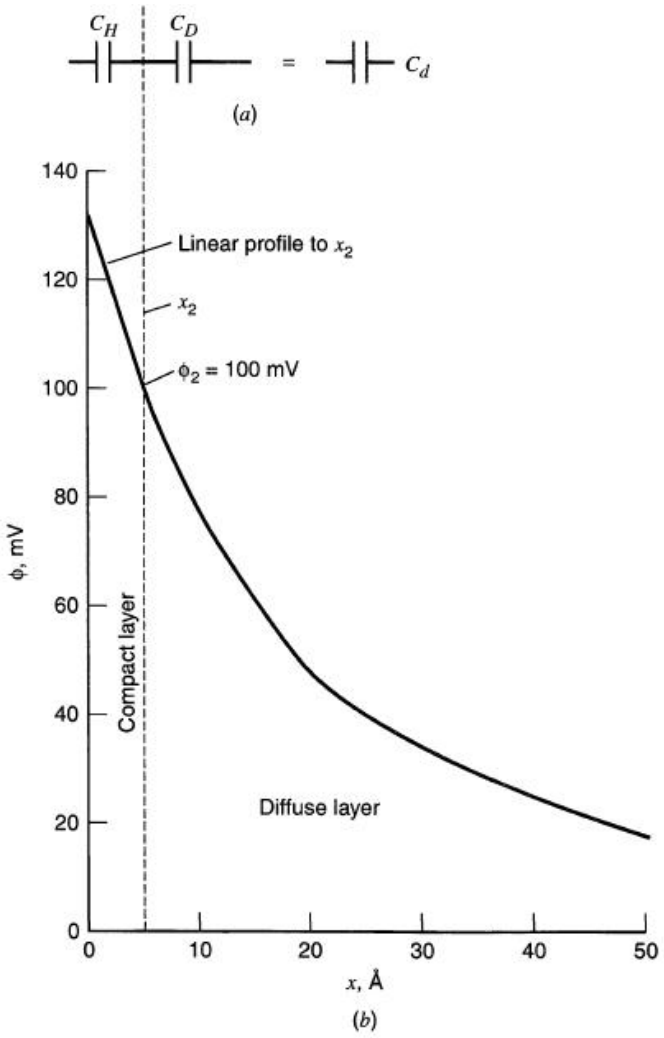


Figure 1.8: (a) A view of the differential capacitance in the Gouy—Chapman—Stern (GCS) model as a series network of Helmholtz-layer and diffuse-layer capacitances. (b) Potential profile through the solution side of the double layer, according to GCS theory. Calculated from Equation 1.4 for $10^{-2}$M electrolyte in water at 25°C. Taken from [5].

Figure 1.9 summarises the physical picture in each of the three models.

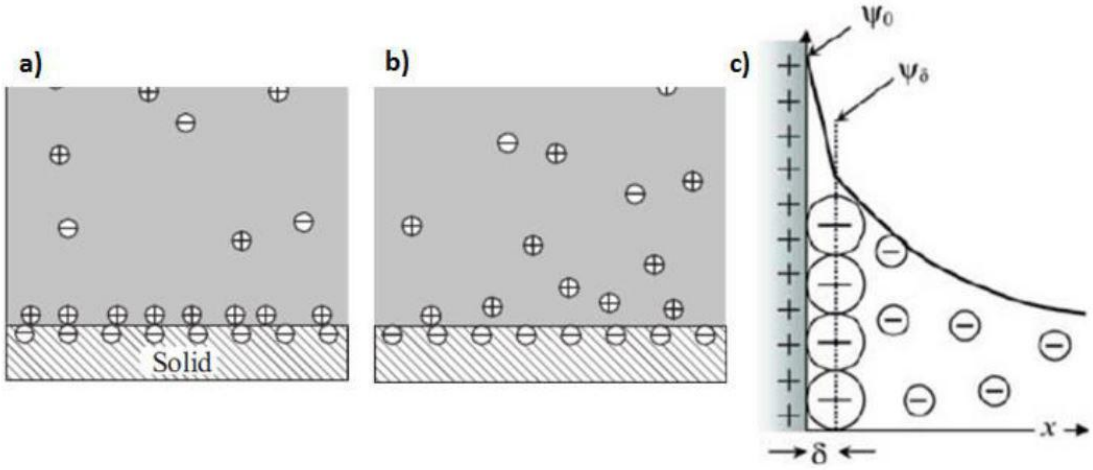


Figure 1.9: The system of the Electric Double Layer assmed for a) the Helmholtz model, b) the Guoy-Chapman theory, and c) the Stern modification. Taken from [7].

### 1.2.3 Pseudocapacitors

As mentioned earlier, capacitance in supercapacitors arises from two factors, the electric double layer (Section 1.2.2), and pseudocapacitance. This is the term given to any charge accumulation that occurs through faradaic processes. As there are many such processes which can occur, we will treat it quite generally. Faradaic processes can occur in the operation of a supercapacitor, as ions in the electrolyte within the OHP also act as electron donors and transfer electrons to the electrode atoms. This results in a faradaic current and result in charge being transferred from the solution to the electrode (or vice versa), and are often a function of electrode potential. This creates a derivative $dQ/dV$ which has the mathematical structure of capacitance but not the same physical origin, i.e. it is not the potential dependant accumulation of electrostatic charge, and hence it is called pseudocapacitance [8]. Common faradaic processes include the following:

- Redox reactions: when electron transfer occurs between ions, changing the oxidation states of involved ionic species.
- Electrosorption processes: when electrons leave an ionic species and adsorb to the electrode surface
- Intercalation of ions: when ions manouever in between layers of the electrode lattice and adsorb onto active surfaces in the electrode bulk.

### 1.2.4 Hybrid Capacitors

In general EDLCs display excellent power densities but poor energy densities due to the limited available surface area of the active materials. PCs usually display much better energy densities, but often cannot reach the same power density because the faradaic charge storage mechanism is not as fast as the electrostatically governed EDL effect. In an attempt to obtain the best of both worlds there have been many instances of published research investigating supercapacitors which have one EDLC electrode and the other a faradaically governed electrode like those used in a PC or even a battery [9].

Figure 1.10 summarises the processes which lead to observed capacitance in supercapacitors: A and B are examples of EDL storage mechanisms, and C and D are examples of faradaic mechanisms. C is the redox reaction of $RuO_2$, and D is the intercalation of Li ions.

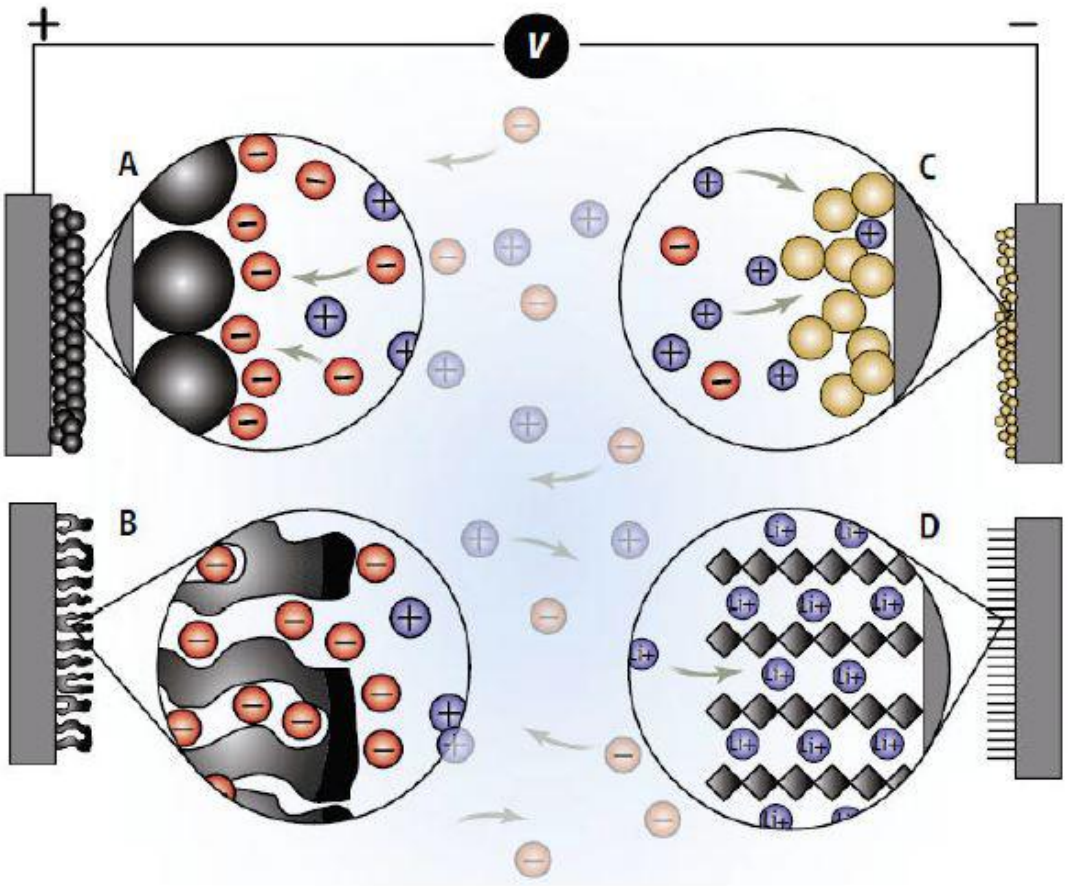


Figure 1.10: A and B are examples of EDL storage mechanisms, and C and D are examples of faradaic mechanisms. C is the redox reaction of RuO2, and D is the intercalation of Li ions. Taken from [7].

In this dissertation these concepts will be applied to understanding the electrochemical and physical processes which allow the MXene $Ti_2C$ to function as an active material in a supercapacitor.

# Chapter 2

# Literature Review

MAX phases and their corresponding MXenes have been much studied in academic institutions around the world, however, the specific MXene $Ti_2C$ has not benefitted from this academic interest as much as other MXenes. Nevertheless, it is worth discussing the current research on general MXenes as much of it is relevant to $Ti_2C$. Onion-like carbons (OLCs) are also a material which, until the last decade or so, have not been well studied despite being a known carbon nanostructure [10]. Both MXenes and OLCs have shown great potential for good electrochemical performance in the literature, and it is worth familiarising ourselves with the current research.

## 2.1 MXenes

MXenes are a family of 2D-like materials derived from MAX phases. The MAX phase structure is $M_nAX_{n-1}$, where M is an early transition metal, A is a group 13 or 14 element, X is carbon (C) or nitrogen (N), and n ranges from 1 to 3. The A group element is etched out to create a MXene with the following formula: $M_nX_{n-1}$. MXenes are given their name because of their 2D-like structure being reminiscent of graphene. MXenes typically exhibit good conductivity, and such has over the last few years attracted much interest in its electrical properties. Current applications under investigation are gas adsorption, electronics, sensors, catalysts, with a big focus in energy storage materials. The first MXene discovered was $Ti_3C_2$ and this was done by Yuri Gogotsi and his group at Drexel University, with the first paper on the topic being published in 2011 [11].

In this dissertation the specific MXene of focus will be $Ti_2C$, made from the MAX phase $Ti_2AlC$. However, due to much of the focus of research being on the heavier MXene $Ti_3C_2$ the discussion will also sometimes use it as an example. Whenever the term MXene is used in this dissertation it can be assumed that the author is referring to $Ti_2C$, unless otherwise stated.

### 2.1.1 MAX Phase Structure

There are around 60 pure MAX phases currently known, and different synthesis procedures can yield different combinations of M, A, or X elements in a single MAX phase, for example having $Ti_3(Al_{0.5}, Si_{0.5})C_2$, so this number can be increased even further[12].

Figure 2.1 illustrates the typical MAX phase structure for different values of n. The M and X elements form sandwich like layers which are interleaved with A group elements. The MAX phases are hexagonal and have $P6_3/mmc$ symmetry. The X elements are situated at octahedral sites in the lattice and are bonded directly to the M group elements through a mixture of ionic, covalent, and metallic bonds. The A group element is bonded directly to the M group element through a metallic bond. This means that while both bonding mechanisms are relatively strong, the M-X bonds are much stronger than the M-A bonds[12].

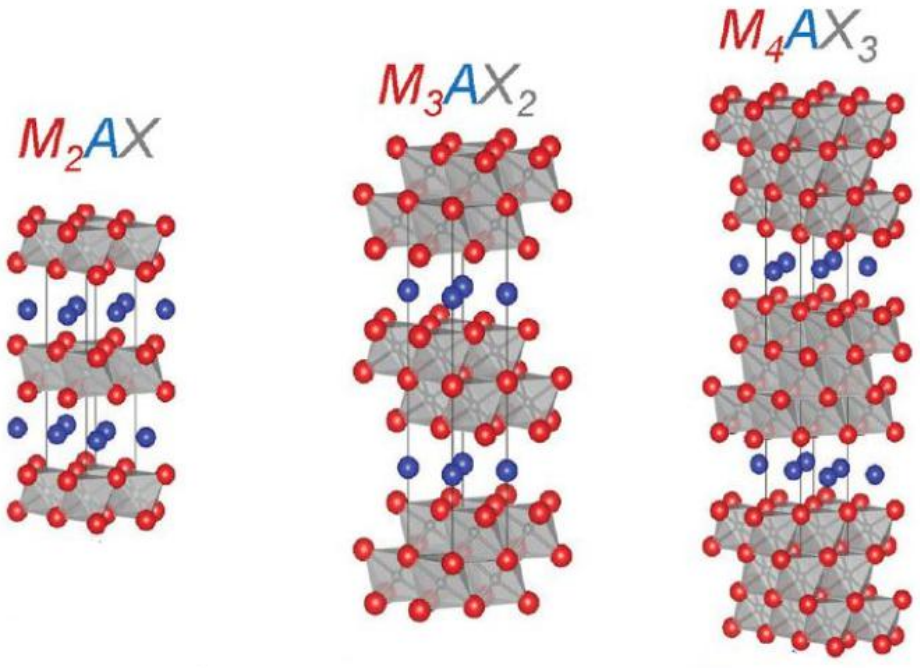


Figure 2.1: Illustration of the structure of MAX phases for n values 1-3. Red dots are the M elements, blue dots are the A elements, and grey dots are the X elements. Taken from [12].

### 2.1.2 Synthesis: MAX to MXene

Standard synthesis procedures involve using a strong etchant like hydrofluoric acid to remove A group elements from the precursor MAX phase. Figure 2.2 demonstrates this process for the MAX phase $Ti_2AlC$. This is possible because of the relative strength difference in the M-A and M-X bonds discussed in the previous section. Since they are both quite strong they cannot be removed via mechanical means like stretching or shearing forces. Instead a chemical agent, usually hydrofluoric acid (HF), is used to break the M-A bonds, while leaving the M-X bonds intact. It should be noted that the concentration of HF etchant needed is dependent on the strength of the M-A bonds in the MAX phase. For example, the energy of the M-A bond in $Ti_2AlC$ is 0.98 eV and in $Nb_2AlC$ is 1.21 eV. The ideal etching conditions for $Ti_2AlC$ is 10% HF concentration for 10 hours, while for $Nb_2AlC$ is 50% concentration for 90 hours. The higher bond energy requires a stronger etchant, hence the higher concentration and etching time. If $Ti_2AlC$, for example was to be etched at 50% concentrated HF it would completely dissolve in solution [12].

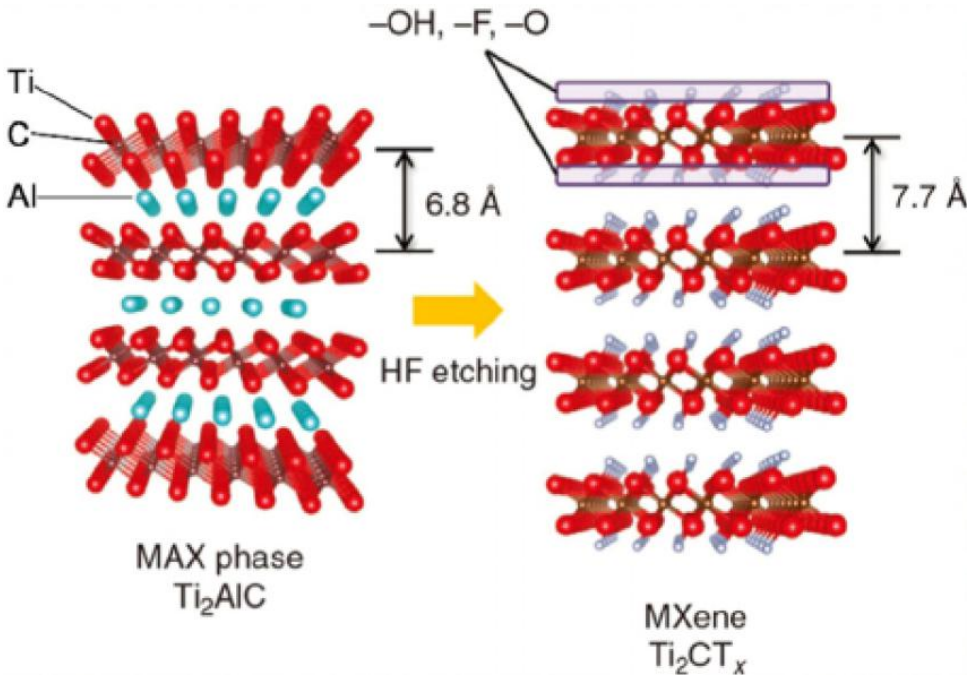


Figure 2.2: Illustration of the etchng process of $Ti_2AlC$, depicting the removal of Al atoms in the presence of HF and the subsequent increasing of the interlayer distance. Also shown are functional groups terminating on the surface of MXene layers. Taken from [13].

Gogotsi et al (2014) showed that an alternative synthesis method is possible using LiF and HCl instead directly using HF. The LiF salt would react with the HCl in solution to form HF in situ and etch the MAX phase [14]. The advantage of using this technique is twofold. Firstly it removes the dangers of directly handling HF acid, a dangerous laboratory substance. Secondly, there is an intercalation of Li+ ions and water molecules between the MXene layers, thereby weakening the electrostatic attraction between the layers and hence increasing the interlayer spacing [15]. This increased spacing facilitates better ion transport in the material, allowing for improved electrochemical performance.

X-ray diffraction (XRD) and Raman spectroscopic analysis is often used to confirm the success of the etching process. In the XRD pattern of $Ti_2CT_X$ Mxene we see the disappearance of most peaks, visible in Figure 2.3a), in particular the peak which sits between 40°C and 50°C depending on the X-ray source of the instrument. In addition there is the strengthening, broadening and downshift of the (002) peak [12], which corresponds to the interlayer spacing between the M-X layers. In the Raman spectra, visible in Figure 2.3b), the characteristic peaks $\omega_{1-4}$ of the MAX phase $Ti_2AlC$ are visible. These are assigned to the shear and longitudinal vibrations of the Ti and Al atoms [16]. After etching these peaks are upshifted and broadened. This behaviour is also observed in doped graphene, and indicates that particles from the etching solution have been introduced [17] corresponding with the replacement of Al by functional groups. The appearance of the D and G bands - $\omega_5$ and $\omega_6$ respectively - are also visible, and are due to $sp^2$ sites. The G-band peak is associated with the stretching of the C-C bond in carbon materials and occurs in all $sp^2$ carbon systems with both rings and chains. The D-band peak is dependant on the $sp^2$ fraction and appears only if the $sp^2$ is in disordered rings, as is the case of $Ti_2CT_X$ Mxene.

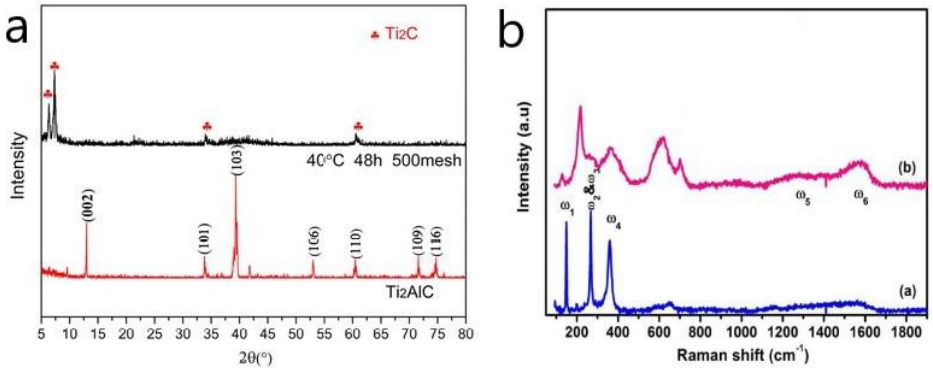


Figure 2.3: An example of a) an XRD pattern [18] and b) a Raman spectrum [19] of $Ti_2CT_X$

### 2.1.3 Basic MXene Structure

Often instead of leaving the M-X layers bare the etching process replaces the A group elements with functional groups, usually hydroxyl (OH), fluorine (F), or oxygen (O) molecules if HF is used as an etchant. These functional groups tune the band gap, and therefore the electrical properties of the MXene. Theoretical studies of bare MXene layers indicate that they would be metallic in nature, however, due to the functional groups bonding to the M-X layers these MXenes are often semiconducting[12]. The etching process is also observed to increase the interlayer spacing between the M-X layers. This is possibly due to the substitution of an A group atom with two functional groups, as two bonds will be open after the A group atom has been removed, one on each M-X layer [12]. A likely reason for the observed increased interlayer distance post-etching could be because of a Coulomb repulsion between the two functional groups, or even the absence of a stronger M-A bond which had previously acted to attract the layers.

It should be noted that it is difficult to predict which surface groups will form on the M-X surfaces. Most density function theory models to date focus on specific functional groups and do not discuss mixed functional groups forming on the M-X surfaces[15]. In reality, most synthesis processes result in many different functional groups forming, as is indicated in Figure 2.2.

### 2.1.4 MXene Morphologies

The morphology of MXenes are highly dependent on the synthesis method employed. For MXenes made using HF acid as an etchant an accordion-like morphology is typical. For MXene made using the LiF and HCl method the MXene is more densely packed and is a clay like material. These features are shown in Figure 2.4.

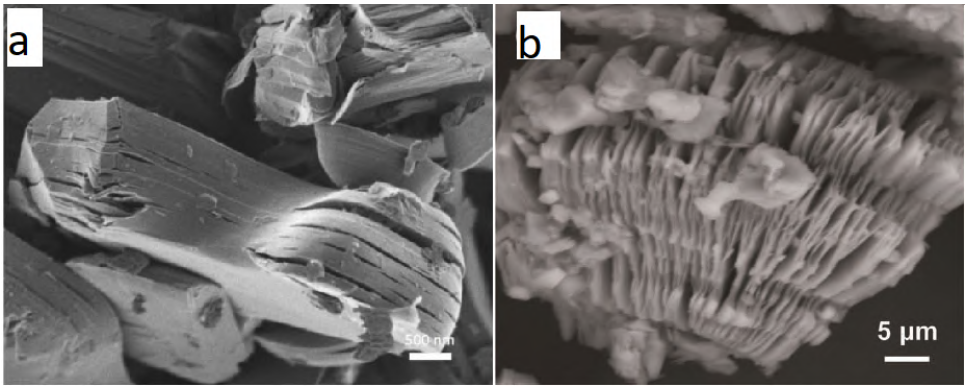


Figure 2.4: A comparison between $Ti_3CT_X$ made a) using LiF and HCl [14] and b) direct concentrated HF [11].

Delamination of the MXene multi-layered structure is usually performed by intercalating the layers with some molecule and then applying some mechanical shearing force to separate the layers. However, because

the MXene clay already has $Li^+$ ions intercalated only very slight mechanical shearing is required, and without the need of additional molecules [15]. The delamination process separates the layers in the multi-layered MXene, forming MXene nano-sheets (MNS). These MNS facilitate much better ion transport and thereby allow for higher capacitances to be realised.

MXene nanoribbons (MNRs) are another possible morphology for MXene to form. By exposing the MNS to a continuous shaking treatment in a KOH solution researchers were able to form these MNRs from $Ti_3C_2$ MXene. The benefit of forming MNRs is that the interlayer spacing is larger compared to that of the MNS, and allowed for better ion reaction kinetics [20], thereby enhancing the energy and power densities of the material. Figure 2.5a depicts this process visually, and Figure 2.5b-d shows the scanning electron microscopy (SEM) images of the respective morphologies.

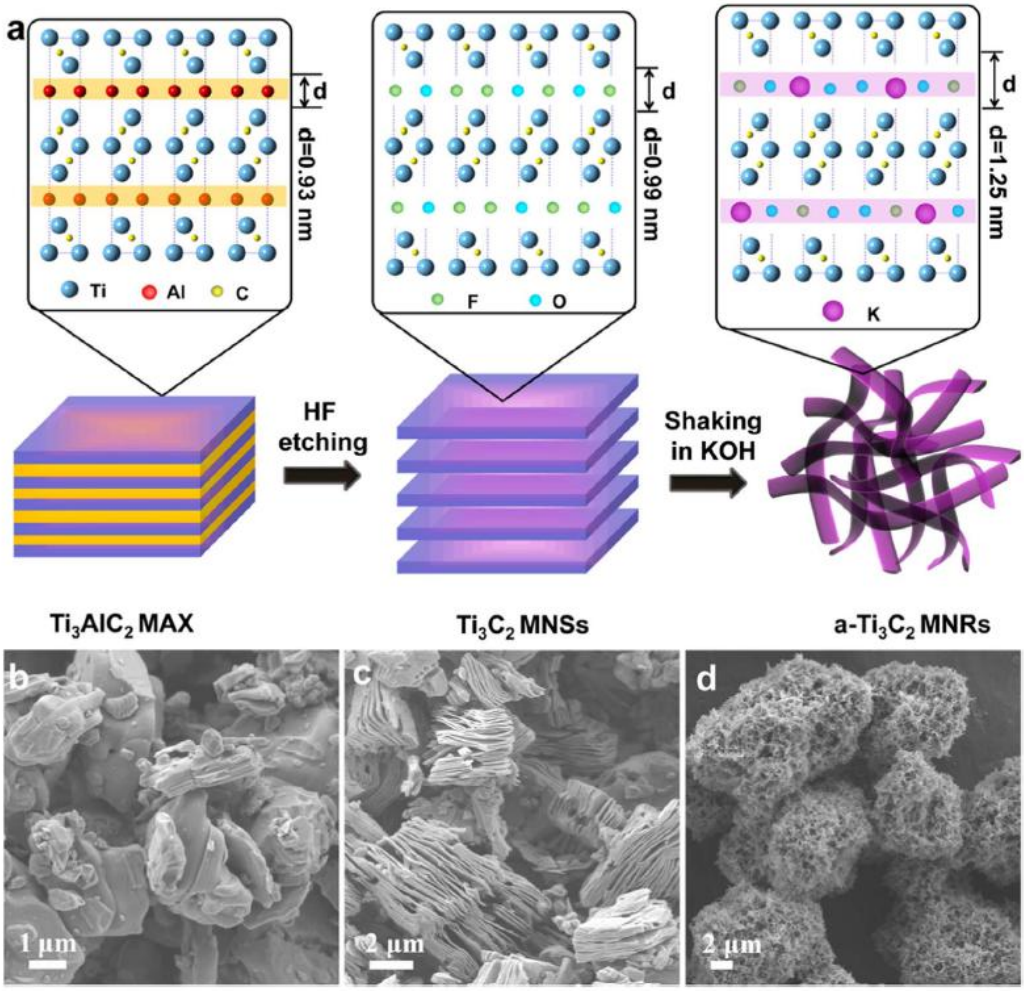


Figure 2.5: a) an illustration of the formation process of nanoribbons, starting from the MAX phase structure, etching in HF, and shaking in KOH. SEM images of b) the MAX phase $Ti_3AlC_2$, c) $Ti_3C_2$ MNSs, and d) alkalised $Ti_3C_2$ MNRs

### 2.1.5 MXene in Supercapacitors

At this stage most research in MXene applications in supercapacitors is focused on the MXene $Ti_3C_2$ and not the MXene $Ti_2C$ so they are relatively few papers on this MXene. However, there are two that of specific interest to this work.

While MXenes do not exhibit as high surface areas as other EDLC materials, they do allow for pseudo-capacitive ion intercalation which gives rise to high capacitances [21]. Lukatskaya et al (2015) suggested that this is a result of the pseudocapacitive redox reactions of the Titanium in the MXene [22]. Ling et al (2014) showed that increeasing the interlayer spacing can facilitate better ion transport and hence improve the capacitance of the material [23].

In this study the MXene $Ti_2CT_X$ has been intercalated with onion-like carbons (OLCs) in order to improve its electrochemical behaviour. OLCs have been shown to exhibit excellent conductivities and rate handling capabilities [10], and by integrating them into the MXene compound we will be increasing the interlayer spacing and improving the stability of the layers.

To date most published research has been focused on the heavier MXene $Ti_3C_2$ and not its lighter cousin $Ti_2C$. Relevant works on the lighter MXene include Rakhi et al (2016) who showed that the heavier $Ti_3C_2$ yielded a specific capacitance (in a symmetric set up) of around 80 F/g, which was more than twice that of the specific capacitance of $Ti_2C$, which as around 32 F/g [24]. These results were obtained under the same experimental conditions, at 30% wt KOH and at 1A/g current density. Melchior et al (2018) showed that by adding carbon nanospheres (CNS) the performance of the lighter Mxene in a symmetric set up could yield around 50 F/g in 1M $LiSO_4$ [19], which is a 65% increase in specific capacitance compared to the previous result.

In this study the fabrication and performance of a symmetric supercapacitor made from the MXene $Ti_2C$ which has undergone OLC doping will be assessed in a 1M $H_2SO_4$ electrolyte. The use of 1M $H_2SO_4$ has been explored by Gogotsi et al in a few of their studies [15], [14] and has been shown to have one of the highest current responses when compared to other aqueous electrolytes.

It should be noted that for a symmetric supercapacitor the specific capacitance per electrode is typically 4 times greater than the specific capacitance of both electrodes [25]. This will be highlighted again when the results in this work are compared to the literature.

## 2.2 Onion-Like Carbons

Carbon nanomaterials are a diverse family and have applications in many areas, including electronics, sensors, and energy storage. This family includes nanoparticles such as fullerenes, carbon nanotubes, and of course graphene. OLCs, also called carbon onions, were until recently quite understudied, being overshadowed by these other carbon nanomaterials [10]. OLCs consist of concentric spherical closed shells of carbon, a distinctly onion-like structure, hence the name. They are most commonly made by annealing nanodiamond (ND), another understudied carbon nanomaterial.

### 2.2.1 OLC synthesis

OLCs can be synthesized via a number of techniques, however, we will focus on the most commonly used method: the vacuum annealing of ND precursors. The ND can also be annealed in the presence of an inert gas like argon.

The annealing temperature greatly influences the final structure of the OLC. During annealing, the ND begins to undergo a phase change into graphitic carbon. The process begins from the outside in. As the temperature is increased, the ND core becomes progressively smaller, and at the highest annealing temperatures this core disappears altogether, yielding a fully formed OLC. The final structure of the OLC is also dependent on the ND precursor. The ND particles can vary in size, with most OLCs being synthesized from ones which are around 5nm in diameter. While these NDs are mostly carbon (80-90%), they also typically contain some oxygen and hydrogen as functional groups, and nitrogen in the ND core. Usually the annealing process results in a thin layer of disordered and amorphous carbon engulfing the OLCs[10].

This method is limited only by the size of the furnace used, and so is scalable and therefore viable in an industrial setting. It is also fairly cheap (2 euros per gram as of 2016), contains a low impurity count, and is also a fairly simple procedure. A drawback to this method is that the OLCs produced will not all be perfectly spherical carbon onions, but nevertheless it has an almost 100% yield and is very cost efficient [10].

### 2.2.2 OLC Structure

As mentioned above, the structure of the OLC is highly dependent on its synthesis, and in the case of the annealing of NDs it is especially dependant on the annealing temperature. Figure 2.6 below illustrates this dependence. At around 200°C desorption of water occurs as well as the removal of oxygen containing functional groups. As the temperature increased more functional groups - like carboxyl or anhydride

groups - detach from the ND. The ND consist of $sp^3$ hybridised carbon, and as these functional groups detach it creates dangling bonds as there is one bond that is now freed. As the temperature reaches around $800 - 900°C$, there is a phase transformation as the ND graphitizes, forming $sp^2$ hybridised carbon, as $\pi$ bonds between the $p$ orbitals form. This forms shells of graphitic carbon on the outside of the ND. As the temperature increases, this graphitization moves progressively on towards the ND core. It is common for defects to occur at the surface of the emerging OLC as the functional groups are removed. As the temperature reaches between $1100 - 1300°C$, the carbon becomes increasingly more graphitic towards the core and the number of defects decrease. At around $1800 - 2000°C$ the highly disordered $sp^3$ hybridised ND is fully transformed into a highly ordered $sp^2$ hybridised OLC[10].

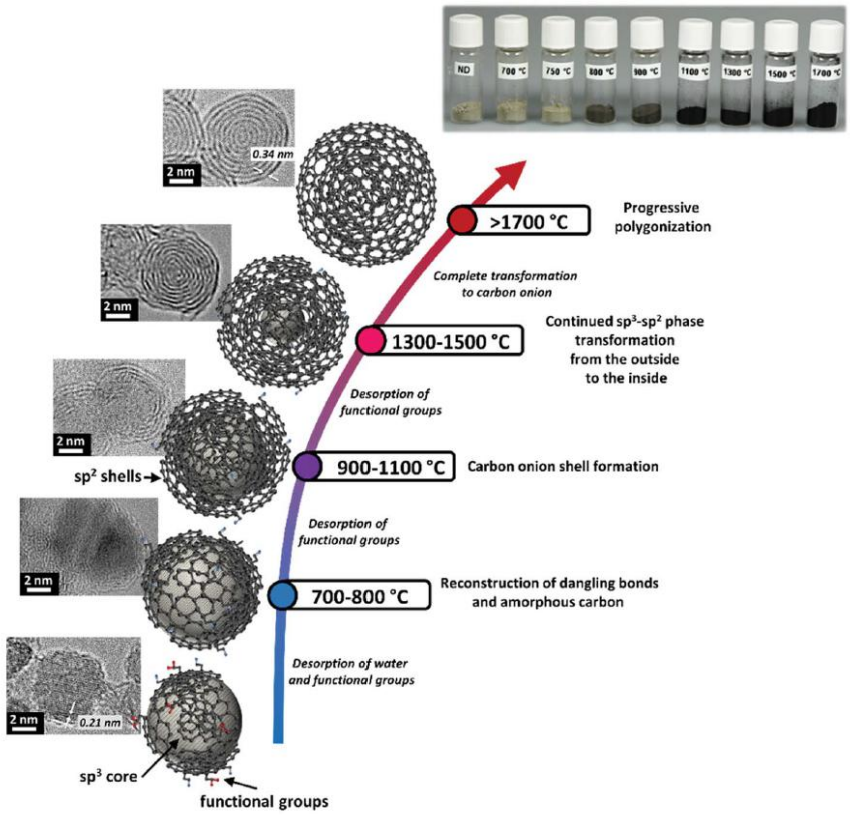


Figure 2.6: An illustration of the evolution of the ND as the synthesis temperature increases, showing how the ND progressively graphitises with increasing temperatures. Taken from [10].

### 2.2.3 Electrochemical Properties of OLCs

The two most important properties of OLCs affecting their electrochemical performance is their conductivity and their surface area. The surface area of the material influences how many ions from the electrolyte can intercalate in the material, and therefore affect how much charge can be stored in the material, and the pore distribution that makes up the surface area influences the ion transport, i.e. how easily ions can move in and out of the material. This translates to facilitating the power handling of the material, i.e. the charge and discharge times of the material as well as capacitive retention. If a material has easily accessible sites it will be able to handle higher rates of charging/discharging for longer periods of time compared to a material which has a more restrictive pore distribution.

The conductivity of the material affects how much energy is lost during the charge transport, with a higher conductivity resulting in better power handling as well capacitive retention compared to a lower conductivity.

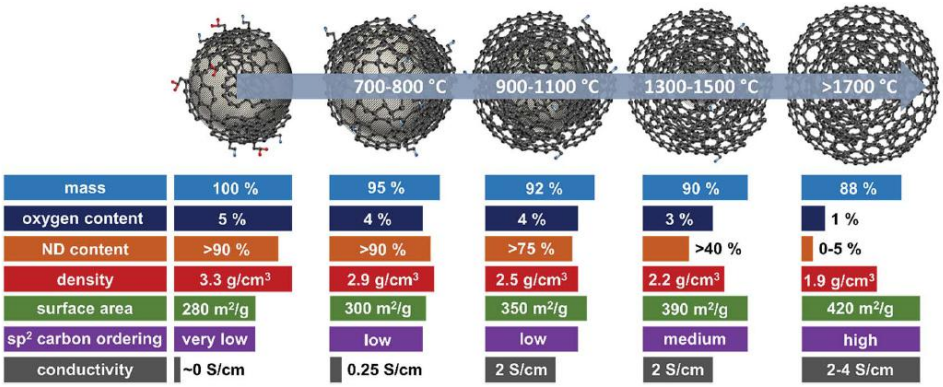


Figure 2.7: A summary of temperature dependant OLC properties like conductivity and surface area. Taken from [10].

Figure 2.7 shows how these properties, as well as several others, are affected by the annealing temperature. The conversion from $sp^3$ ordering to $sp^2$ ordering is what is responsible for the change in these properties. The actual figures will differ depending on the actual synthesis technique, but the overall trend will be the same.

It should be noted that at above 1500°C particle sintering - particles fusing together during heating - will occur in an inert atmosphere, resulting in the surface area remaining the same or even decreasing as particles agglomerate[26]. As the nanodiamond ($sp^3$) transforms to graphitic carbon ($sp^2$) its density decreases, resulting in an increase in surface area. The general specific surface area (SSA) of OLCs lies in the range of $300 - 600 m^2/g$. This is modest compared to some other carbon nanomaterials, for example activated carbon has an SSA of over $1500 m^2/g$. However, most of the surface area of OLCs are localised to the external surface of the structure, removing the need for ions to intercalate into the nanoparticle which often causes losses in energy or even sometimes results in inaccessible sites. The surface area of an OLC is fully accessible, allowing for far greater ion transport properties.

The increase in conductivity from $sp^3$ to $sp^2$ is explained by looking at the nature of the bonds. In $sp^3$ ordering the $s$ orbital hybridises with the three $p$ orbitals, forming four new $sp$ orbitals. The electrons in these orbitals are bound to the carbon atom with a covalent $\sigma$ bond, making it tightly bound to the nucleus and therefore it is more difficult for the electron to move in the material [27]. This type of bonding leads to insulative behaviour in a material, like in the ND particles.

In $sp^2$ ordering only two of the $p$ orbitals hybridise with the $s$ orbital, forming three $sp$ orbitals and therefore three covalent $\sigma$ bonds, but the last electron forms a delocalised $\pi$ bond. This electron is essentailly free to move around between carbon atoms and gives rise to the high conductivity associated with materials like OLCs, graphene, and carbon nanotubes which have this type of carbon ordering present [26].

### 2.2.4 OLCs in Supercapacitors

The modest surface area of OLCs makes them poor active materials for electrodes as it results in low specific capacitances, especially when compared to other carbon nanomaterials such as activated carbon or carbon nanotubes. Most research focuses on using OLCs as a conductive additive as opposed to an active material for this reason, with the exception of using OLC as the active materials in a micro-supercapacitor [28].

In a PhD thesis by John McDonough (2014) [7] the use of OLCs as an alternative conductive additive to carbon black was investigated. It was found that when using activated carbon as an active material, the use of OLCs increased the capacitance to 86 F/g from 71 F/g with carbon black, and from 60 F/g with no conductive additive. The use of OLCs as an active material was also investigated, yielding a poor 25 F/g for the aforementioned reasons. These measurements were carried out in a three electrode configuration.

OLCs have also been used to increase the capacitance of the MXene $Ti_3C_2T_X$, increasing the capacitance from 360 F/cm$^{-3}$ to 397 F/cm$^{-3}$ using freestanding films [29] in a three electrode configuration.

# Chapter 3

# Methodology

The MXene $Ti_2CT_X$ was synthesized from $Ti_2AlC$ MAX phase and doped with carbon onions. The MXene was then doped with OLCs and the resulting material was used to fabricate electrodes for electrochemical testing. A range of physical as well as electrochemical characterisation techniques were used to verify the materials synthesized as well as gain an understanding of the underlying structure so as to better explain the observed electrochemical behaviour.

## 3.1 From MAX Phase to MXene

The HCl/LiF approach shown by Gogotsi et al (2014) to be successful for the synthesis of $Ti_3C_2T_X$, and by Liu et al (2016) for the synthesis of $Ti_2CT_X$, was followed.

2 g of LiF powder was added to 40 ml of 6M HCl and sonicated for 15 minutes. 2 g of the MAX phase $Ti_2AlC$ (Maxthal 211, Kanthal AB, Sandvik Materials Technology, Sweden, $> 90\%$ wt purity, $< 45\mu m$ particle size) was then slowly added to the LiF/HCl solution. This was then magnetically stirred at between 40 and 45 °C for 48 hours, with an additional hour required to reach a steady temperature. The solution was then centrifuged and washed with ethanol water several times until the pH reached approximately 6. This was done to get rid of any organic molecules as well as separate the sample from the rest of the etchant. The centrifugation would have also somewhat delaminated the MXene sheets. The resulting powder was then vacuum dried at 80°C for 24 hours. The XRD patterns showed some anomalous peaks which were most likely due to some residual aluminium and some organic compounds that were still present due to insufficient washing. Hence, it was decided to etch the resulting powder for another 48 hours following the same procedure. The resulting XRD pattern was representtaive of what was expected when compared to the literature. We had a final yield of 936 mg of $Ti_2CT_X$.

The set up for the synthesis is shown in Figure 3.1. The solution was magnetically stirred in a round bottom flask with one opening used for measuring the temperature and the other used for applying a condenser to keep the temperature constant. Figure 3.2 shows the centrifuge and the vacuum oven used during the synthesis process.

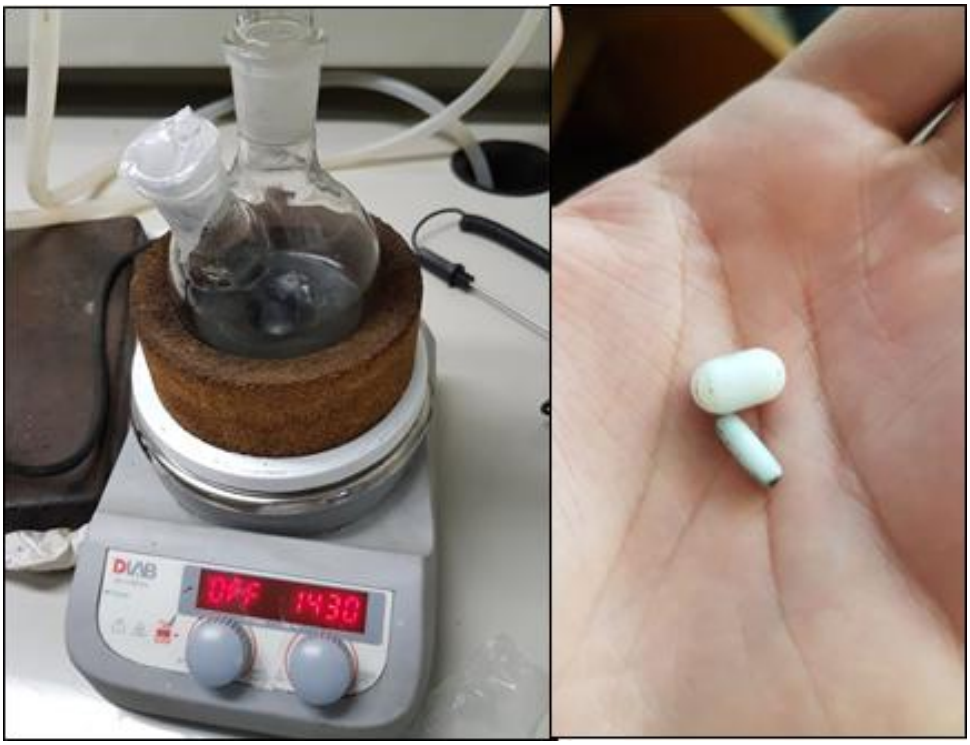


Figure 3.1: Set up for etching of MXene showing MAX phase in solution with LiF and HCl on a magnetic stirrer (left), and stir bar used for the magnetic stirring (right).


Figure 3.2: Centrifuge used for washing the MXene post-etching (left), and the vacuum oven used for drying the MXene after washing (right).

## 3.2 Synthesizing OLC-doped MXene sheets

The synthesis of the OLCs were not carried out as part of this work, however, the process is detailed as follows. They were synthesized by heating nanodiamond (ND) powder (98-99% purity, NaBond Technologies®) in a muffle furnace at 1300°C for 3 hours under an Argon atmosphere.

Two methods of preparing the OLC doped MXene were explored. The first was made by adding OLCs to the $Ti_2CT_X$ powder in a 90:10 (MX:OLC) ratio and sonicating for 12 hours in dimethyl fluoride (DMF) solvent. The solution was then centrifuged for several hours and washed with ultrapure water. The

resulting solution was decanted and vacuum dried at 80°C for 24 hours. When mixed into the electrode paste this sample would yield 8% doping as the ratio between the sample and other additives would be 80:20. The sonication process would also contribute to delaminating the sheets further. Figure 3.3 shows the OLC doped MXene after sonication in DMF.

Figure 3.3: OLC doped MXene after sonication in DMF (left), and after drying in a vacuum oven (right).

The second method was involved adding the OLCs to the MXene in a 95:5 ratio (MX:OLC) sonicating the mixture in NMP solvent for 4 hours. The solution was vacuum dried directly for 12 hours without any washing. This procedure was seen to be more efficient and resulted in less sample loss, and so this was chosen to be the preferred method of creating the MX/OLC batches. The process was repeated by adding the OLCs to the MXene in a 90:10 ratio, so that two batches of MX/OLC were made; 5% and 10% doped MX/OLC.

A 90:10 ratio sample will yield 8% doping because the active material is only 80% of the electrode paste, and similarly the 95:5 ratio will yield 4% doping quanitity, as will be seen in Section 3.7.

## 3.3 MXene sheets to MXene nanoribbons

In an attempt to increase the surface area of the MXene two batches of pristine MXene were separated, 200mg each. This was added to 30ml of $KOH$ in the first batch, and 30ml of $NH_4OH$ in the second batch. The two batches were shaken continuously for 90 hours at 156 RPM. Figure 3.4 shows the two samples in solution. The resulting solutions were then centrifuged and washed with ethanol water until the supernatant reached a pH of approximately 7. The samples were then vacuum dried for 48 hours at 60°C

## 3.4 OLC doping of MXene Nanoribbons

There were two batches of MXene nanoribbons; MXene shaken in KOH, and MXene shaken in $NH_4OH$. Each of these batches were then doped with OLCs. This was done by adding OLCs to the sample in a 90:10 ratio, and adding a few drops of DMF. This was then sonicated for 48 hours. The resulting mixture was then centrifuged for several hours and washed with ultrapure water. The precipitate was dried for 48 hours at 60°C. When mixed into the electrode paste these samples would constitute 8% OLC doping.

Figure 3.4: MXene in KOH and $NH_4OH$ solution after shaking treatment for 90 hours.

## 3.5 Summary of Materials synthesized

The list below includes all the samples synthesized during this research.

- Pristine MXene
- 5% doped MXene/OLC (NMP solvent)
- 10% doped MXene/OLC (NMP solvent)
- 10% doped MXene/OLC (DMF solvent)
- $KOH$ MNR
- $NH_4OH$ MNR
- $KOH$ MNR/OLC (10%)
- $NH_4OH$ MNR/OLC (10%)

It should be noted that due to the extremely poor electrochemical performance of the KOH and $NH_4OH$ MNRs during the 3 electrode testing their OLC doped counterparts were not tested.

## 3.6 Physical Characterisation

Many physical characterisation techniques were performed only after the electrochemical characterisation of the samples was complete, so that no resources were wasted on characterising bad samples. The two techniques used during material synthesis were XRD and Raman, as they could effectively guide the synthesis process to allow us to be sure we were creating the correct materials.

Physical characterisation techniques used in this investigation included the following:

- X-ray Diffraction (XRD)
- Raman Spectroscopy (Raman)

- Scanning Electron Microscopy (SEM)
- Transmission Electron Microscopy (TEM)
- Brunauer–Emmett–Teller (BET) surface area analysis
- X-ray Photoelectron Spectroscopy (XPS)

### 3.6.1 X-ray Diffraction

XRD involves bombarding a sample with X-rays and measuring the reflected photons as a function of the diffraction angle. When the X-rays encounter a layer they will interact constructively, thereby creating a peak in the XRD pattern. If there is no layer present the photons will interact destructively. In other words, destructive and constructive interference occurs as a function of the path difference between rays scattered from different layers, allowing the instrument to measure the reflected photons as a function of the diffraction angle. The relationship between the wavelength of the X-ray, the diffraction angle, and the interlayer distance is determined by Bragg's Law, and is shown schematically in Figure 3.5:

$$n\lambda = 2dsin(\theta) \tag{3.1}$$

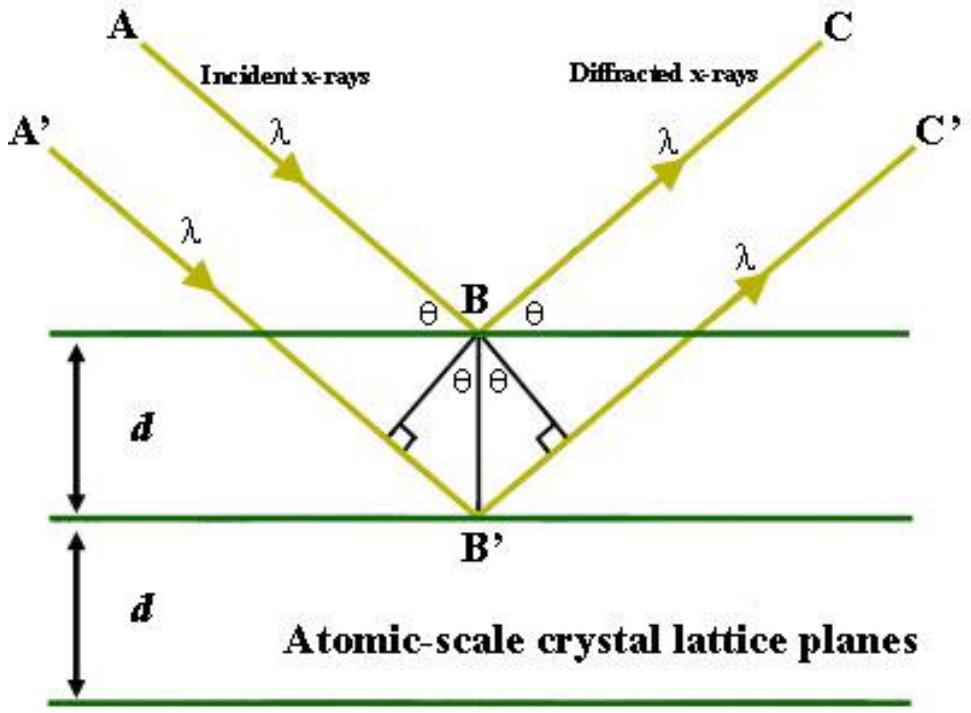


Figure 3.5: Schematic representation of the principle of Bragg's Law showing the reflection of X-rays from different layers. Taken from [30].

During the etching of the A group element from the MAX phase a layer of molecules will essentially be removed. This will effectively cause the reduction of specific peaks in an XRD pattern. The interlayer distance is also likely to relax as the A group layer would effectively act as a glue for the MX layers, which would cause peaks to shift to lower $2\theta$ values.

A good example of this is shown in a paper by Liu et al (2016) [18] where $Ti_2C$ was prepared from its corresponding MAX phase, $Ti_2AlC$. Figure 3.6 below shows the XRD pattern used in the paper. One can see that many of the peaks have disappeared, in particular the peak around 40°. This is the peak attributed to the $Ti_2AlC$ phase. Also notice the shifting of the (002) peak to lower angles; this is due to the relaxation of the interlayer distance, and is attributed to the $Ti_2C$ phase. The rest of the peaks are caused by other phases in the sample, such as $TiC$.

XRD is especially useful after etching the MAX phase, as one can get a good idea as to whether the etching was successful or not from a relatively short scan (around 10 - 30 min) using an instrument like the D2 Bruker X-ray diffractometer, also shown in Figure 3.6, which is what was used for this research.

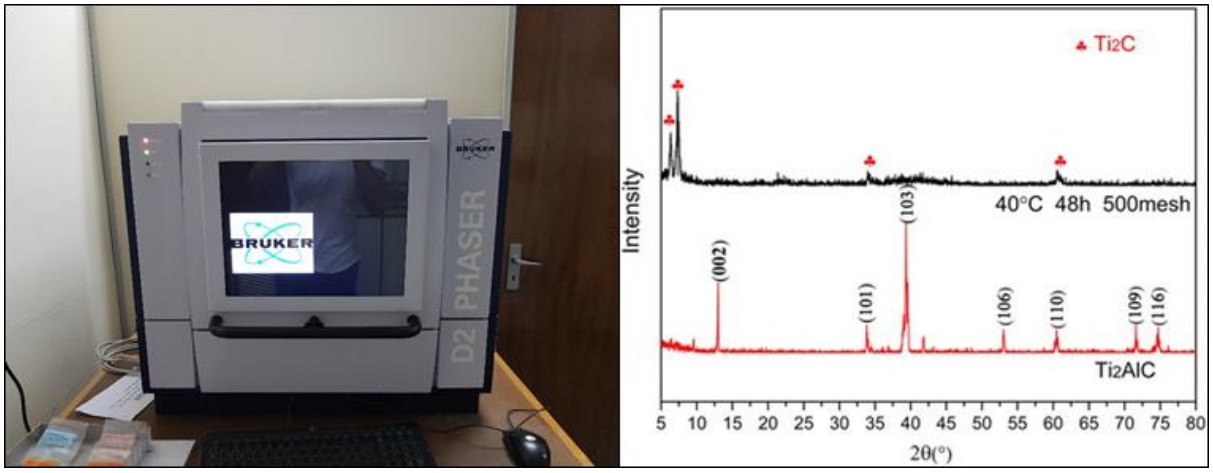


Figure 3.6: Bruker D2 X-ray Diffractometer used in this research (left), and an example of an XRD pattern for the MXene $Ti_2CT_X$ from Liu et al (2016) [18].

### 3.6.2 Raman Spectroscopy

Raman spectroscopy uses the inelastic scattering of light to measure wavelength shifts in reflected photons to determine which vibrational modes are present in a sample. It is a useful technique in determining whether the exfoliation of the MAX phase was successful as one can see if the vibrational modes of Al are present or not in the exfoliated sample. Figure 3.7 below shows an extract from Melchior et al (2018)[19] where she compares the Raman spectrum of the MXene $Ti_2CT_X$ with that of its MAX phase precursor $Ti_2AlC$. The first three peaks are characteristic of the MAX phase according to Spanier et al (2005)[31], and the broadening of the peaks indicate the disordering that is expected during the exfoliation. The shifts in wavelength also indicate a change in vibrational modes, specifically the shift of the first peak indicates the removal of Al from the material. In addition, the appearance and/or strengthening of D and G bands in the spectrum correlate to the rise of disordered carbon in the material which is to be expected from the etching process.

Figure 3.7 also shows the Raman instrument used in this work.

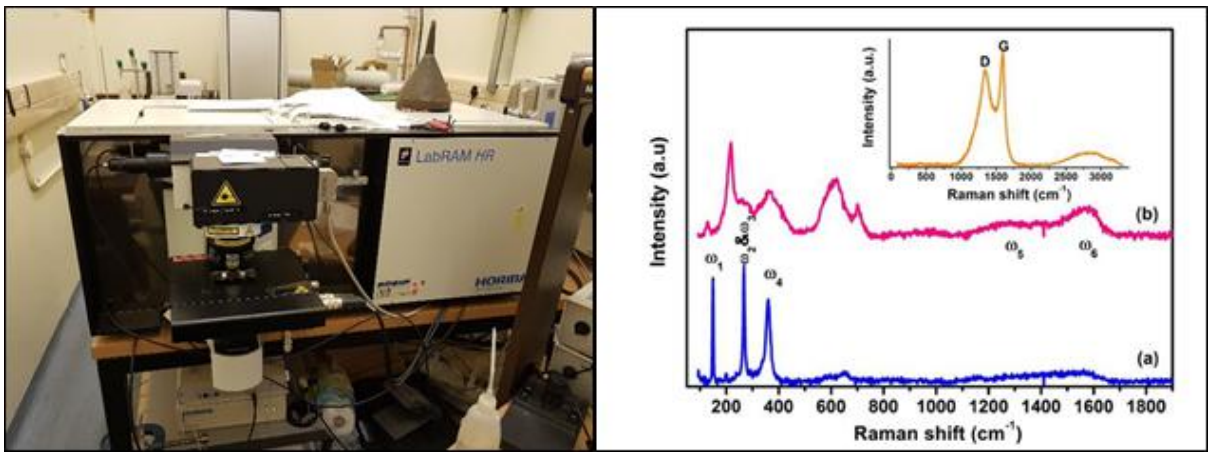


Figure 3.7: Raman instrument used in this work (left), and an example of a Raman spectrum for the MXene $Ti_2CT_X$ from Melchior et al (2018) [19].

### 3.6.3 Scanning Electron Microscopy

The principle of electron microscopy is essentially bombarding a sample with electrons and detecting the scattered electrons with a variety of detectors. The measurement takes place inside a vacuum chamber in an electron microscope unit. All detectors are inside the chamber with the sample, with an electron gun mounted above the sample. It should be noted that electron microscopes can be outfitted with many different detectors.

The accelerated electrons contain significant amounts of kinetic energy and this is dissipated into various signals when the electrons interact with the sample and decelerate. The signals which are important for SEM imaging are the secondary electrons. Other signals include backscattered electrons, diffracted backscattered electrons, characteristic x-rays, visible light and heat. These other signals can give information about the contrast between different phases of the material as well as chemical composition of the sample, amongst other things [32].

SEM imaging is an excellent tool for analysing the surface features of a material. It allows the researcher to truly visualise the sample they are working with. For example, for MXenes we can see the layered sheets in the structure (Figure 3.8 below).

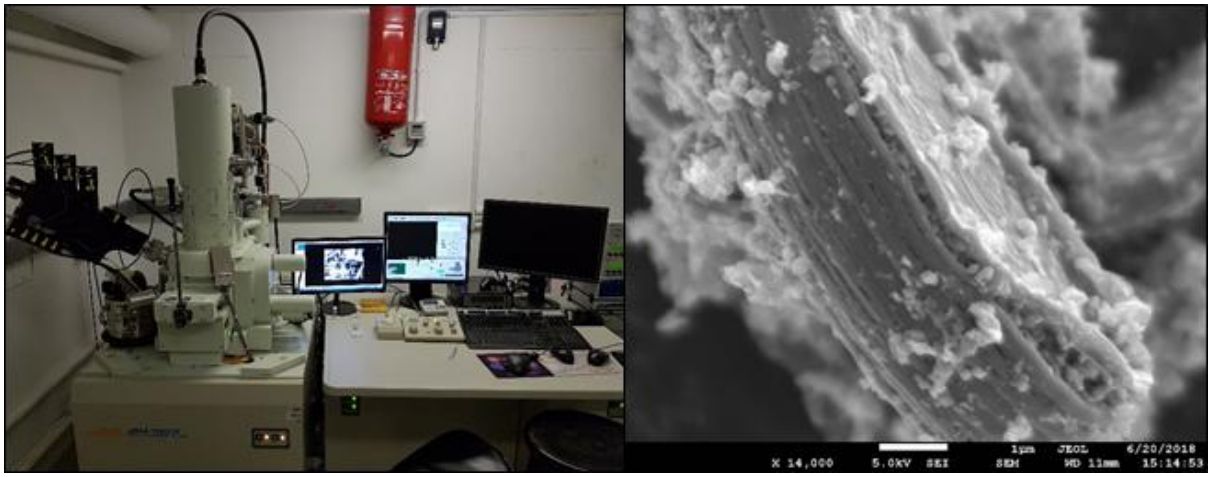


Figure 3.8: Electron microscope used for SEM in this work (left), and an example of a SEM image of the MXene $Ti_2CT_X$ from this work (right).

It should be noted that TEM works in a similar way to SEM, except the electrons are accelerated to much higher energies ($\sim$ 120 keV).

### 3.6.4 Brunauer–Emmett–Teller surface area analysis

The surface area of the materials used in this work can be analysed via BET surface analysis. The principle of BET rests on Brunauer–Emmett–Teller theory, which assumes that gas molecules can adsorb onto a surface in an indefinite amount of layers, they only interact with adjacent layers, and the Langmuir theory can be applied to each layer. This yields the BET equation:

$$\frac{1}{v\left[(p_0/p)-1\right]} = \frac{c-1}{v_m c}\left(\frac{p}{p_0}\right) + \frac{1}{v_m c}$$

Where $p$ and $p_0$ are the equilibrium and saturation pressure of adsorbates at the temperature of adsorption, $v$ is the adsorbed gas quantity, $v_m$ is the monolayer adsorbed gas quantity and $c$ is the BET constant:

$$c = exp\left(\frac{E_1 - E_L}{RT}\right)$$

The BET equation can be plotted as a straight line by putting the LHS on the x-axis and $p/p_0$ on the y-axis. The slope $A$ and the y-intercept $I$ can be used to calculate $v_m$ and $c$ via:

$$v_m = \frac{1}{A+I}$$

$$c = 1 + \frac{A}{I}$$

From which we can calculate the total and specific surface area:

$$S_{Total} = \frac{v_m N s}{V}$$

$$S_{BET} = \frac{S_{Total}}{\alpha} \tag{3.2}$$

where $v_m$ is in units of volume which are also the units of the monolayer volume of the adsorbate gas, $N$ is Avogadro's number, $s$ is the adsorption cross section of the adsorbing species, $V$ is the molar volume of the adsorbate gas, and $\alpha$ is the mass of the solid sample or adsorbent[33].

Figure 4.4 shows the BET instrument used in this work.

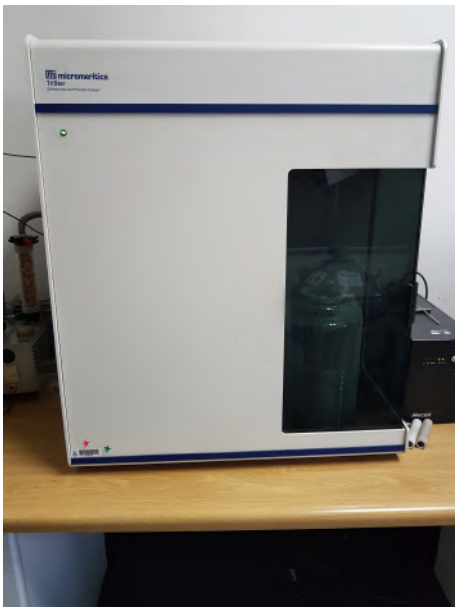


Figure 3.9: BET instrument used for this work.

### 3.6.5 X-ray Photoelectron Spectroscopy

XPS is a surface sensitive spectroscopic technique that involves irradiating the surface of a sample, in a high vacuum ($\sim$ 10 - 8 millibar) with an incident beam of x-rays while measuring the kinetic energy of electrons that escape the first 10nm of the surface of the sample and fall incident onto the detector. This technique is useful for determining the elemental composition in the parts per thousand range, empirical formula, electronic and chemical states of the elements in the sample material. Figure 3.10 illustrates an example of an XPS spectra of MXene from Melchior et al's paper (2018) [19].

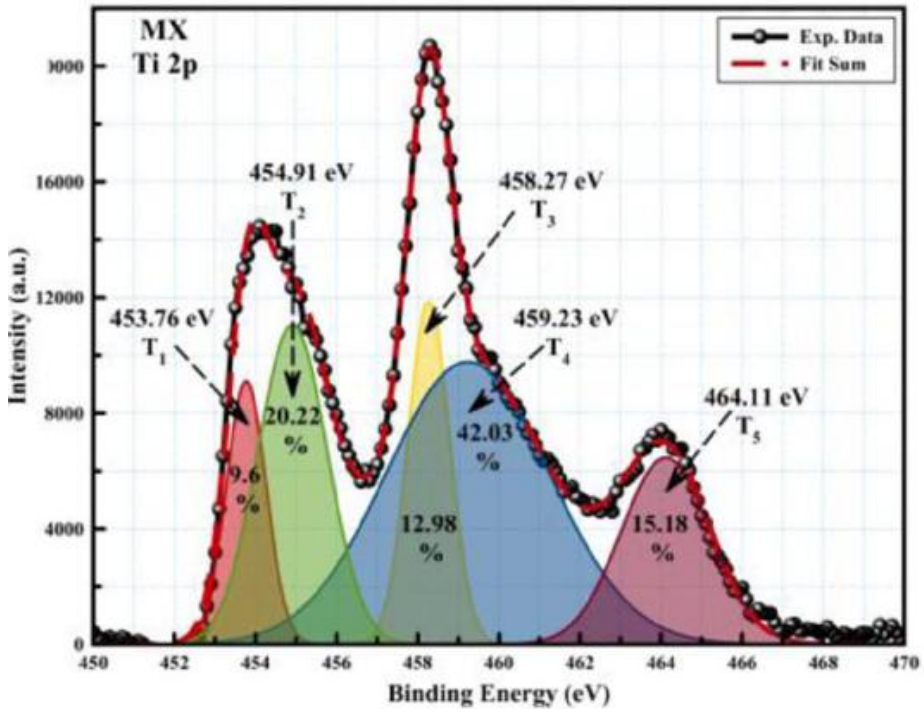


Figure 3.10: An example of an XPS spectrum for the MXene $Ti_2CT_X$ from Melchior et al (2018)[19]

## 3.7 Fabrication of electrochemical cells

### 3.7.1 Two Electrode Cells vs Three Electrode Cells

In electrochemistry a signal is applied to the material being investigated and a resulting signal is measured. Often this involves applying a current and measuring the corresponding voltage change (as in a Constant Current Charge/Discharge measurement) , or vice versa (as in a Cyclic Voltammetry measurement). There are other measurements which can be performed, but regardless of the measurement there are two types of cell configurations that can be used; a 3 electrode and a 2 electrode configuration. Each configuration has different uses, with the 3 electrode configuration being more generally used for measuring preliminary results and research, whereas the 2 electrode configuration is used for measuring results more important to industry. This is because the three electrode configuration measures the performance of the sample material on one working electrode, and thus the results are not representative of a working device, and the 2 electrode measures the performance of the sample material on both the anode and the cathode in the cell, which more closely mimics an actual working device.

In a three electrode cell the electrodes used are the working electrode, the counter (sometimes called the auxiliary) electrode, and the reference electrode. The schematic for this set up is shown in Figure 3.11. Current is passed between the counter/auxiliary electrode and the working electrode. The counter electrode's electrochemical properties are not of interest and should not produce any substances which may interfere with the working electrode. The potential of the working electrode is measured with respect to the potential of the reference electrode. The device used to measure the potential difference between the reference electrode and the working electrode has a high input impedance so that little to no current passes through the reference electrode, hence its potential will remain constant and equal to its open circuit value. A series of measurements over a potential range can give insight into the electrochemical behaviour of the sample, and this will be explained in more detail in Section 3.8. The working electrode usually consists of a current collector which is coated with the sample which needs to be analysed. In the case of this work carbon paper was chosen as the current collector as its high conductivity would not hinder the reactions in the cell.

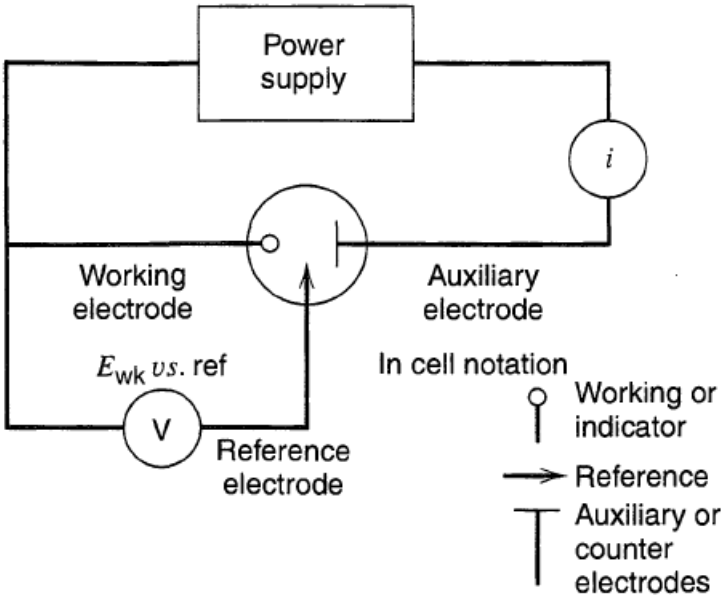


Figure 3.11: The schematic for a three electrode set up, depicting the working, counter, and reference electrodes.

In a two electrode cell the only electrodes present are the anode and the cathode. The current flows between them and the potential is measured across them. This type of configuration is preferred for research which is testing the industrial feasibility of a device, as the configuration mimics a real world cell. Figure 3.12 depicts this set up. It should be noted that the set up can either be symmetric or asymmetric. A symmetric cell implies that the same material is used on both electrodes, and an asymmetric cell implies that there is a different material on each electrode. A symmetric cell setup is used in this work. Again, both anode and cathode consist of the sample paste coated on carbon paper.

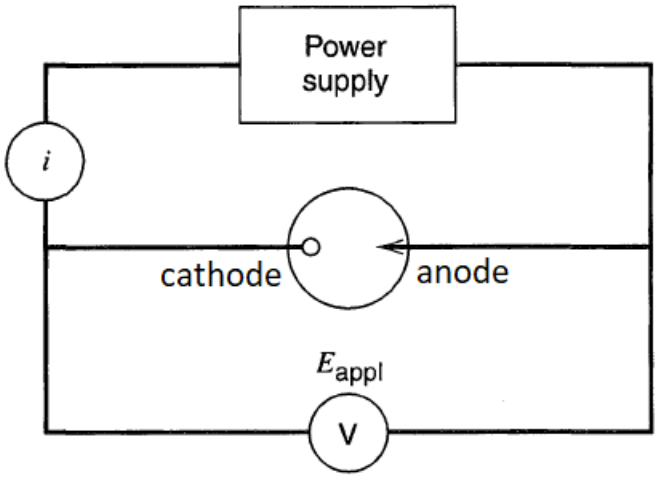


Figure 3.12: The schematic for a two electrode set up, depicting the anode and cathode.

In this work three electrode measurements were used to obtain preliminary data, and this was followed by two electrode measurements to assess the feasibility of the samples in a real-world setting.

### 3.7.2 Swagelok Cells vs Traditional Cells

In addition to configuration of a cell one must also decide what type of cell to use to test the sample. The traditional method used is to place the three electrodes in a beaker of electrolyte and take the measurements using leads connected to these electrodes. This type of set up is shown in Figure 3.13

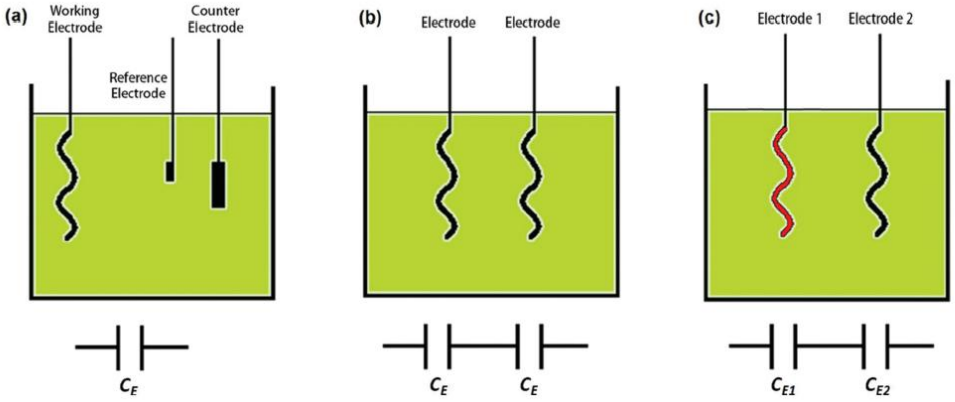


Figure 3.13: An illustration of a traditional beaker method for measuring electrochemical performance in a) three electrode, b) symmetric two electrode, and c) asymmetric two electrode configurations. Taken from [3].

More recently, for supercapacitor research, Swagelok cells have been used. These are cells which usually allow for the electrodes to placed right flush against each other with a separator containing the electrolyte in between. In this work two types off Swagelok cells were explored; the Split Flat cell (SFC) and the T-type cell. Figure 3.14 depicts a schematic and image of the SFC, and Figure 3.15 depicts images of the T-type cell.

The SFC Swagelok has a few advantages over the traditional beaker set up; they are reliably sealed which minimizes the interference of atmospheric effects like evaporation of electrolyte or oxygenation of the electrolyte which can affect performance, they allow for direct contact between electrodes and the cell separator, and allow for less electrolyte to be used to test the system. They also more closely mimic a real-world cell. The two electrode and three electrode SFC were two distinct cells.

The T-type Swagelok proved to be more reliable than the SFC as it offers all the advantages described above, and had less working parts so the results were more reliable and reproducable, and the cell was far easier to prepare. We will go into detail in the preparation for both cells further on. The T-type cell could also be used in both the three elctrode and two electrode configurations.

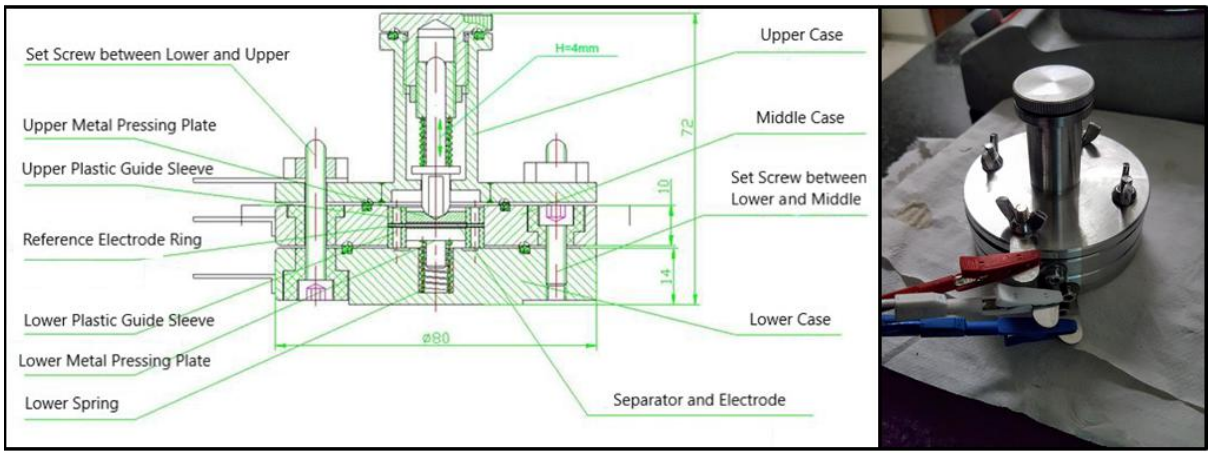


Figure 3.14: A schematic of the three electrode Swagelok Split Flat cell used in this work (left), and an image of it in operation (right).

Figure 3.15: An image of the T-type Swagelok cell used in this work.

### 3.7.3 Preparation of Electrode Paste

The paste for the working electrodes (in the three electrode set up) and the anode and cathode (in the two electrode set up) were prepared in the same way. The only difference between different samples was the choice of active material itself, and not its ratio to other additives. Carbon black was added as a conductive additive and polyvinylidene fluoride (PVDF) as a binder to the active material. The ratio between the active material, carbon black, and PVDF was 80:15:5. A few drops of N-Methyl-2-pyrrolidone (NMP) were added to the mixture and the sample was stirred magnetically for 24 hours. NMP was added as needed until a smooth texture was observed before leaving the sample to stir. The materials used and the stirring process is shown in Figure 3.16.

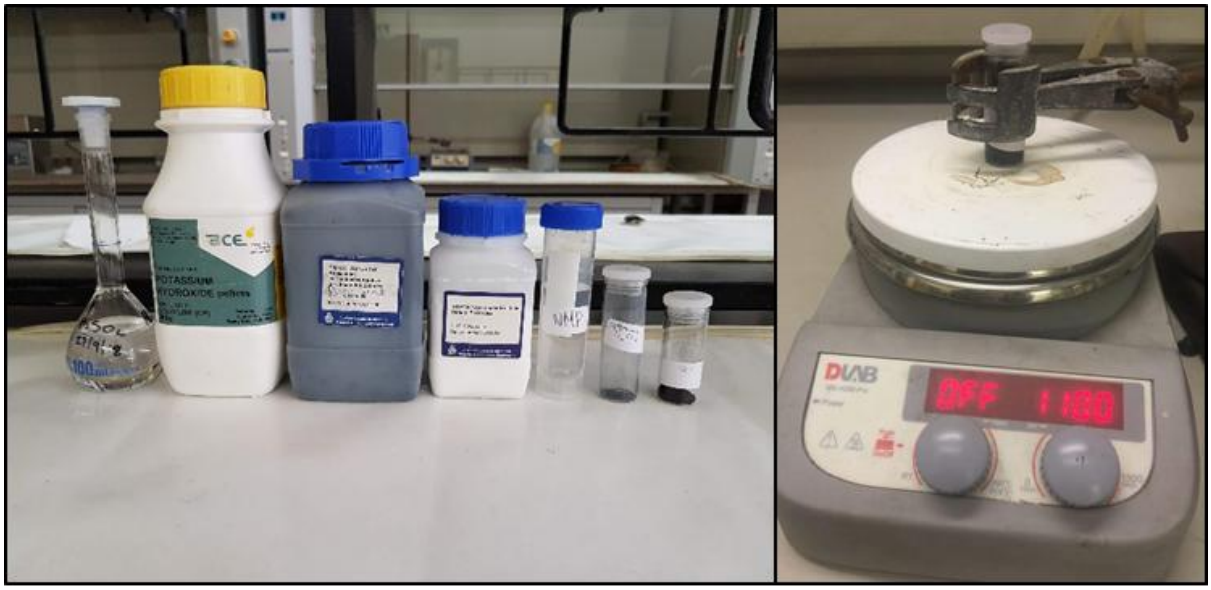


Figure 3.16: The materials used in this work (left) from left to right: 1M $H_2SO_4$ solution, $KOH$ pellets, Carbon Black, PVDF binder, NMP solvent, Synthesized MXene, OLC powder. An image of sample paste magentically stirring (right).

### 3.7.4 Coating of Electrodes

When coating the electrodes care was taken to weigh the electrode before and after coating so as to properly determine the mass loading. The bare 12 mm carbon paper electrode was cut from a sheet of carbon paper using a 12 mm punch. The carbon paper electrode was placed on a piece of filter paper. A micropipette was used to draw up 18 $\mu$m of sample for consistency and this was applied to the bare working electrode. A spatula was used to spread the sample until an even as possible a surface was formed. The electrode was weighed during the coating process so that the mass loading was as consistent as possible. The working electrode after coating tended to be between 19 mg and 20 mg. The electrode was then vacuum dried for 12 hours at 80°C. An image of the coating process and some coated electrodes is shown in Figure 3.17.

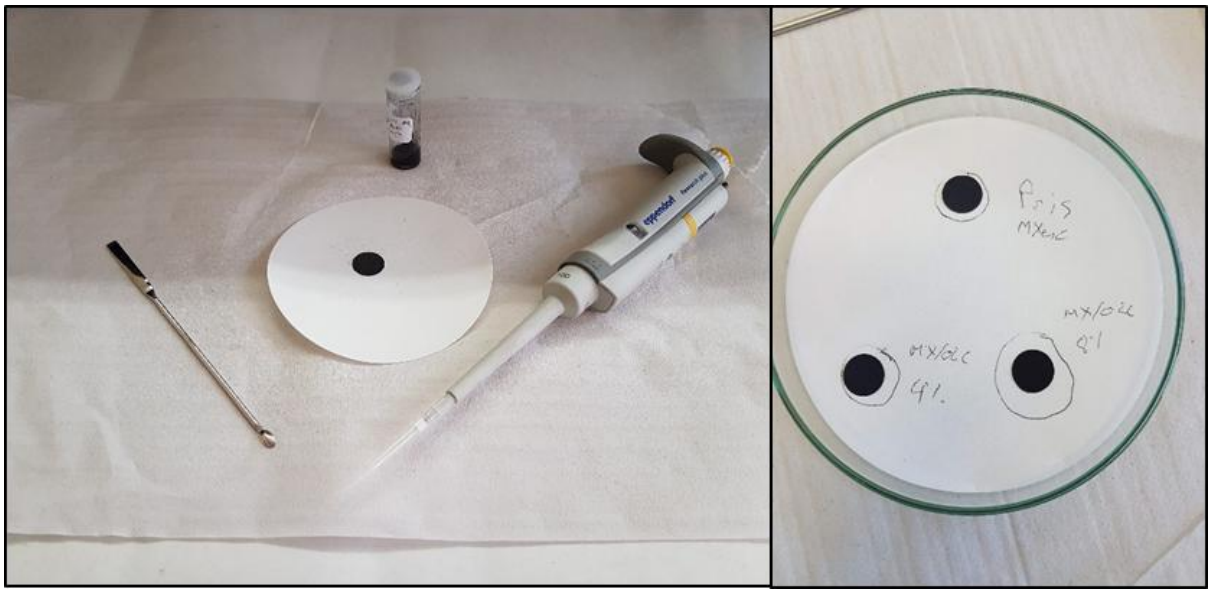

Figure 3.17: An image of the set up used for coating, showing a spatula used for spreading, a filter paper with an electrode placed on it, the sample paste in a vial, and the micropipette used to draw up the paste (left). An image of coated electrodes (right).

### 3.7.5 Preparation of Electrolyte

The potassium hydroxide, $KOH$, (3M) electrolyte was prepared by adding 3.38 g of $KOH$ pellets to 20 ml of ultrapure water. The solution was sonicated for a few minutes until all the pellets were dissolved. Sulfuric acid, $H_2SO_4$, (1M) was also investigated as an electrolyte. $H_2SO_4$ (1M) was prepared by diluting 5.5 ml of 98% purity $H_2SO_4$ in 94.5 ml of ultrapure water. A syringe was then used to draw up around 10 ml of the electrolyte, shown in Figure 3.18.

To convert weight percentage concentration to molarity the following formula was used:

$$M[mol/L] = \frac{(m[g/mol] \cdot w[\%])}{\rho[g/L]}$$

where $M$ is the molar concentration, $m$ is the molar mass, $w$ is the weight percentage concentration, and $\rho$ is the density of the electrolyte.

To calculate the amount of solute or pellets to dilute in water the following formula was used:

$$C_1V_1 = C_2V_2$$

where $C_1$ and $V_1$ are the concentration and volume of the final solution, respectively, and $C_1$ and $V_1$ are the concentration and volume of the solute, respectively. Note that these share the same symbol as those used for capacitance and voltage, however, it will not be necessary to use the above quantities again.

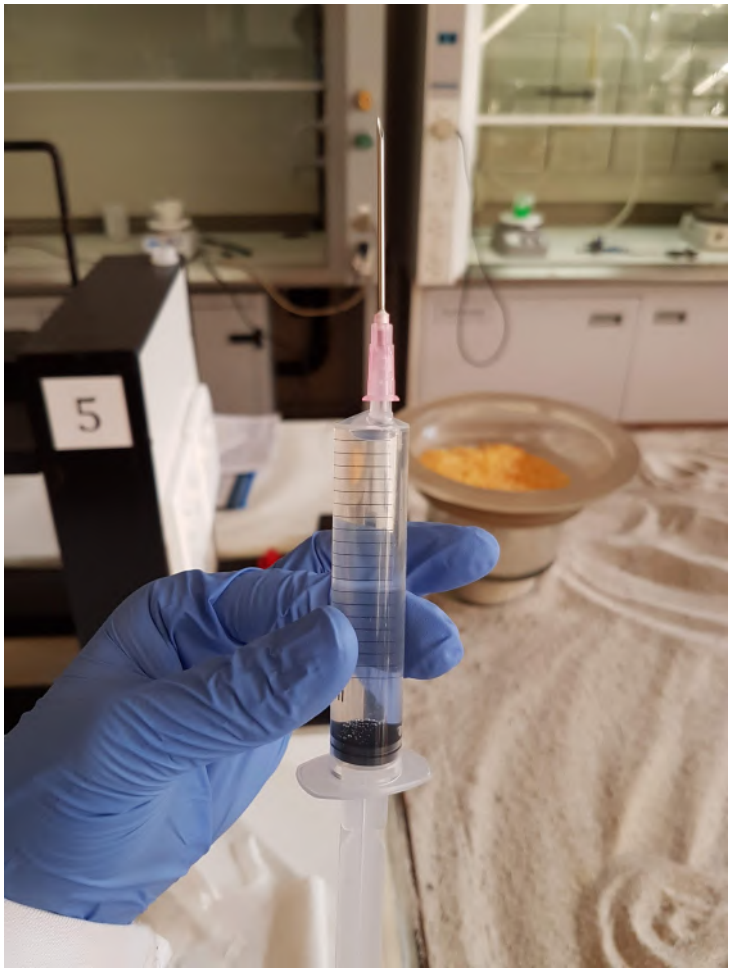


Figure 3.18: An image of a syringe used to draw up 3M KOH electrolyte

### 3.7.6 Assembly of Three Electrode Split Flat Swagelok Cell

The SFC consists of three main components; the lower, middle, and upper cases. Starting with the lower case, the spring is inserted into the bottom cavity. The lower metal pressing plate is inserted on top of

the spring. Two plastic guide sleeves are stacked around the lower metal pressing plate. The middle plate is placed on top of the lower case and screwed in tight. Now the electrodes get placed. First the 16 mm counter electrode (nickel foam) is placed on the lower metal pressing plate. The reference (carbon paper) electrode is a ring with an inner diameter of 16mm and an outer diameter of 20 mm, and is placed on the plastic guide sleeve so that it circles the counter electrode. The 16 mm cell separator is then placed on top of the counter electrode and the 12mm working electrode is placed on top of the cell separator. The upper pressing plate is then placed on top of the working electrode and the upper case is placed on top of this and screwed in tightly. Figure 3.19 shows an image of how all the working parts fit together. The electrolyte is then filled through the top of the upper case, and the cap is then closed tight. Generally enough electrolyte is added so that it overflows slightly as the cap is closed. Care was taken to make sure that the overflowing electrolyte was soaked up immediately. A more effective method of adding electrolyte was to presoak the separator in the elctrolyte to prevent an excess amount from disturbing the positioning of the electrodes.

Figure 3.19: An image of how the working parts of the SFC fit together.

### 3.7.7 Assembly of Three Electrode T-Type Swagelok Cell

The T-type Swagelok consist of three main working parts; the main cylinder, the upper pressing cylinder and the lower pressing cylinder. Figure 3.20 shows the assembly of the cell. During assembly the first step is to shave two lengths of enamelled copper wire with some sandpaper to allow the ends of the wire to conduct a signal. Each wire is then threaded through the lower and upper pressing cylinders, so that each cylinder can now carry a signal from the inside of the cell to the outside. The lower pressing cylinder is then inserted into the cell and a spring is placed ontop of it and it is closed with the lower cap of the cell. Two Whattman glass microfibre separators - which have been presoaked in electrolyte - are sandwiched between the two electrodes. This can either be the working and the counter electrode for the three electrode configuration or the anode and the cathode for the two electrode configuration. This electrode sandwich is then placed in the cell so that it rest on the lower pressing cylinder. The upper pressing cylinder is then inserted into the cell and closed tight. The middle screws are then all screwed in to completely close up the cell. In the case of the three electrode configuration, one of the screws can be threaded with $Ag/AgCl$ wire which can act as the reference electrode. The cell is now ready for electrochemical testing.

The T-type Swagelok was chosen to be the best cell to test the samples with. The primary results in Chapter 4 are from this cell.

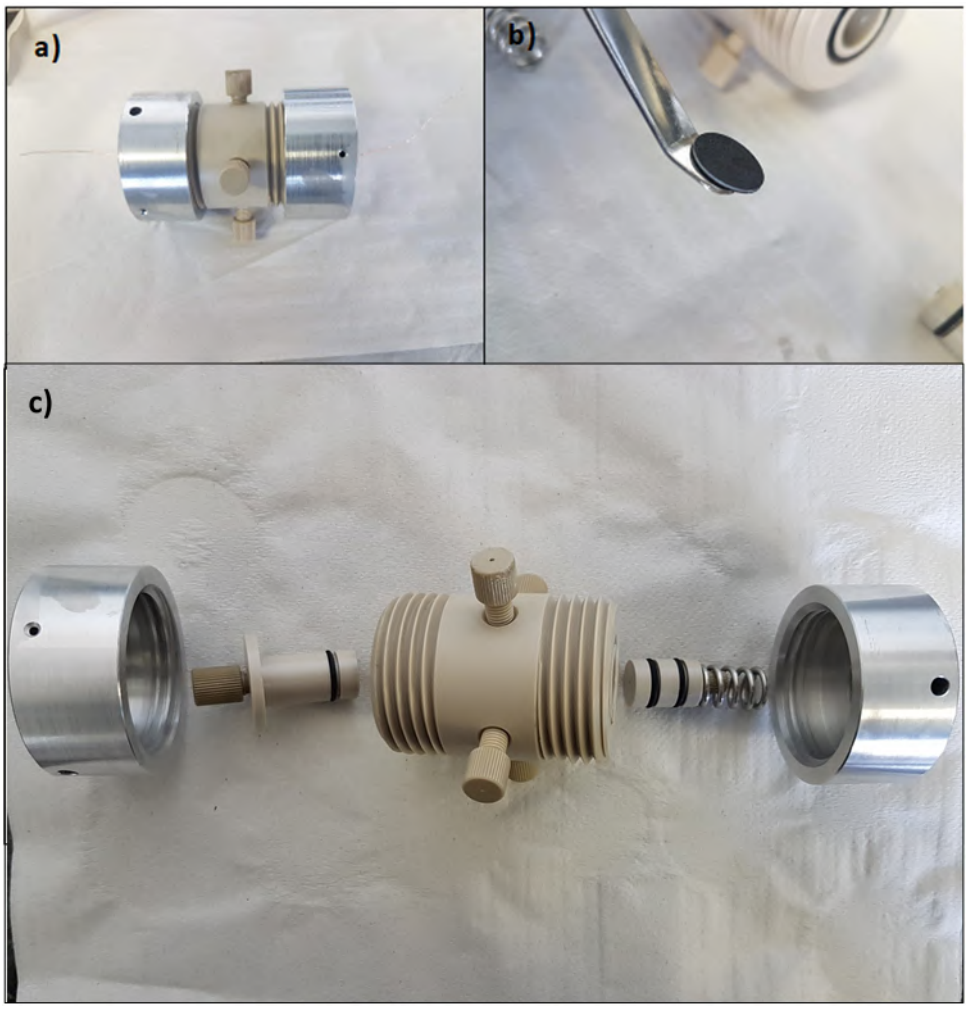


Figure 3.20: An image of the T-type Swagelok: a) closed in 2 electrode configuration, b) separator sandwiched between the anode and cathode, c) showing how to open and close the cell with all its working parts.

## 3.8 Electrochemical Characterisation

Assessing the performance of capacitors is done in many ways. Looking at the equation for capacitance, we see that it is a function of voltage and charge. Experimentally, we can control these variables to characterise the performance of a capacitor. Some of the most popular methods of characterising capacitors are Cyclic Voltammetry (CV), Constant Current Charge Discharge (CCCD) and Electrochemical Impedance Spectroscopy (EIS). All electrochemical characterisation was performed on a Biologic SP300, which can be seen in Figure 3.21.

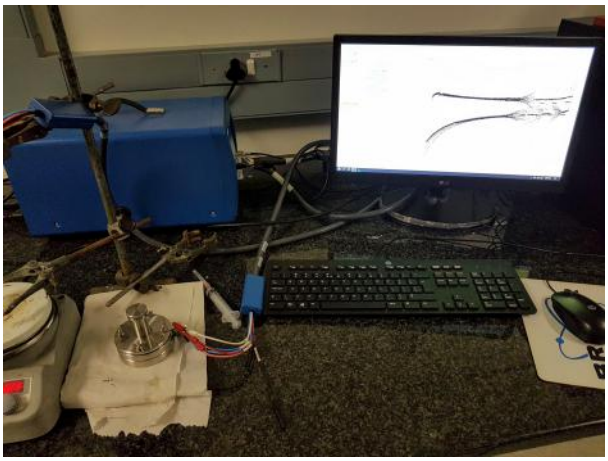

Figure 3.21: An image showing the testing of an SFC using the SP300.

Electrochemical testing was performed on a Biologic SP300 potentiostat at room temperature and included CV, CD, and EIS. The CV measurements were carried out at scan rates ranging from 5 mV/s to 200 mV/s. The CD measurements were carried out at current densities ranging from 0.25 A/g to 10 A/g, and included a cycling test comprising 10000 cycles. The EIS measurements were carried out at frequencies ranging from 100 kHz down to 10 mHz at open circuit voltage pertubation. A Z-fit tool from the EC-Lab software was used for the data analysis.

Properties of interest of the electrodes; specific capacitance, potential window, equivalent series resistance (ESR), energy density, and power density can all be given by the discharge curves if the CD measurements. EIS measurements give details on the charge transfer mechanisms taking place at the electrode-electrolyte interface as well as also provide a measure of the specific capacitance. CV measurements allow for an easy comparison of electrochemical behaviour between different samples and can also be used to get an idea of the specific capacitance and potential windows of the different samples.

Capacitances are given by the following formula for CD, EIS, and CV measurements respectively:

$$C = \frac{I\Delta t}{V_0} \tag{3.3}$$

$$C = -\frac{1}{2\pi f z''} \tag{3.4}$$

$$C = \frac{\int I(V)dV}{\dot{v} \cdot 2V_0} \tag{3.5}$$

where $I$ (A) is the applied current, $V_0$ (V) is the discharge potential window excluding the IR drop, $t$ (s) is the corresponding discharge time, $f$ (Hz) is the frequency, $z''$ ($\Omega$) is the imaginary part of the impedance, $I(V)dV$ is the integration of the area enclosed by the CV divided by two to account for the discharge cycle, $v$ (mV/s) is the scan rate.

The specific capacitance per electrode for a symmetric two electrode system where the properties of each electrode are the same, whether for gravimetric or geometric specific capacitances, is given by the following equation[25]:

$$C_s = \frac{4C}{S} \tag{3.6}$$

where $S$ is the mass (g) or geometric area ($cm^2$) of the electrode, and $C$ is the capacitance measured by any of the techniques discussed above.

In Chapter 1 discussed the power and maximum energy densities, however the following equations detail the very same metrics in more practical units. The gravimetric energy density $E_s$ ($W \cdot h \cdot kg^{-1}$), gravimetric power density $P_s$ ($W \cdot kg^{-1}$), and maximum power density $P_{max}$ ($W \cdot kg^{-1}$) is given by the following Equations 3.7 - 3.9, respectively:

$$E_s = \frac{CV_0^2}{2m} \cdot \frac{1000}{3600} \tag{3.7}$$

where $m$ is the combined mass of both electrodes.

$$P_s = \frac{E_s \cdot 3600}{\Delta t} \tag{3.8}$$

$$P_{max} = \frac{V_0^2 \cdot 1000}{4m \cdot ESR} \tag{3.9}$$

where the ESR ($\Omega$) is determined by looking at the IR drop at the beginning of the discharge curve. When the discharge curve occurs directly after a charging cycle, as is the case in the CD measurements, the ESR is given by Equation 3.10.

$$ESR = \frac{V_{IRdrop}}{2I} \tag{3.10}$$

where the $V_{IRdrop}$ is the voltage drop between the first two points immediately after the current switch.

### 3.8.1 Cyclic Voltammetry

Cyclic Voltammetry is performed by applying a potential across a working electrode and a reference electrode (or the anode and cathode in a two electrode set up) and measuring the resulting current. CV is especially useful for determining making a first order approximation as to the charge storage mechanism of the material. An EDLC will typically have a rectangular curve resembling that of an ideal capacitor, and a PC will depict typical reversible redox curves. However, care must be taken as many PC materials also display a rectangular CV curve, so this method can only be used to see whether redox reactions are occurring within the operating voltage of the tests. CVs are also useful for determining the potential windows (operating voltage) of the material. It is also possible to determine the specific capacitance of the material by integrating the CV curve:

$$C_S = \frac{\Delta Q}{m \cdot \Delta V} = \frac{\int_0^{2V_0/\dot{v}} \mid i \mid dt}{m \cdot 2V_0}$$

To convert the current response of the CV to specific capacitance the following formula is used:

$$C_S \left[\frac{F}{g}\right] = \frac{I[mA]}{\dot{v}\left[\frac{mV}{s}\right] \cdot m[g]}$$

### 3.8.2 Constant Current Charge Discharge

CCCD involves applying a fixed current on the working electrode and then measuring the change in voltage, within the operating voltage range of the material, across the electrodes. This is considered to be the most accurate technique, of the three techniques discussed here, for determining the specific capacitance, the equivalent series resistance (ESR or $R_{ES}$), and the operating voltage of the supercapacitor (SC) material. By integrating the discharge curve one is able to determine the specific capacitance. By looking at the IR drop during the discharge cycle one is able to calculate ESR, and by looking at the shape of the charge and discharge curve one is able to make an estimate as to the operating voltage of the cell, if one is dealing with standard materials with linear responses or hybrid capacitors.

The formula to calculate the specific capacitance from a charge discharge curve is

$$C_S \left[\frac{F}{g}\right] = \frac{I[mA] \cdot t_{discharge}[s]}{m[mg] \cdot V_0[V]}$$

and the ESR is determined by looking at the vertical voltage drop at the discharge curve and using Ohm's Law:

$$R_{ES}[\Omega] = \frac{V_{IR}[V]}{I[A]}$$

### 3.8.3 Electrochemical Impedance Spectroscopy

EIS involves the measurement of a SC's impedance as a function of applied frequency, by providing a low amplitude alternating current with or without a direct current offset. The resulting information is depicted in a Bode plot, which demonstrates the cell response between the phase angle and frequency, and the Nyquist plot, which shows the imaginary and real parts of the impedance of the SC material on a complex plane. For the scope of this study only Nyquist plots have been used for analysis. EIS is a versatile technique which can be used to characterize charge and mass transfer, as well as give an estimate for performance indicators such as specific capacitance and equivalent series resistance. By fitting an equivalent series circuit to the Nyquist plot one can make certain assumptions as to the charge transport mechanisms, where each component of the equivalent series circuit must correspond to a physical feature of the system itself.

# Chapter 4

# Results

Measurements using the following physical characterisation techniques were obtained:

- X-ray Diffraction (XRD)
- Raman Spectroscopy (Raman)
- Scanning Electron Microscopy (SEM)
- Transmission Electron Microscopy (TEM)
- Brunauer–Emmett–Teller (BET) surface area analysis
- X-ray Photoelectron Spectroscopy (XPS)

These will be discussed and analysed. The performance of the sample materials were assessed using the following electrochemical techniques:

- Cyclic Voltammetry (CV)
- Constant Current Charge/Discharge (CD)
- Electrochemical Impedance Spectroscopy (EIS)

These will also be discussed and analysed.

## 4.1 Physical Characterisation

### 4.1.1 X-ray Diffraction

Figure 4.1 shows the XRD results of (a) the MAX phase $Ti_2AlC$, (b) the MXene $Ti_2CT_X$, (c) $Ti_2CT_X/OLC$ (5% doping), and (d) $Ti_2CT_X/OLC$ (10% doping). The main peaks in (a) are the two peaks at around 10° and 15°, and the broad peak at around 45°. The smaller of the two peaks corresponds to the (002) layer of the MAX phase $Ti_3AlC_2$, of which there are trace amounts in the precursor material sourced [19]. The more significant peak corresponds to the (002) layer of the MAX phase $Ti_2AlC$. The broad peak at 45° corresponds to the aluminium layer in the MAX phase [19] . In the MXene XRD patterns, (b) - (d), notice that this broad peak has completely disappeared, indicating the successful transformation from MAX phase to MXene. In addition to this, in the MXene patterns both show the shifting of the (002) peak to a lower $2\theta$ angle, which indicates a larger interlayer spacing in accordance to the Bragg equation (Equation 3.1), resulting from the removal of the Al atoms and the formation of functional group terminations, i.e. F, O, or OH groups [11]. In particular, the peak appears to comprise two separate peaks which are very close together, at $2\theta$ values of $7.5° \pm 0.3°$ and $8° \pm 0.3°$. The presence of two peaks was also observed by Liu et al (2016) [18]. These two peaks indicate the presence of two basal planes with interlayer distances of 6.86 nm ± 0.5 nm and 6.43 nm ± 0.2 nm respectively. These distances are higher than those reported in the paper by Liu et al (2016), and the reason for this is most likely the extended etching time used in this study, i.e. 96 hours instead of 48 hours. The longer etching time is likely to have allowed the *in situ* formed HF to etch the MAX phase more effectively.

Figure 4.2 shows a zoomed in region of plots (b)-(d) from Figure 3.6, where the amorphous carbon from the OLC should be apparent as very broad amorphous peaks that would look like increased noise. However, it is difficult to discern any noticeable difference between samples in Figure 4.2. The success of the OLC doping will be more noticeable from the Raman Spectroscopy results.

The rest of the peaks in the MXene patterns indicate the presence of $TiC$ and $TiO_2$ phases as indexed in Figure 4.1.

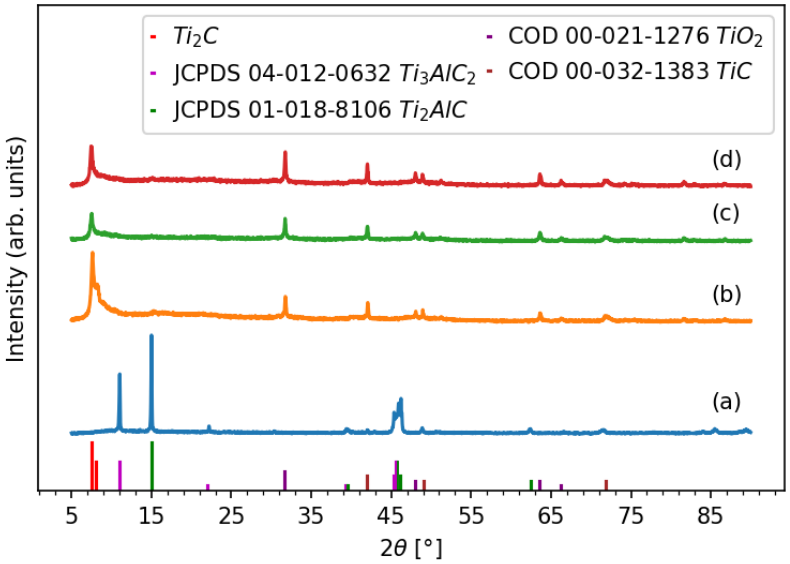


Figure 4.1: XRD patterns for a) MAX phase precursor, b) MXene synthesized from etching the MAX phase, c) 5% OLC doped MXene, and d) 10% OLC doped sample.

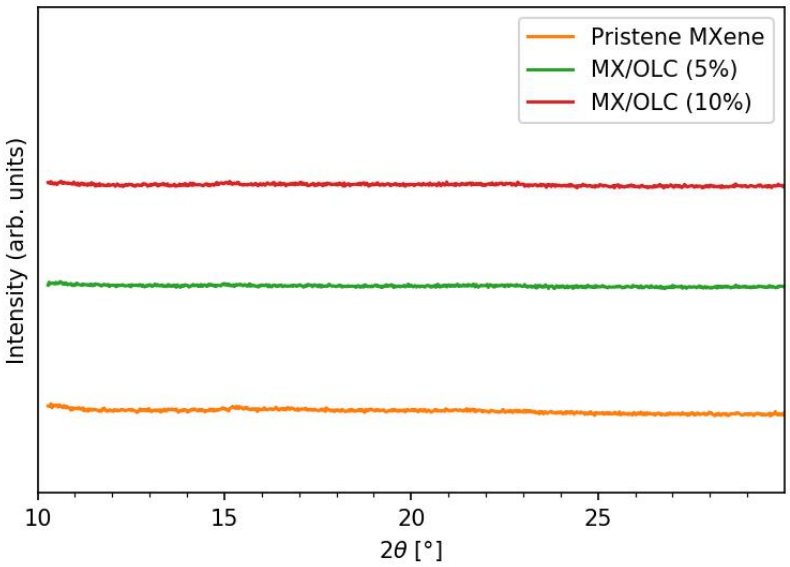


Figure 4.2: Zoomed in image of the section of the XRD patterns for the MXene and OLC doped samples where the amorphous carbon region should appear. It is difficult to discern any noiticeable difference between samples.

### 4.1.2 Raman Spectroscopy

Figure 4.3 shows the Raman spectra of the materials and samples prepared in this work. Most notable is the shifting of the $\omega_{1-4}$ peaks from (a) in (b),(d), and (e). These peaks are the characteristic peaks of $Ti_2AlC$ [31], and occur at $147cm^{-1}$, $265cm^{-1}$, and $361cm^{-1}$ respectively. The change in wavenumber of these peaks, taken together with the previous XRD results, lead us to infer that Al has been removed from the MAX phase and replaced with another atom(s). There is also the appearance of the $\omega_5$ peak in the MXene plots. This peak is attributed to non-stoichiometric $Ti_xC_y$ which forms as a by-product of the etching process during synthesis[19]. The appearance of $\omega_{6-7}$ at $1280cm^{-1}$ and $1500cm^{-1}$ in all the spectra except (a) correlate to the D and G bands, which indicates the appearance of free carbon in the material. The D band is indicative of disordered graphitic structures, and the broadness of the peak indicates that there is a small amount of disordered carbon in the MXene [19]. This is further indication of the successful etching process as it is quite a rough process in the sense that forcibly removing an element from the material would also cause some disorder to the remainder of the structure, albeit much less so.

Figure 4.3(c) shows the Raman spectrum for OLCs. The spectrum features very prominent D and G bands, which are characteristic of OLCs [7] due to the $sp^2$ hybridised carbon ordering. These bands feature more strongly in the OLC doped samples ((d) and (e)), due to the presence of OLC in the sample. In particular the intensity is stronger in the 10% doped sample compared to the 5% doped sample. The peaks have been slightly upshifted in (d), indicating that the nanoparticles have been intercalated successfully and have adsorbed to the MXene surface, thereby resulting in a slight energy shift in the scattered photons.

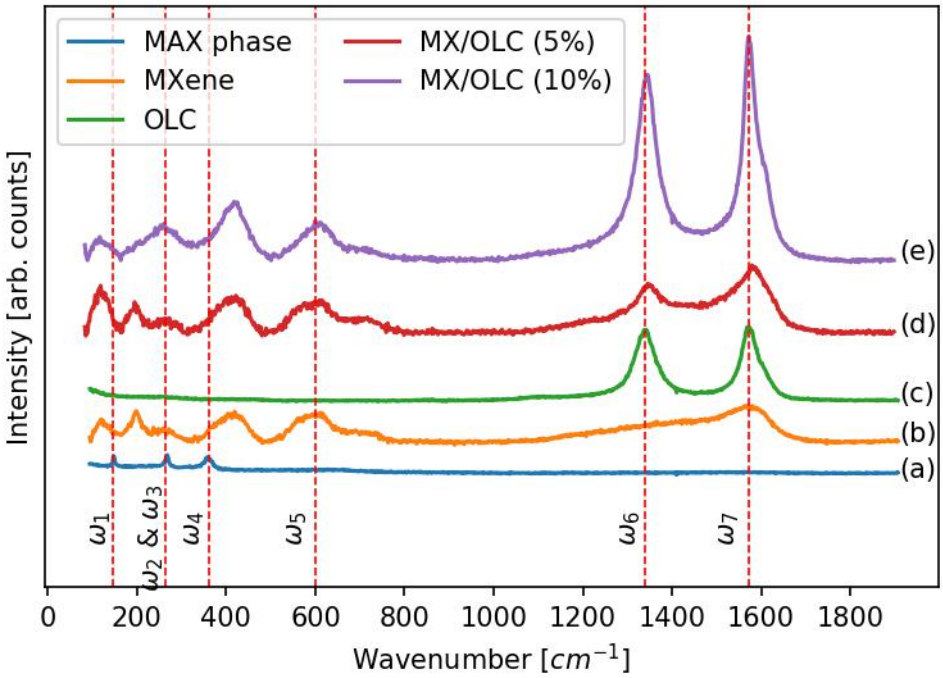


Figure 4.3: Raman spectra of a) MAX phase precursor, b) Pristine MXene, c) OLCs d) 5% OLC doped MXene, and e) 10% OLC doped MXene.

### 4.1.3 Brunauer–Emmett–Teller (BET) surface area analysis

Figure 4.4 contains the plot of the isotherm for the pristine MXene sample. Using the analytical procedure outlined in Chapter 3 (Equation 3.2) the specific surface area (SSA) of the pristine sample was calculated to be 18 $m^2/g \pm 0.2$ $m^2/g$ . It was not possible to measure the BET isotherms for the OLC doped samples because 200 mg of sample are required per measurement, and due to material scarcity the doped samples were not synthesized in sufficient quanitities to allow for this. However, since the SSA of the OLCs

themselves is known (390 $m^2/g$ for OLCs sythesized at 1300 °C) it is possible calculate an estimate for the maximum SSA of the doped samples using the weight percentages of the OLCs. Table 4.1 shows these estimates. These actual SSA of the doped samples is likely to be lower than these estimates since the addition of OLCs may block access to existing active sites or the active sites created by other OLC particles.

| **Sample** | **BET maximum SSA** ($m^2/g$) |
|---|---|
| Pristine MX | 18 (measured) |
| MX/OLC (5%) | 37 (estimated) |
| MX/OLC (10%) | 55 (estimated) |

Table 4.1: Estimates of the BET surface area for samples used in this work.

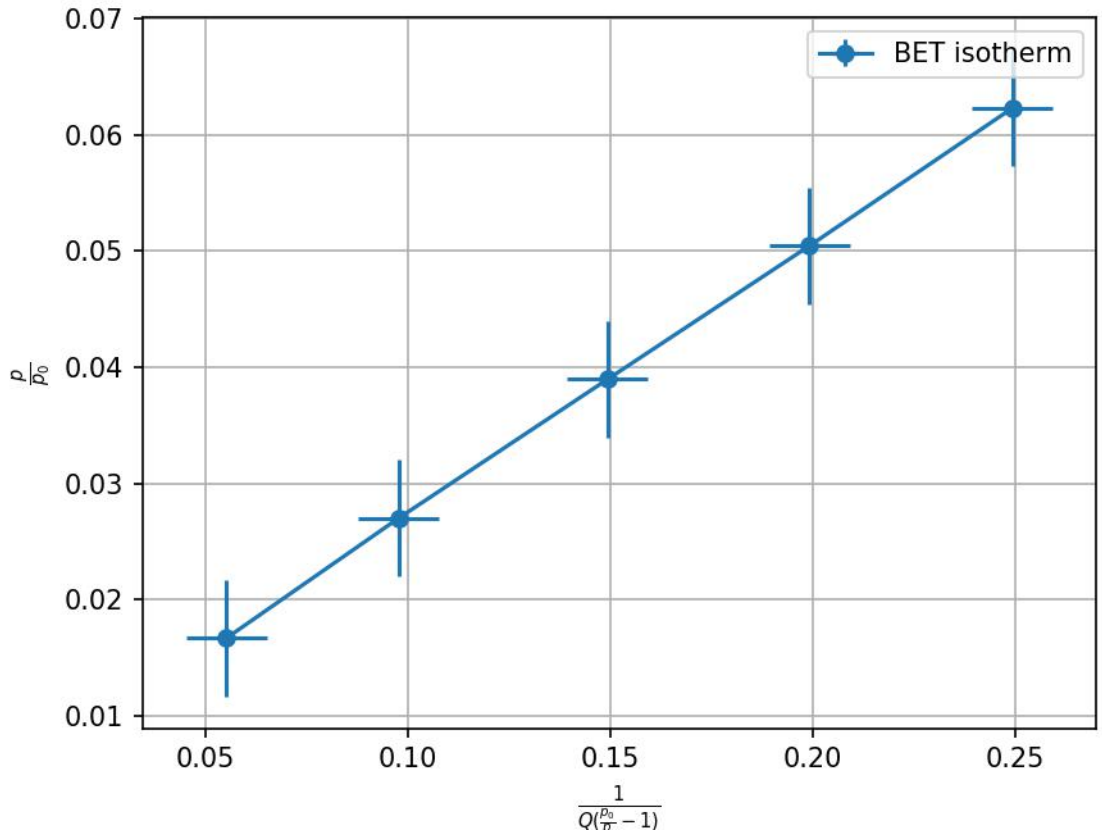


Figure 4.4: Plot of the BET isotherm for the pristine MXene sample.

### 4.1.4 Scanning Electron Microscopy

Figure 3.8 contains SEM images of (4.5a) pristine MXene, (4.5b) OLCs, and (4.5c) OLC doped MXene. As can be seen in (4.5a)there is a clear accordion like layered structure present in the pristine material. Alos present are what appear to look like spots which we would expect from a doped material. It is thought that these spots might in fact be the remnants of other MAX phase sheets which have been 'over-exfoliated' as the synthesis procedure was carried out at double the usual length compared to most literature [12], [15], [18].

In contrast the OLCs (4.5b) are very difficult to make out using the SEM instrument available. One can just about make out some sort of agglomerated structure at the 100 nm scale of the image, which lends some credence to the idea that the OLC powder consists of particles with a diameter ranging from 5

nm to about 50 nm, as is expected for the OLCs used in this study (refer back to Section 2.3 for more details).

Due to the presence of what may very well be the sheet remnants in the pristine sample, it is very difficult to see the OLC particles in the OLC doped MXene (Figure 4.5c).

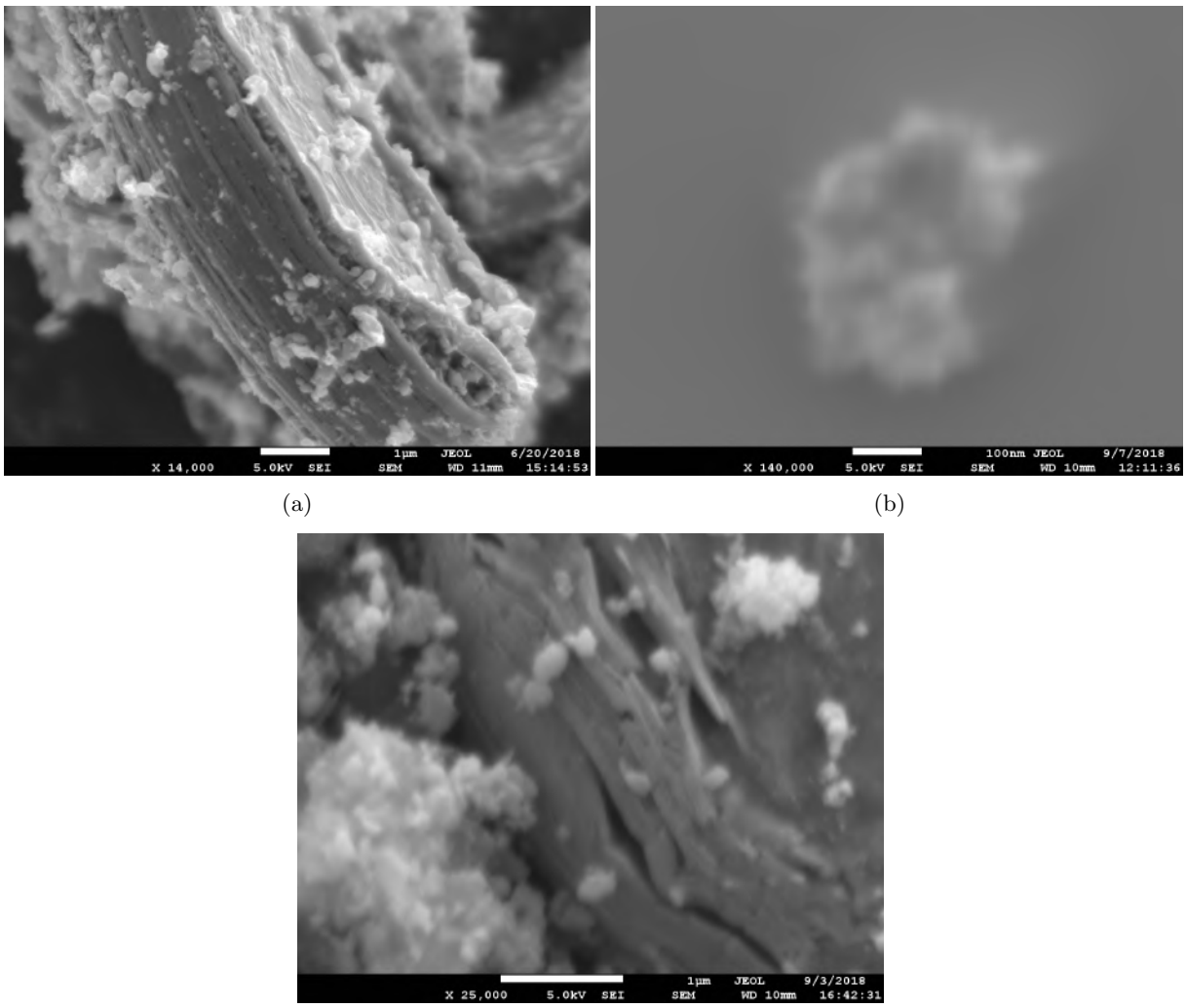


(a) (b)

(c)

Figure 4.5: SEM images of a) Pristine MX, b) OLC c) OLC doped MXene (10%)

### 4.1.5 Transmission Electron Microscopy

Figure 4.6 contains TEM images of the samples used in this study. In Figure 4.6a a low magnification image of a MXene multilyered structure is shown. It is clear that there are very well defined layers present, and careful inspection reveals that each defined layer is further subdivided into its own many layers, reminiscent of the multilayered structure discussed in Chapter 2. Figure 4.6b a higher magnification image is shown, showing two key features. The first of these is several layers in the structure indicated by the different gradients in the TEM image, and the second is a few distinnct spots. These spots correlate with the SEM observations of the pristine material, and may very well be the remnants of layers that were destroyed in the etching process. It is also clear that these spots are present inside the structure itself, and may possibly increase the interlayer distance as well as the stability of the interlayer spacing, similarly to what is expecetd of the OLCs themselves.

Figure 4.6c shows a TEM image of the OLC sample. Again two features are of interest. The first is the fairly large rounded objects which are rpesent at the edges of the structure. These are thought to be larger OLC particles ($\sim$ 50 nm in diameter). The second feature of interest is the presence of much smaller circular objects on the edges of the structrure. These are thought to be much smaller

OLC particles ($\sim$ 5 - 10 nm in diameter). The presence of both these features show agreement with the literature discussed in Chapter 2, stating that in samples of OLCs that have been synthesized in temperatures arounf 1300°C it is to be expected that the diameter of the particles will vary in this range.

Figure 4.6d shows a TEM image of the 5% OLC doped sample. As stated earlier, the presence of what is likely the sheet remnants is clearly visible in the MXene sample. This makes it difficult to discern from a SEM or TEM image if the spots present in the material are the supposed sheet remnants or in fact the OLCs. However, other if we are to take these images in the context of the other characterisation results (XRD, Raman, XPS) it is highly likely that the spots in Figure 4.6d are a combination of those seen in Figure 4.6b as well as te OLCs in Figure 4.6c. This is further evidence suggesting the successful intercalation of OLCs in the MXene structure. It is also important to note that these OLCs have both intercalated into the layers but also adsorbed onto the surface of the MXene structure.

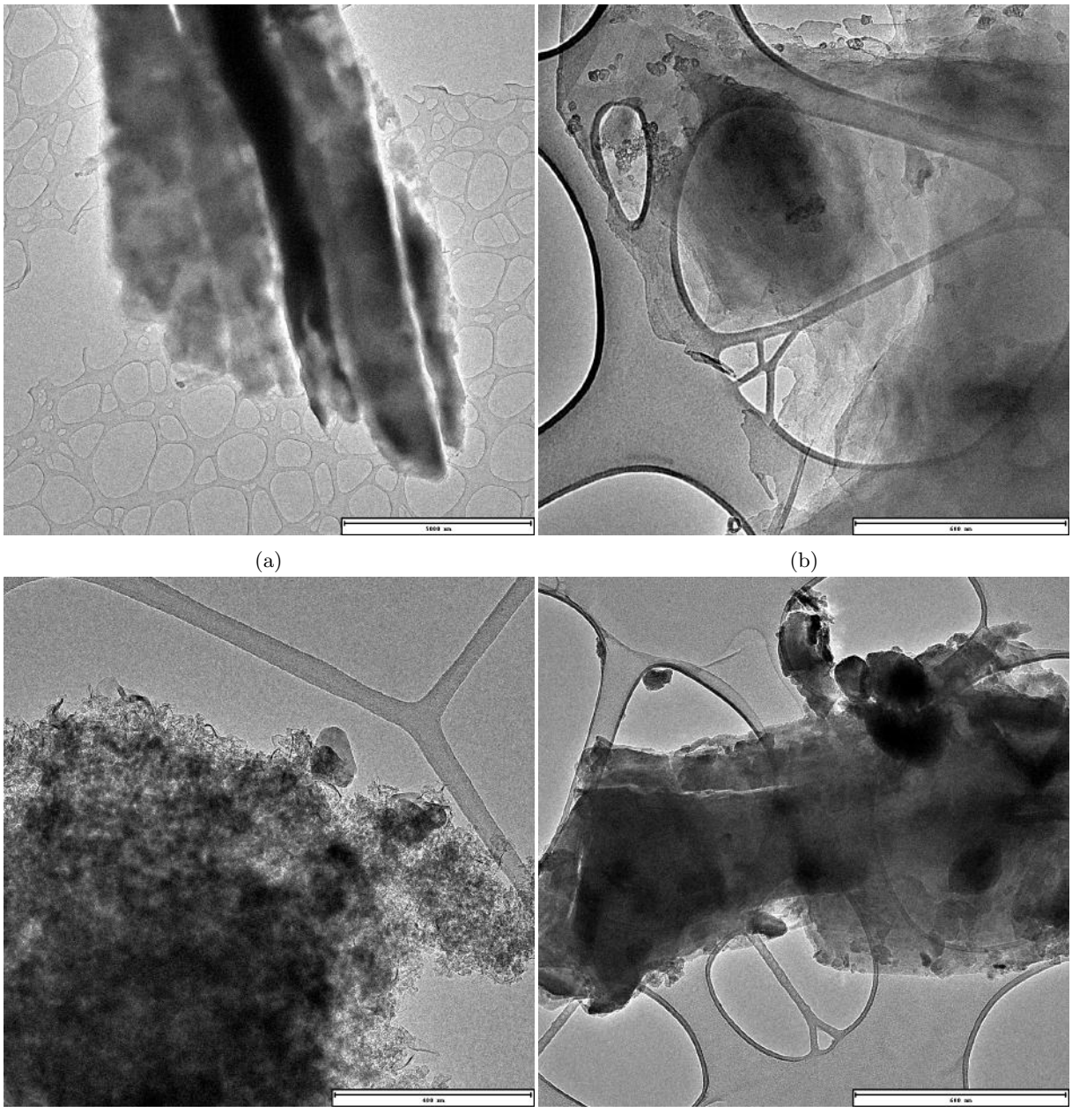

(a) (b)

(c) (d)

Figure 4.6: TEM images of (a) Pristine MXene sheets at low magnification, (b) Pristine MXene sheets at higher magnification, (c) agglomerated OLCs showing the different diameters, (d) 5% OLC doped Mxene.

### 4.1.6 X-ray Photoelectron Spectroscopy

Figure 4.7 displays survey scan XPS measurements for the Pristine MXene, 5%, and 10% OLC doped samples. Indicated clearly in the image are the peaks associated with the the Ti 2p, C 1s, O 1s, and F 1s orbitals in all samples. High resolution scans were taken of these peaks and are shown in Figures 4.8 and 4.9. The fitting was performed using Gaussian deconvolution using the Scipy package in Python, and all fits exhibited an $R^2$ value $< 1$.

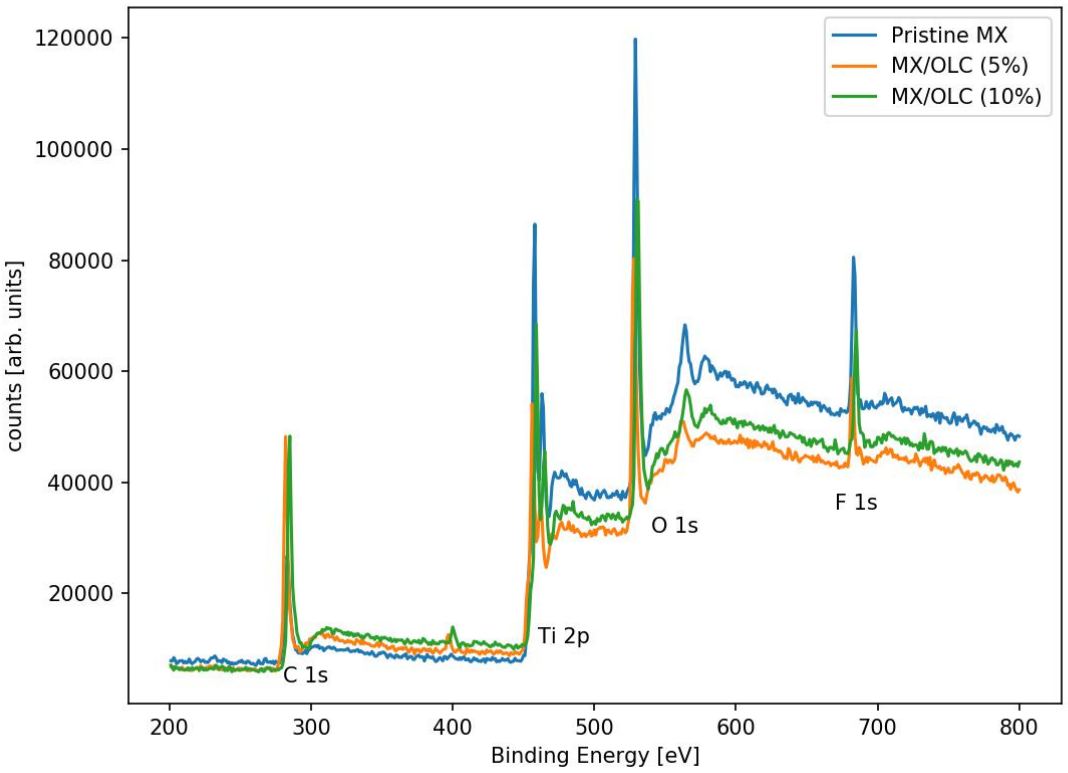


Figure 4.7: An XPS survey scan measurement of the Pristine MXene, 5%, and 10% OLC doped samples. Shown are the Ti 2p, C 1s, O 1s, and F 1s peaks in each sample.

Table 4.2 shows the corresponding atomic and mass concentration of the elements for the pristine MXene sample. By looking at the atomic concentration one can see that the MXene is mostly carbon and oxygen, and has much higher concentrations of titanium when compared to the literature [19]. This is most likely due to the prolonged etching time as well as the use of the LiF + HCl synthesis method as opposed to direct immersion in HF. We can also see that the Pristine sample has a higher oxygen concentration and a lower fluorine concentration when compared to the literature, which is actually much more favourable as recent literature reports that the presence of oxygen functional groups in place of fluorine promotes higher capacitance [15].

| **Element** | **Atomic conc. [%]** | **Error [%]** | **Mass conc. [%]** | **Error [%]** |
|---|---|---|---|---|
| **Ti 2p** | 19,59 | 0,40 | 44,09 | 0,62 |
| **C 1s** | 31,80 | 0,87 | 17,95 | 0,58 |
| **O 1s** | 38,64 | 0,72 | 29,05 | 0,54 |
| **F 1s** | 9,97 | 0,58 | 8,90 | 0,52 |

Table 4.2: Atomic and mass percentages of each element present in the pristine MXene sample.

Figure 4.8 contains the high resolution scan regions for the Pristine MXene sample. The high resolution

scan around the Ti 2p peak (Figure 4.8a) reveals four deconvoluted peaks. A comparison with a paper by Melchior et al (2018) [19] and a paper by Shah et al (2017) [34] reveals that $Ti_1$ corresponds to the presence of Ti-C (7.48%), $Ti_2$ corresponds to $Ti^{3+}$ (49.26%), $Ti_3$ corresponds to $Ti - O$ (13.85%), and $Ti_4$ corresponds to $C - Ti - F_x$ (29.41%). There does however seem to be the absence of $Ti^{2+}$ in this scan, and it may in fact be hidden with the $Ti_1$ peak. If this is the case then it contributes very little to the overall curve. The Ti-C signal correlates with the appearance of TiC in the XRD results (Figure 4.1), and may also come from the bulk material. $Ti^{3+}$, and if present $Ti^{2+}$, may arise from the formation of different mixed oxides and carboxides on the MXene surface [19]. The Ti-O signal correlates with the $TiO_2$ peaks found in the XRD, and may have formed during the drying process.

Figure 4.8b shows the high resolution scan around the C 1s peak, revealing four fitted Gaussian peaks. According to the literature ([19], [34]) $C_1$ corresponds to C-Ti (8.65%), $C_2$ corresponds to C-C for $sp^2$ carbon (71.73%), $C_3$ corresponds to C-C for $sp^3$ carbon (9.64%) [35], and $C_4$ corresponds to O = C-O (9.98%). The C-Ti signal likely correlates to the Ti-C peak observed in Figure 4.8a. The C-C signal likely arises from the graphitic carbon formed during the etching process [34] and the O = C-O signal may be present due to some residual organic compounds that were not removed during the washing process [19].

Figure 4.8c shows the high resolution scan around the C 1s peak, revealing two fitted Gaussian peaks. A comparison with the literature ([19], [34]) reveals that the $O_1$ peak corresponds to the presence of $TiO_2$ (50.06%). The $O_2$ peak corresponds to $C - Ti - O_x$ (49.94%). Melchior et al (2018) also observed a third peak which was thought to arise from the presence of $C - Ti - (OH)_x$, which is absent in this sample. This likely means that there is very little OH group terminations on the MXene surface, and that the surface terminations are dominated by F and O groups.

Figure 4.8d shows the high resolution scan around the F 1s peak, revealing two fitted Gaussian peaks. A comparison with the literature ([19], [34]) reveals that $F_1$ and $F_2$ are likely attributed to $C - Ti - F_x$ (64.62%) and $AlF_x$ (35.38%) respectively. The $C - Ti - F_x$ corresponds to the $Ti_4$ signal observed in Figure 4.8a and likely indicates fluoride surface terminations. The $AlF_x$ signal is surprisingly large and may in fact stem from etching residues which were not washed away. A similar observation for both these signals was observed by Melchior et al (2018) [19].

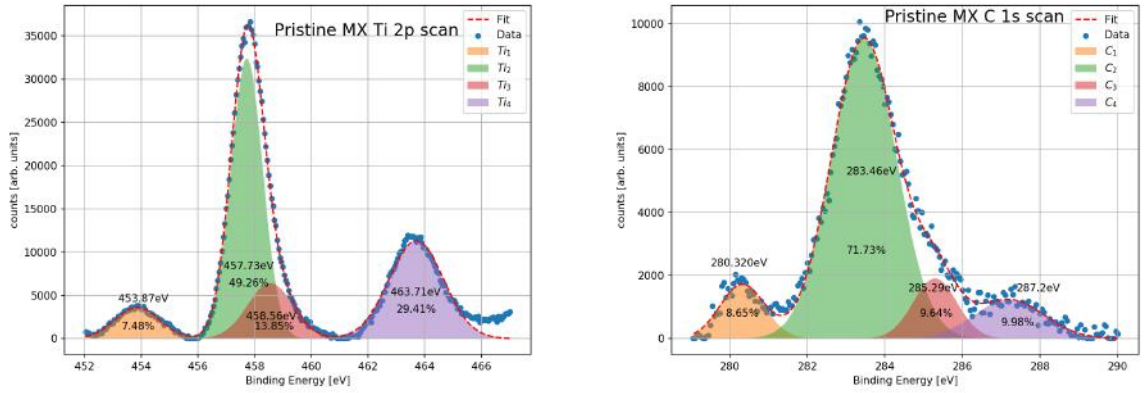


(a) (b)

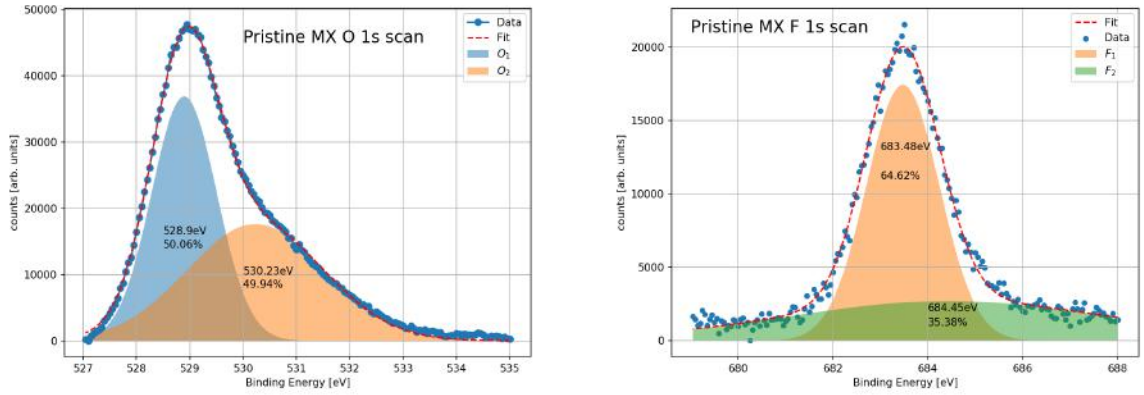


(c) (d)

Figure 4.8: High resolution scans of pristine MXene around the a) Ti 2p peak, b) C 1s peak, c) O 1s peak, and d) F 1s peak.

Tables 4.3 and 4.4 show the atomic and mass concentrations of the 5% and 10% OLC doped samples. The only significant difference is the increase in atomic and mass concentrations of the C 1s in the doped samples. This is expected as more carbon in the form of the OLCs has been added to the material. It is interesting to note that the atomic and mass concentrations are within the error margins of each other. This is most likely because the 5% and 10% doping quantities are not high enough for the instrument to detect a difference, which is not completely unexpecetd given that XPS is a surface science technique and is limited to taking measurements over very small areas in a sample.

| **Element** | **Atomic conc.** [%] | **Error** [%] | **Mass conc.** [%] | **Error** [%] |
|---|---|---|---|---|
| **Ti 2p** | 11,18 | 0,31 | 30,69 | 0,67 |
| **C 1s** | 57,78 | 0,87 | 39,80 | 0,78 |
| **O 1s** | 25,08 | 0,75 | 23,02 | 0,69 |
| **F 1s** | 5,96 | 0,57 | 6,50 | 0,62 |

Table 4.3: Atomic and mass percentages of each element present in the MX/OLC (5%) sample.

| **Element** | **Atomic conc.** [%] | **Error** [%] | **Mass conc.** [%] | **Error** [%] |
|---|---|---|---|---|
| **Ti 2p** | 11,44 | 0,31 | 31,06 | 0,66 |
| **C 1s** | 55,84 | 0,86 | 38,03 | 0,78 |
| **O 1s** | 25,58 | 0,66 | 23,20 | 0,58 |
| **F 1s** | 7,15 | 0,56 | 7,70 | 0,59 |

Table 4.4: Atomic and mass percentages of each element present in the MX/OLC (10%) sample.

Figures 4.9 contains the high resolution scan images for the 5% and 10% OLC doped samples. All scans contain the same signature peaks present in the pristine MXene sample (Figure 4.8), however, there are slight differences in these peaks.

Figures 4.9a and 4.9b shows the high resolution scan for the Ti 2p peak for the 5% and 10% OLC doped sample, respectively. By looking at the percentage of photoemission one can see that the $Ti_1$ and $Ti_2$ peaks contribute a slightly higher proportionate signal to the overall curve compared to the pristine MXene (Figure 4.8a). This indicates that there is a slight increase in the proportion of TiC and carboxides on the MXene surface, which agrees with the introduction of more carbon to the sample.

Figure 4.9c and 4.9d shows the high resolution scan for the C 1s peak for the 5% and 10% OL doped sample, respectively. The most notable difference in the C 1s scans is the relative increase in the $C_3$ and $C_4$ signals. This indicates that there is a higher proprtion of $sp^3$ hybridised carbon in the OLC doped

samples, and is likely because the OLCs used in this work were synthesized at 1300°C, meaning that the OLCs are only partially graphitised.

Figure 4.9e and 4.9f shows the high resolution scan for the O 1s peak for the 5% and 10% OL doped sample, respectively. The main difference in the O 1s peaks is the $\sim$ 10% increase in the proportional strength of the $O_2$ signal, indicating a higher proportion of oxygen terminations as opposed to $TiO_2$, which may have occurred during the OLC intercalation process.

Figure 4.9g and 4.9h shows the high resolution scan for the F 1s peak for the 5% and 10% OLC doped sample, respectively. While 4.9h shows little to no change from the pristine MXene sample (Figure4.8d) as expected since no fluorides were added, Figure 4.9g shows two distinct peaks which seem to have split up from the central peaks in Figure 4.8d and 4.9h. The cause for this is unknown, and may have been a sampling error during the measurement. Unfortunately due to the difficulty of procuring XPS measurement time it was not possible to repeat the experiment within the time frame of this dissertation.

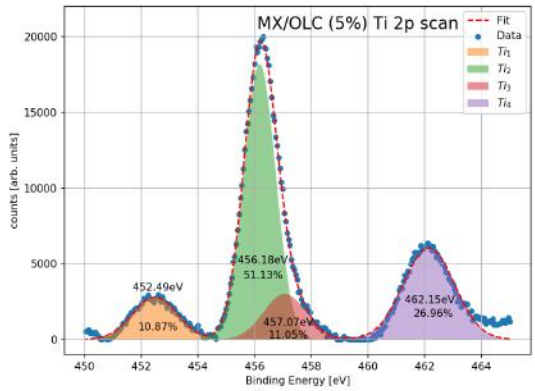


(a)

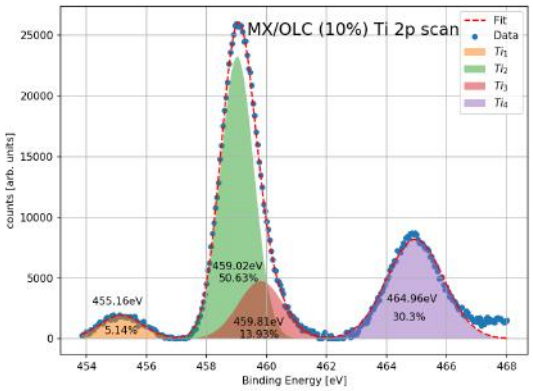


(b)

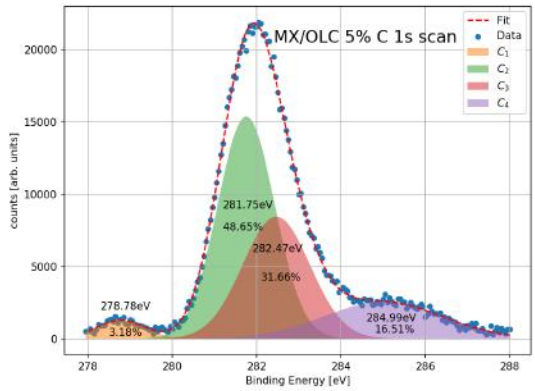


(c)

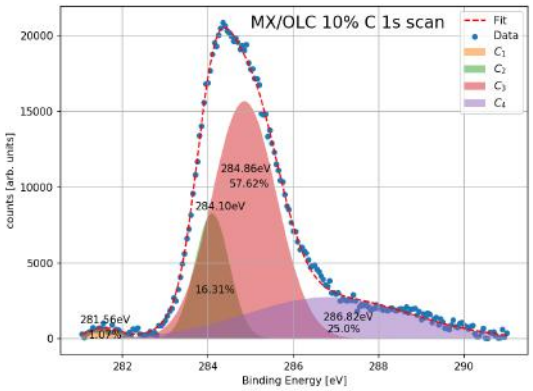


(d)

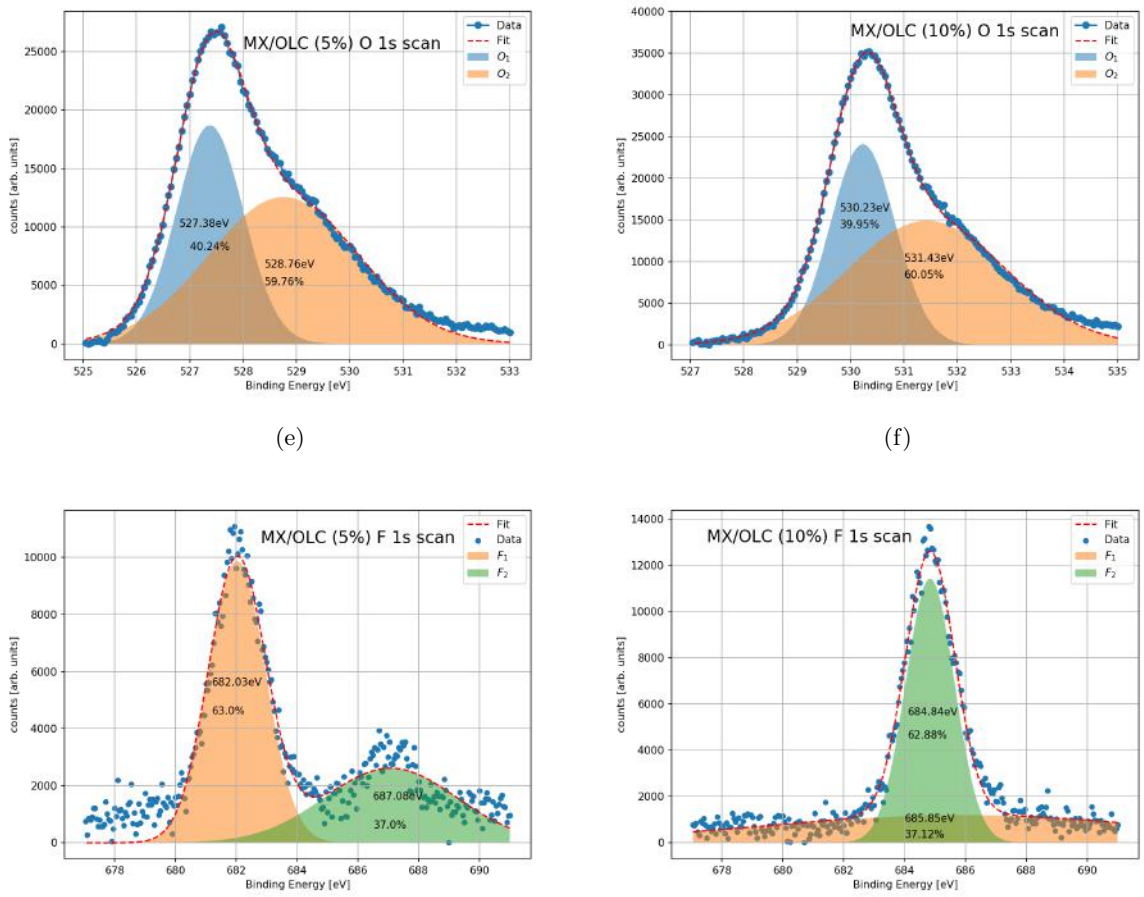


Figure 4.9: High resolution scans of OLC doped MXene around the a-b) Ti 2p peak, c-d) C 1s peak, e-f) O 1s peak, and g-h) F 1s peak.

## 4.2 Electrochemical Characterisation

Table 4.5 provides a list of the electrochemical experiments performed. Each experiment consists of those outlined in the Section 3.8, and the table provides the configuration used (three electrode or two electrode), the material under study, and the electrolyte used. Of all these experiments, using the two electrode Swaglok T-type configuration proved to be the most reliable method (highlighted in green). The mass loadings for these experiments were 3.28 mg $\pm$ 0.005 mg, 3.04 mg $\pm$ 0.005 mg, and 3.28 mg $\pm$ 0.005 mg for the pristine sample, 5% doped sample, and 10% doped sample respectively.

In particular, the screen printed electrode method proved to be unreliable because of the high uncertainty on the mass loading of the active material, as it required a very small amount of sample to be dropped onto the electrode. The MNRs themselves were shown to yield very low capacitances compared to the pristine material when the measurements were repeated on the SFC, and so they were subsequently abandoned as a viable avenue. It is thought that one of the reasons for this was that during synthesis it was not possible to reach a high enough RPM on the shaker instrument used. An RPM of 150 was used as opposed to the 250RPM used in the study by Lian et al (2017) [20].

It was also decided to pursue the use of $H_2SO_4$ as the electrolyte in this study because of it's higher ionic conductivity. Gogotsi et al (2017) has also shown repeatedly that this electrolyte produces a much higher current repsonse when compared to 3M KOH [15]. However, the use of this electrolyte seemed to compromise the integrity of the SFC results as severe corrosion was noticed during these experiments. As a result, it was decided to use the Swagelok T-type cell to conduct the electrochemical measurements, and since by this point enough preliminary data had been acquired which indicated the efficacy of both

the materials under study and the chosen electrolyte it was decided that only the two electrode results were necessary to characterise the performance of the material. The purpose of the three electrode results was only to guide the research process, and would not have provided a good indication of the materials capacity for practical applications [25].

| **Configuration** | **Active Material** | **Electrolyte** |
|---|---|---|
| 3 Electrode Screen Printed | $Ti_2CT_X$ | 3M KOH |
| 3 Electrode Screen Printed | $Ti_2CT_X$ KOH MNR | 3M KOH |
| 3 Electrode Screen Printed | $Ti_2CT_X$ $NH_4OH$ MNR | 3M KOH |
| 3 Electrode Swagelok Flat | $Ti_2CT_X$ KOH MNR | 3M KOH |
| 3 Electrode Swagelok Flat | $Ti_2CT_X$ $NH_4OH$ MNR | 3M KOH |
| 3 Electrode Screen Printed | $Ti_2CT_X$ / OLC (10%) prepared in DMF | 3M KOH |
| 3 Electrode Swagelok Flat | $Ti_2CT_X$ | 3M KOH |
| 3 Electrode Swagelok Flat | $Ti_2CT_X$ / OLC (10%) prepared in DMF | 3M KOH |
| 3 Electrode Swagelok Flat | $Ti_2CT_X$ / OLC (5%) | 3M KOH |
| 3 Electrode Swagelok Flat | $Ti_2CT_X$ | 1M $H_2SO_4$ |
| 3 Electrode Swagelok Flat | $Ti_2CT_X$ / OLC (10%) | 1M $H_2SO_4$ |
| 3 Electrode Swagelok Flat | $Ti_2CT_X$ / OLC (5%) | 1M $H_2SO_4$ |
| 3 Electrode Swagelok T-type | $Ti_2CT_X$ | 1M $H_2SO_4$ |
| 3 Electrode Traditional Beaker | $Ti_2CT_X$ | 1M $H_2SO_4$ |
| 2 Electrode Swagelok Flat | $Ti_2CT_X$ | 1M $H_2SO_4$ |
| 2 Electrode Swagelok Flat | $Ti_2CT_X$ / OLC (5%) | 1M $H_2SO_4$ |
| 2 Electrode Swagelok Flat | $Ti_2CT_X$ / OLC (10%) | 1M $H_2SO_4$ |
| 2 Electrode Swagelok T-type | $Ti_2CT_X$ | 1M $H_2SO_4$ |
| 2 Electrode Swagelok T-type | $Ti_2CT_X$ / OLC (5%) | 1M $H_2SO_4$ |
| 2 Electrode Swagelok T-type | $Ti_2CT_X$ / OLC (10%) | 1M $H_2SO_4$ |

Table 4.5: Summary of most of the electrochemical experiments performed in this study, excluding all reproducability tests.

### 4.2.1 Activation

The sample's electrochemical prooperties were first explored using CV at 20 mV/s. Often in materials the sample needs to first be activated by allowing ion diffusion to occur for a number of cycles. A CV is usually run several times until a stable CV is obtained. This is a common practice in any scientific experiments to ensure that one is observing the true picture of the material's behaviour [25]. In this work the sample was activated using techniques in the following order:

1. CV for 10 - 20 cycles at 20 mV/s
2. CCCD at 1 A/g

Figure 4.10 shows the CV plots of the first few cycles at 20 mV/s and after cycling at 1 A/g for a few cycles, for the three samples under study; (4.10a) Pristine $Ti_2CT_X$, (4.10b) $Ti_2CT_X$//OLC (5%), and (4.10c) $Ti_2CT_X$//OLC (10%). It is clear from the the figures that there is a definite increase in area under the CV in all cases which corresponds to an increase in total capacitance. This increase, however, is much more apparent in the doped samples (Figures 4.10b - 4.10c) than in the pristine sample. This indicates that OLCs are definitely playing a role in the electrochemcial behaviour of the cell. In particular the need for this activation may arise from the fact that the OLCs are situated in layers of the MXene and might be blocking access for the ions in the electrolyte, thereby corresponding to an intially lower specific capacitance. As an initial electrical signal is applied to them the onions reorient themselves so as to achieve the most energy efficient orientation, i.e. finding the path of least action in an application of the least action principle, which corresponds to the specific capacitance then surpassing that of the pristine material. Melchior et al (2018) observed the intercalation of carbon nanospheres in $Ti_2CT_X$ MXene [19], and since OLCs have, on average, a smaller diameter than carbon nanospheres there is a high possibility that the OLCs have intercalated. This intercalation would lend credence to the possibility that the reorientation of the OLCs in the MXene layers produces the observed change in signal during the activation process.

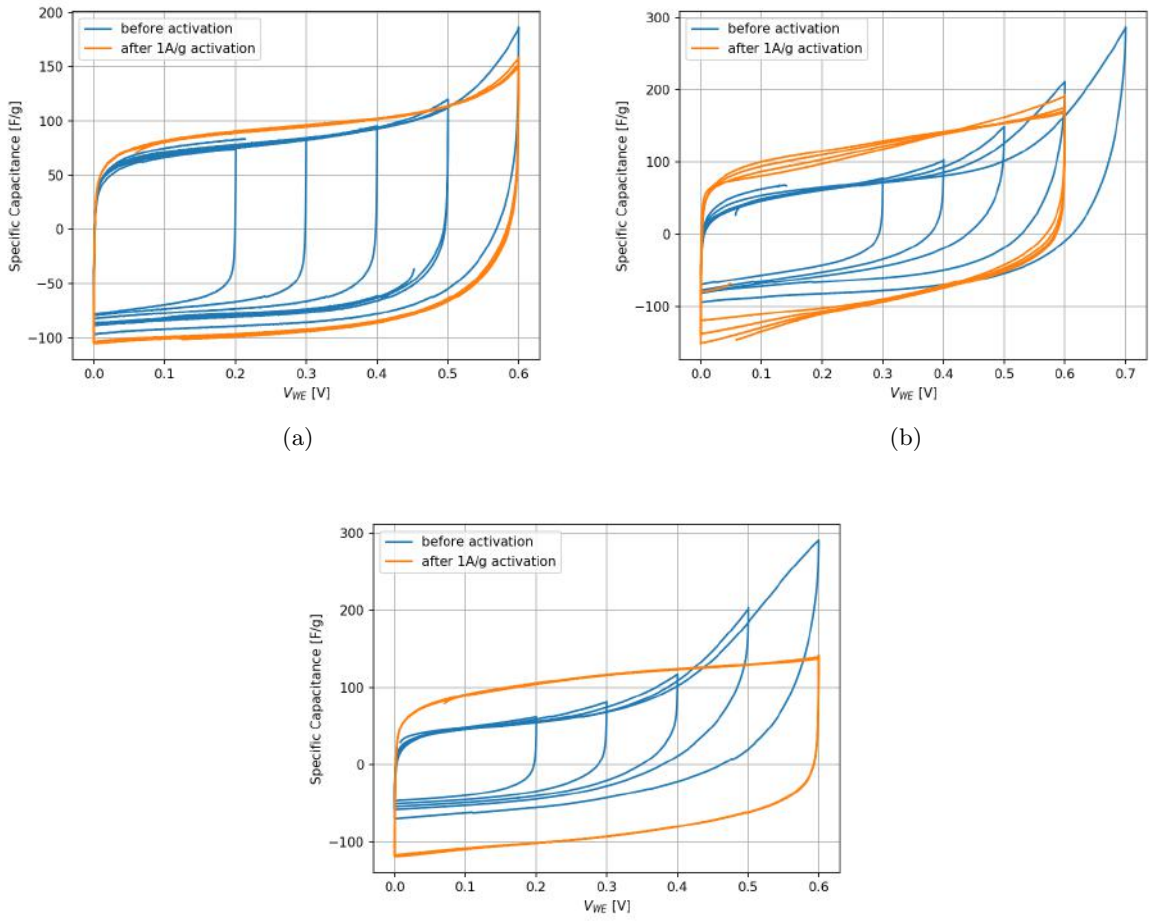


(a)

(b)

(c)

Figure 4.10: CV plots of the first few cycles at 20 mV/s and after cycling at 1 A/g for a few cycles, for the three samples under study; (4.10a) Pristine $Ti_2CT_X$, (4.10b) $Ti_2CT_X$//OLC (5%), and (4.10c) $Ti_2CT_X$//OLC (10%).

### 4.2.2 Potential Window (CV and CD)

Figure 4.11 contains scans of different potential windows using CV (4.11a - 4.11c) and using CD (4.11d - 4.11f). It is clear from all CVs that at 0.7 V a tail starts forming in the voltammogram, which corresponds to the degradation of the electrolyte as it oxidises. From the shapes of the CV plots 0.6 V seems to be the ideal window. In the subsequent CD plots this analysis is reinforced by the symmetric shape of the charge/discharge curves, indicating that there is good coulombic efficiency at the 0.6 V potential window, and that this coulombic efficiency becomes slightly worse at the 0.7 V window for both doped and undoped samples. Thus the doping of OLCs has not had any effect on the potential window of the material.

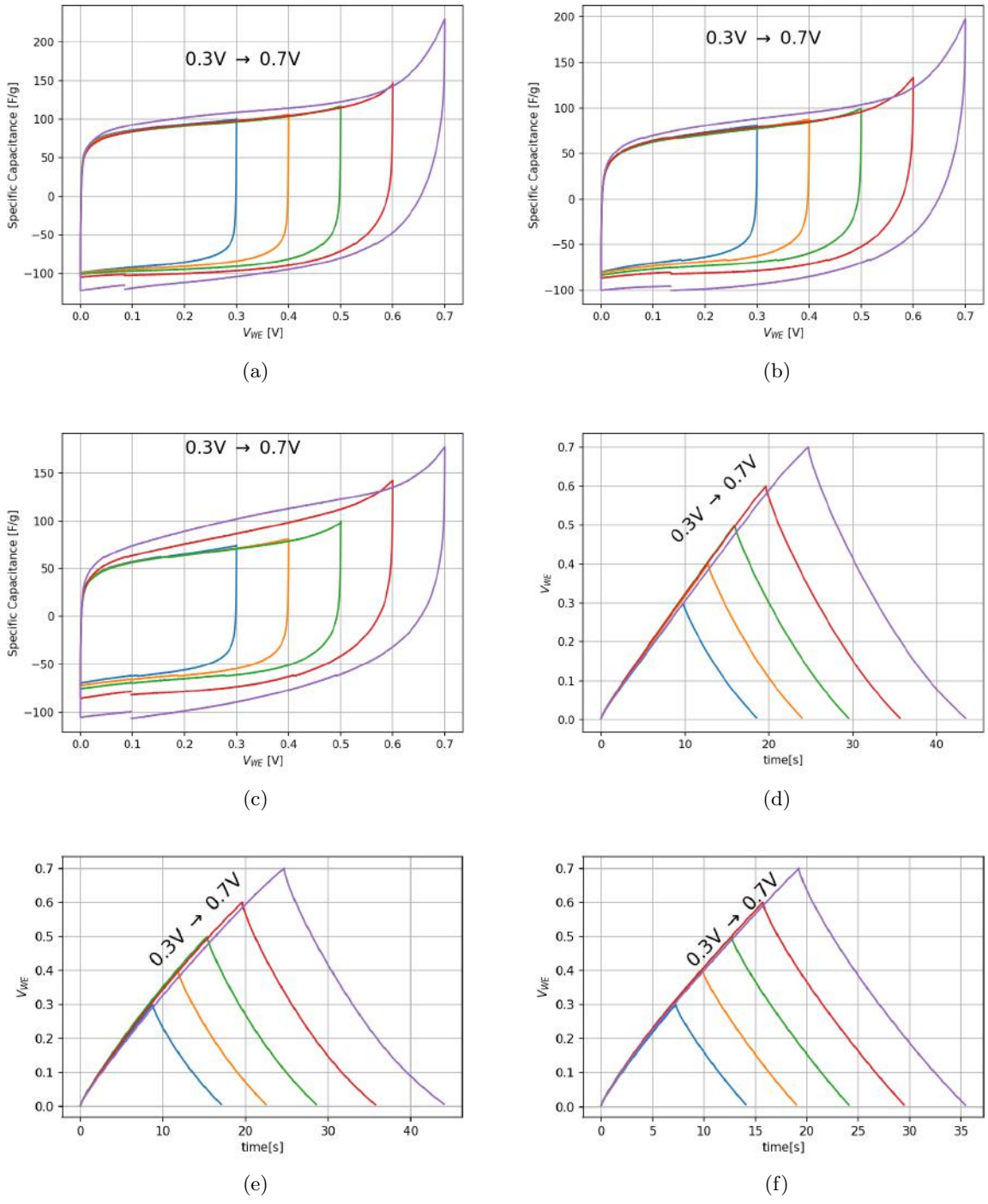


Figure 4.11: Scans of different potential windows using CV (a-c) and using CD (d-f) of different samples under study; (a and d) Pristine $Ti_2CT_X$, (b and e) $Ti_2CT_X$/OLC (5%), and (c and f) $Ti_2CT_X$/OLC (10%).

### 4.2.3 Scan Rates (CV)

Figure 4.12 contains the different scan rates at the 0.6 V potential window for each sample. The shape of the CV is consistent across scan rates 20 mV/s to 200 mV/s, with only a slight decrease in capacitance at the higher scan rates. This indicates that the material, both doped and undoped samples, are quite stable at high scan rates. We can see however, that the area enclosed by the 5% doped sample exhibits a higher overall specific capacitance when compared to the other samples, however, the pristine sample exhibits a higher specific capacitance compared to the 10% doped sample. This difference is highlighted

in Figure 4.12d in which the CVs of each sample are shown at a scan rate of 50 mV/s.

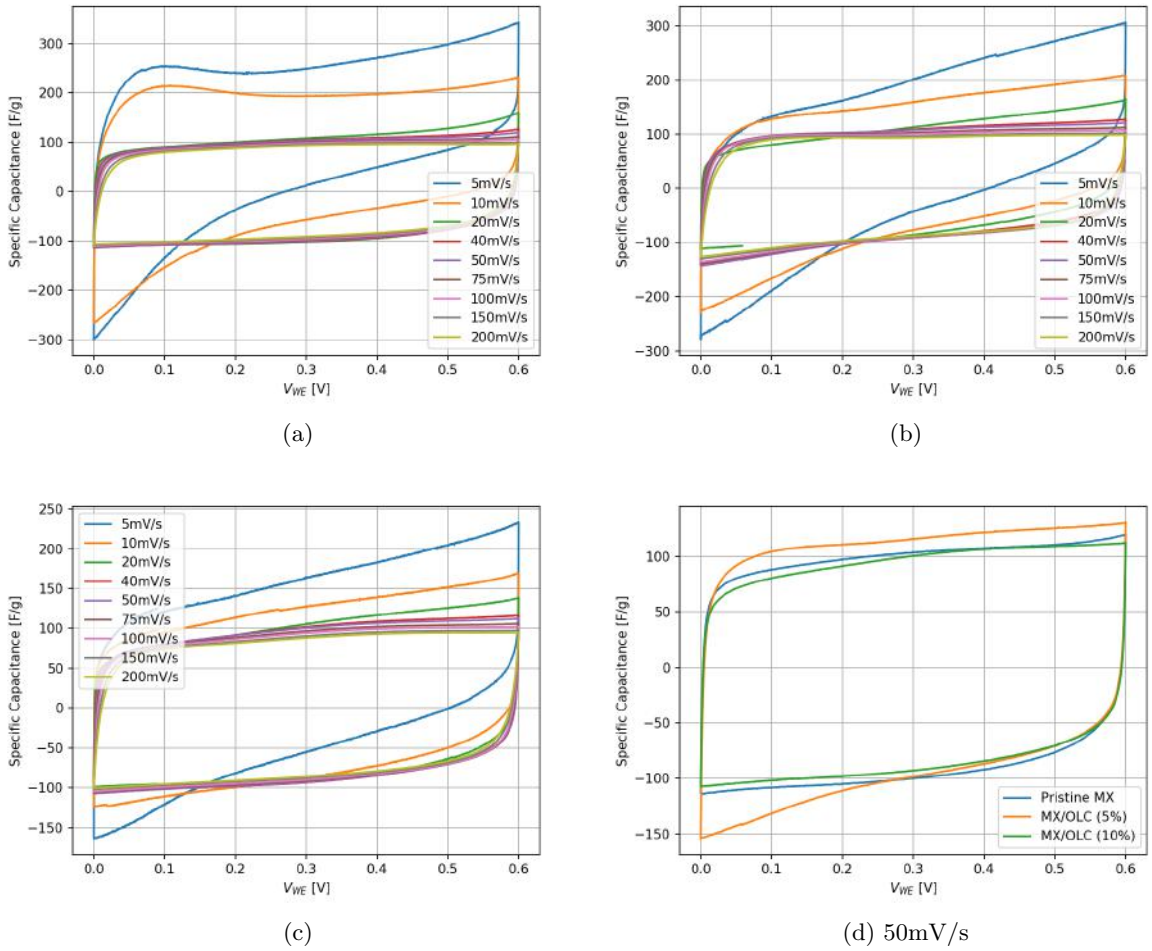


(a) (b)

(c) (d) 50mV/s

Figure 4.12: Different scan rates at the 0.6 V potential window for each sample; (a) Pristine $Ti_2CT_X$, (b) $Ti_2CT)X/OLC$ (5%), (c) $Ti_2CT)X$/OLC (10%), and (d) a comparison of each sample at 50 mV/s.

### 4.2.4 Discharge Curves (CD)

Figure 4.13 contains the CD plots at current densities ranging from 0.25 A/g to 5 A/g for each sample. The charge/discharge curves in all samples are fairly symmetric till 0.5 A/g, with both the pristine and 5% doped sample exhibiting asymmetry at 0.25 A/g, although the 5% sample's CD curve is slightly more symmetric. In contrast, the 10% doped sample is much more symmetric. This implies the possibility that the greater quantity of OLCs has improved the coulombic efficiency at the low current densities. Figure 4.13d shows the comparison of the different specific capacitances calculated from the CD plots using Equation 3.3. From the plot we can see that the 5% doped sample exhibits a specific capacitance which closely mimics the pristine material at high current densities ($\geq$ 3 A/g), however, at lower current densities the 5% doped sample exhibits a much greater specific capacitance, peaking at 147 F/g compared to 106 F/g at 0.25 A/g. The 10% doped sample by contrast exhibits the lowest specific capacitance of around 92 F/g. It should be noted that the error on these measurements were too low to appear in Figure 4.13d.

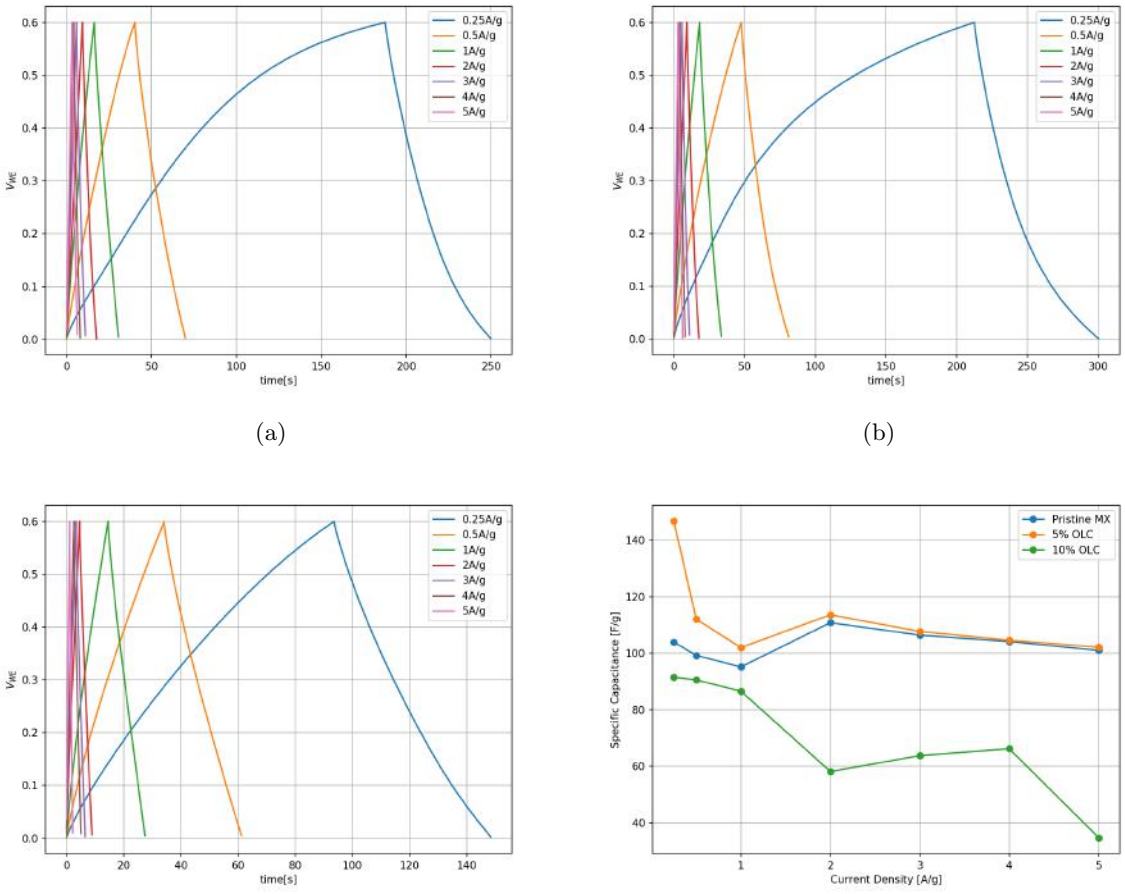


(a) (b)

(c) (d)

Figure 4.13: CD plots at current densities ranging from 0.25 A/g to 5 A/g for each sample; (a) Pristine $Ti_2CT)X$, (b) $Ti_2CT_X/OLC$ (5%), (c) $Ti_2CT_X$/OLC (10%), (d) comparison of specific capacitances vs current density for all samples.

### 4.2.5 Long Term Cycling

Figure 4.14 contains the plots of the efficiency curves, both coulombic efficiency and capacitive retention, for each sample. For the pristine sample in Figure 4.14a we see that coulombic efficiency is stable at 95%, and the capacitive retention decreases to 80% after 10000 cycles. In contrast, the 4% doped sample (Figure 4.14b) shows a capacitive retention of over 100%, which might be because of some more activation that has taken please during the high current cycling. Its coulombic efficiency however, drops from $\sim$ 100% to $\sim$ 90% during some anomolous behaviour at around 9000 cycles. This may be due to the connecting wire reacting with the electrolyte as the electrodes may have come into contact with the sulfuric acid electrolyte during the cell assembly. Figure 4.14c shows that the 8% doped sample behaved consistently with a coulombic efficiency of around 99% and and a capacitive retention of $\geq$ 95%. This indicates that the addition of the OLCs does indeed improve the stability of the material, slightly increasing the coulombic efficiency of the material by 3-4% but vastly increasing the capacitive retention by $\sim$ 20%. The OLCs may in fact be intercalating through the MXene layers and thereby increasing the stability of the layers. This phenomenon has been explored by other authors and the increased stability through this intercalation has been shown to be a valid hypothesis for the MXene $Ti_3C_2T_X$ [23], [36], and so it is not unreasonable to assume a similar effect in the MXene used in this work. A similar analysis was made by Melchior et al (2018) [19].

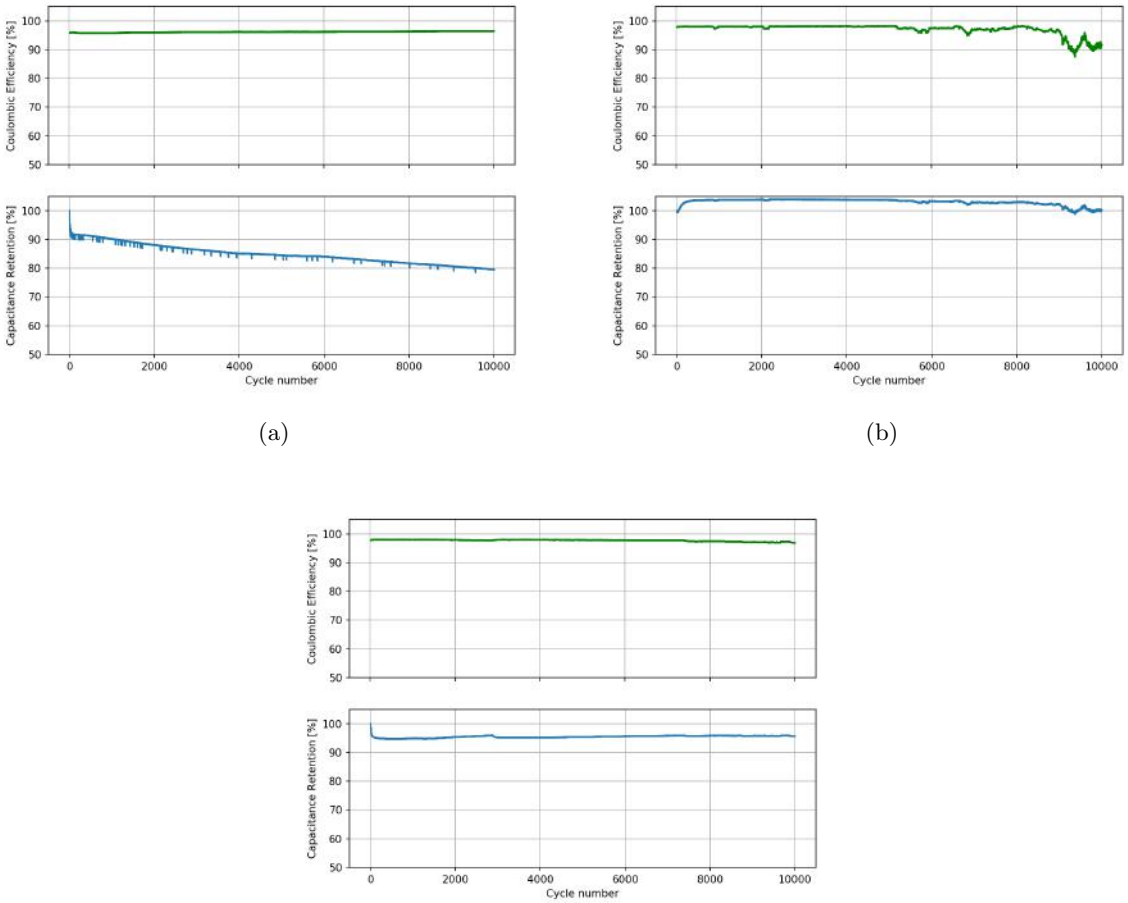


Figure 4.14: Plots of the efficiency curves, both coulombic efficiency and capacitive retention, for each sample: (a) pristine $Ti_2CT_X$, (b) $Ti_2CT_X/OLC$ (5%), (c) $Ti_2CT_X/OLC$ (10%).

### 4.2.6 Impedance Modelling

Figure 4.15 contains the Nyquist plots of each sample before and after long term cycling (10000 cycles) as well as the equivalent series circuit (ESC) uses to fit the data.

The first feature to note from the data in Figure 4.15 is the change in behaviour before and after the cycling. A horizontal skewing in the EIS plot indicates an increased frequency dependance of the real resistance of the cell and thus a decrease in energy storage capability. The pristine MXene sample (Figure 4.15b) shows a significant deviation away from the initial EIS plot. This indicates that the stability pristine MXene has been affected in a non-trivial way. The 5% doped sample (Figure 4.15c) shows a much smaller deviation, and the 10% doped sample (Figure 4.15d) shows no significant deviation. This is in agreement with the anlysis of Figure 4.14 that the addition of OLCs to the active material improves the electrochemical stability of the material, however, it should be noted that the analysis of Figure 4.14 yields more quantifiable data, and that the analyis of Figure 4.15 serves well in reinforcing the data in a more qualitative manner.

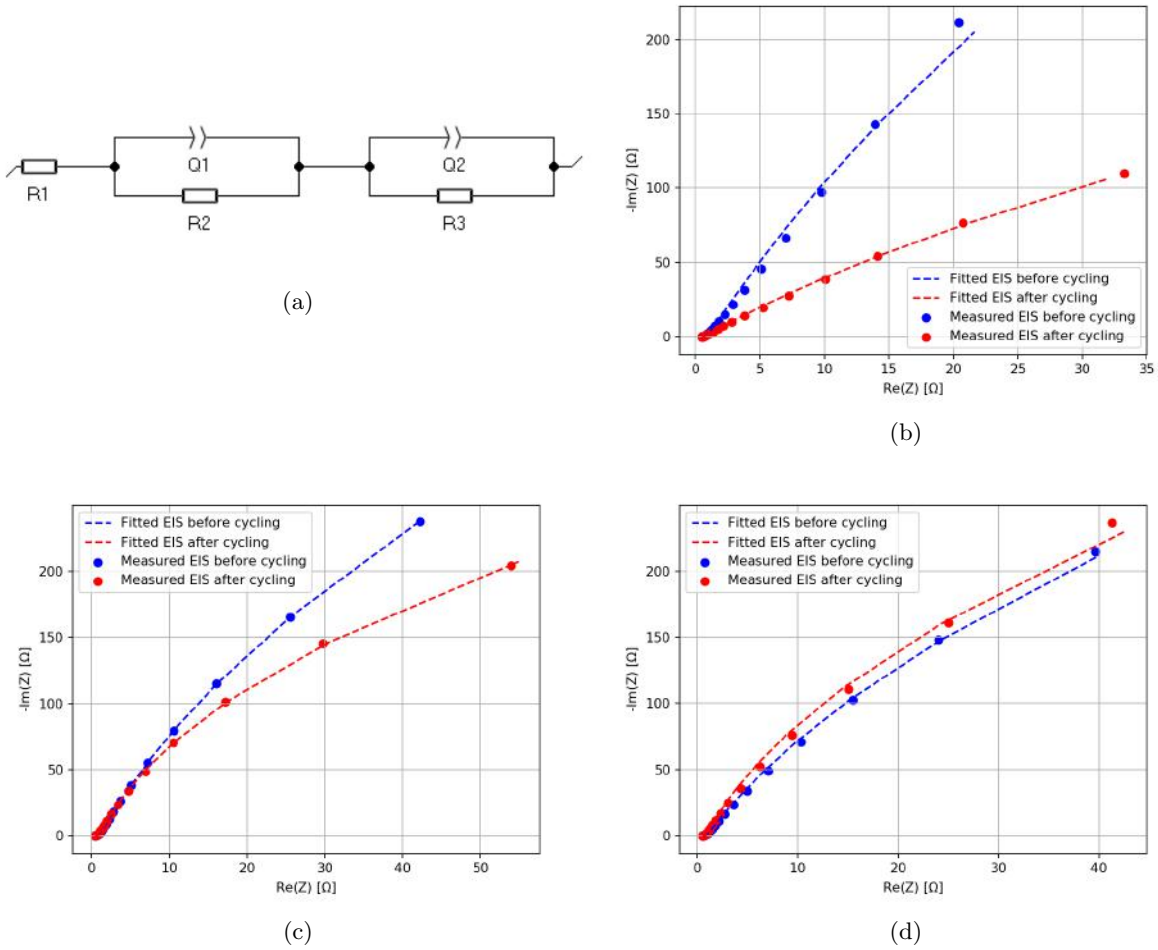


Figure 4.15: Image of the (a) the equivalent series circuit used to fit the EIS data before and after 10000 cycles for (b) Pristine MXene, (c) MX/OLC (5%) and (d) MX/OLC (8%).

The second point of analysis for the EIS plots is a discussion of the ESC. The ESC used in the fitting is shown in Figure 4.15a. The parameters of the fit relate directly to these components and the values of each paramter are located in Tables 4.6 - 4.8. The ESC inlcudes an initial resistor $R_S$ to denote the solution resitance. The solution resistance is synonymous with the equivalent series resistance (ESR) discussed in Chapter 2 and 3. The other components of the ESC include two groups of a constant phase element (CPE) and another resistor in parallel with each other. These represent the charge transfer mechanisms which are active in the supercapacitor, denoted with the subscripts CT1 and CT2. CT2 represents the Electric Double Layer capacitance and the CT1 represents the redox behaviour in the cell. These two mechanisms were discussed in Chapter 1. The CPEs are denoted by $Q$, and the impedance due to a CPE is given in Equation 4.1:

$$Z_{CPE} = \frac{1}{[Q(j2\pi f)^n]} \tag{4.1}$$

where $j$ is the imaginary number $\sqrt{-1}$. Q is a frequency-dependant constant that relates to the electrode-electrolyte interface. $n$ is derived from the slope of $log(Z)$ plotted against $log(f)$ and can exist in the range $-1 \leq n \leq 1$. When $n$ takes a value close to 1, the CPE is equivalent to a capacitor (capacitance in a 'ideal' EDLC, or non-faradiac charge transfer) and when $n$ is close to 0 it resembles a resistor. For a value close to 0.5 the CPE impedance resembles Warburg impedance which represents ion diffusion (pseudocapacitance or faradaic), and when close to -1, it resembles an inductor. The CPE is affected by the following factors [37]:

- the nature of the electrode material (such as porosity, roughness, or polycrystallinity)

- the differences arising from the manner in which the relaxation times are distributed as a result of the heterogeneous nature of the electrode/electrolyte interface
- the fluctuations in the rate of diffusion of ions (i.e. dynamic disorder) at the electrode/electrolyte interface.

A reduced $\chi^2$ value is used to evaluate the goodness of fit for each ESC fit, and all values are less than 0.0005, indicating plausible fits. The parameters for each sample is shown in Tables 4.6 - 4.8. In all three samples the value of $R_S$ is fairly constant before and after cycling at around 0.5Ω. This is sensible since the same set up was used for all samples. The last parameter to note is the value of $n$ in each fit. In the Pristine MXene sample (Table 4.6) the value of $n_1$ decreases from 0.47 to 0.35. This indicates that the first charge transfer mechanism (faradaic) becomes more resitive and therefore more losses occur through this mechanism. The value of $n_2$ decreases from 0.96 to 0.87, indicating that the second transfer mechanism (non-faradaic) also becomes less efficient as it deviates away from unity. In contrast, both doped samples exhibit much more stable $n$ values which do not in fact decrease at all. In fact, these values increase for both doped samples, particlularly for in the case of the $n_1$ values. This indicates that these samples' redox activity improves somewhat through the long term cycling, and could imply that the materials exhibit some further activation during this process.

| **Pristine MXene** | | |
|---|---|---|
| **Parameter** | **Before cycling** | **After cycling** |
| $R_s$ [Ω] | 0.4956 | 0.4768 |
| $Q_{CT1}$ | 0.7303 | 1.423 |
| $n_1$ | 0.4746 | 0.3462 |
| $R_{CT1}$ [Ω] | 0.7388 | 0.1972 |
| $Q_{CT2}$ | 0.0681 | 0.09905 |
| $n_2$ | 0.9554 | 0.8723 |
| $R_{CT2}$ [Ω] | 6938 | 1253 |
| $\chi^2 / \mid Z \mid$ | 2.591e-3 | 3.119e-3 |

Table 4.6: Parameters for the equivalent series circuit fit in Figure 4.15b.

| **MX/OLC (5%)** | | |
|---|---|---|
| **Parameter** | **Before cycling** | **After cycling** |
| $R_s$ [Ω] | 0.5183 | 0.5051 |
| $Q_{CT1}$ | 0.433 | 0.3723 |
| $n_1$ | 0.4557 | 0.5316 |
| $R_{CT1}$ [Ω] | 0.7224 | 0.3975 |
| $Q_{CT2}$ | 0.0556 | 0.06247 |
| $n_2$ | 0.9418 | 0.9428 |
| $R_{CT2}$ [Ω] | 3028 | 1349 |
| $\chi^2 / \mid Z \mid$ | 0.1323e-3 | 0.2018e-3 |

Table 4.7: Parameters for the equivalent series circuit fit in Figure 4.15c.

| **MX/OLC (10%)** | | |
|---|---|---|
| **Parameter** | **Before cycling** | **After cycling** |
| $R_s$ [Ω] | 0.5507 | 0.5403 |
| $Q_{CT1}$ | 0.4486 | 0.3776 |
| $n_1$ | 0.4784 | 0.5467 |
| $R_{CT1}$ [Ω] | 0.5366 | 0.353 |
| $Q_{CT2}$ | 0.0619 | 0.0595 |
| $n_2$ | 0.9397 | 0.9567 |
| $R_{CT2}$ [Ω] | 2453 | 2098 |
| $\chi^2 / \mid Z \mid$ | 0.7268e-3 | 0.1.692e-3 |

Table 4.8: Parameters for the equivalent series circuit fit in Figure 4.15d.

## 4.3 Energy Density, Power Density, and ESR

Figure 4.16 contains all the Ragone plots for samples used in this work. The maximum power and energy density at each current density for each sample is calculated using Equations 3.7 and 3.9. A comparison of Figures 4.16a and 4.16c shows that the highest energy density achieved for the pristine sample was at 2 A/g, but the highest power density was achieved at 0.25 A/g. All samples followed the trend with the highest power density being achieved at 0.25 A/g.

The highest energy density values occur at 2 A/g for the Pristine and 5% doped samples (ignoring the 0.25 A/g reading for the 5% doped sample), and at 0.25 A/g for the 10% doped sample. A possible reason for this seemingly uncorrelated relationship between energy density and current density could be the order in which these measurements were taken. During the discharge measurements the samples were discharged at 1 A/g first, then 0.5 A/g, then 0.25 A/g to test the stability of the samples at low current densities. The samples are then discharged at the higher current densities from 2 A/g to 5 A/g. This could have the unforseen consequence of activating the material with the low current densities which may improve the performance of the material, resulting in better performance of the higher current densities compared to the 1 A/g readings. Lower current densities can create further activation because ions are given sufficient time to intercalate further into the bulk material due to the slower rate of charge transfer.

By looking at Figure 4.16d we can see that the ESR 5% doped sample very closely matches the pristine sample, and is noticeably lower than the pristine sample until 0.25 A/g. This could possibly imply that the addition of the OLCs does not in fact have a significant improvement of the conductivity of the overall material as was hypothesized. In fact, as can be seen in the 10% doped sample, in larger doping quantities the ESR actually increases, implying a less conductive sample. The ESR in Figure 4.16d also closely resembles the fitting parameters for the solution resistance found in the EIS analysis ($\sim 0.5\ \Omega$), showing the ability for different techniques to produce comparable results.

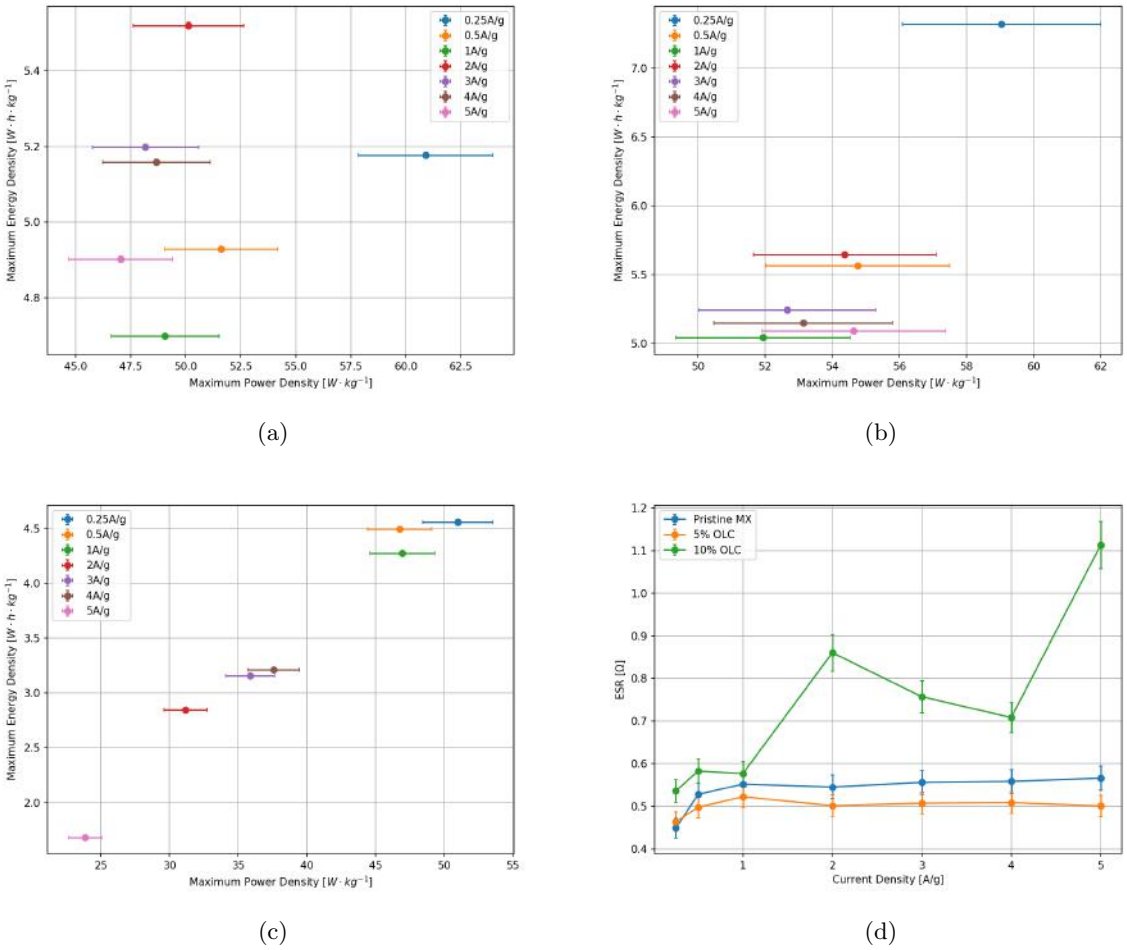


Figure 4.16: Ragone plots comparing the maximum energy and power densities for (a) Pristine MX, (b) 5% doped sample, (c) 10% doped sample, and (d) a plot of the ESR vs current density for all samples.

## 4.4 Evaluation of Key Parameters

As discussed in Chapter 1 the key parameters of interest, and the techniques used to determine them, in this study include the following:

- Specific Capacitance - CD analysis
- Operating Voltage - CV and CD analysis
- Maximum Energy Density - CD and CV analysis
- Maximum Power Density - CD and CV analysis
- Equivalent Series Resistance - EIS analysis
- Time constant - EIS and CD analysis

The values of these parameters are shown in Table 4.9. The specific capacitance vs current density of all samples is found in Figure 4.13d, and the value at 0.25 A/g is shown in Table 4.9. The operating voltage was found to be 0.6 V for all samples from Figure 4.11. The ESR for each sample is determined from the EIS fitting in 4.15 and is shown in Tables 4.6 to 4.8. The time constant $\tau$ is calculated using Equation 1.2, and is shown in Table 4.9. The maximum power and energy density for each sample at 0.25 A/g is calculated using Equations 3.7 and 3.9 and shown in Table 4.9. The errors on $V_0$ are negligible at two significant figures.

| Key Parameter | Pristine MX | MX/OLC (5%) | MX/OLC (10%) |
|---|---|---|---|
| $C_s$ **@ 0.25 A/g [F/g]** | $103.98 \pm 0.16$ | $147.71 \pm 0.24$ | $91.53 \pm 0.14$ |
| $V_0$ **[V]** | 0.60 | 0.60 | 0.60 |
| **ESR @ 0.25 A/g** [$\Omega$] | $0.45 \pm 0.02$ | $0.50 \pm 0.03$ | $0.54 \pm 0.03$ |
| $E_{max}$ **@ 0.25 A/g** [$W \cdot h \cdot kg^{-1}$] | $5.18 \pm 0.01$ | $7.31 \pm 0.01$ | $4.56 \pm 0.01$ |
| $P_{max}$ **@ 0.25 A/g** [$W \cdot kg^{-1}$] | $60.90 \pm 3.04$ | $59.04 \pm 2.95$ | $50.99 \pm 0.21$ |
| $\tau$ | $0.16 \pm 0.02$ | $0.22 \pm 0.03$ | $0.12 \pm 0.03$ |

Table 4.9: A comparison of the key parameters for all samples measured during the course of this study.

## 4.5 Conclusion

It can be concluded that the MXene $Ti_2CT_X$ was succesfully synthesized via etching its precursor material; the MAX phase $Ti_2AlC$. This success of the synthesis was evident in the XRD and Raman Spectroscopy measurements; by seeing the appearance and disappearance of typical key features. The synthesis precedure utilised twice the etching time in HF (formed in situ using LiF and HCl) and this is thought to have ripped up sheets of the MXene. The XRD results showed shoulder peaks where one stand alone peak was expected, indicating that many stacking faults had occurred in the macrostructure of the material instead of the expected regular interlayer distances. This was further reinforced by SEM and TEM results which showed the occurence of many spots of material sitting on, around, and in between the MXene sheets in the pristine MXene sample. Due to the excessive care taken to reduce the chances of contaminants as well as the thorough washing the MXene was given it is likely that these spots are in fact ripped up MXene sheets.

The extended etching time (96 hours as opposed to 48 hours) used to synthesize the pristine MXene, as well as using the LiF + HCl synthesis method, may have been the reason which resulted in its improvement in gravimetric capacitance (104 F/g in this work) compared to the literature for the same material at similar mass loadings ($\sim$ 75 F/g at 0.25 A/g [19], $\sim$ 35 F/g at 0.25 A/g [24]). This improvement was measured using a combination of CV and CD measurements.

OLCs were successfully intercalated into the MXene compound in two different quanitites; 5% and 10% weight percentages. The success of the intercalation was confirmed primarily by using Raman Spectroscopy and XPS measurements. The integration of the OLCs into the MXene compound has been seen to significantly increase the electrochemical stability of the material. This was measured by looking at the capacitive retention after 10000 cycles and is quantified as an approximate 20% increase in stability for both 5% and 10% doped samples. This analysis was qualitatively reinforced using EIS results taken before and after the long term cycling process.

The OLCs were also seen to increase the specific capacitance, measured using CD and CV, of the material when intercalated in small amounts (5%) from 104 F/g to 148 F/g, a 42% increase. OLCs were also seen to decrease the specific capacitance when intercalated in larger amounts (10%) from 104 F/g to 92 F/g (Table 4.9). This is likely due to a compromise between an increase in total surface area of the material due to the addition of high surface area particles (the OLCs) and the very same particles blocking layers and thereby blocking access to active sites which lie deeper in the MXene compound. According to the EIS results the OLCs did not increase the overall conductivity of the compound, but they did facilitate greater faradic charge transfer in the material. This was seen during the fitting of the EIS results, where the redox charge transfer process was obsevred to have a lower resistance in the OLC doped samples.

The 5% OLC doped sample obtained a higher power density and energy density than the pristine sample, and the pristine sample obtaining a higher power and energy density than the 10% OLC doped sample, likely for the same reasons mentioned above. It should be noted that the pristine sample did achieve a slighly higher power density at 0.25 A/g, however, at higher current densities the 5% OLC doped sample exhibits a lower ESR (Figure 4.16d), and therefore a higher power density, as a comparison between Figures 4.16a and 4.16b reveals. However, these measurements are not truly representative as these measurements are usually normalised using the weight of the full supercapacitor device. This study focused solely on the materials themselves, and not the performance of the supercapacitor device, which would include the mass of the plating and the separators.

Overall, it can be conlcuded that the electrochemical performance of the MXene $Ti_2CT_X$ was improved through the integration of OLCs (in small quantities) into the MXene compound, and this was primarily

observed through:

- increase in specific capacitance
- increase in electrochemical stability
- greater facilitation of faradic charge transfer

Future studies may want to investigate the effect of greater OLC quantities on the potential window of the MXene compound, as well the effect of different cell configurations on the results obtained from the material's performance. In particular it would be interesting to see how using precious metals to conduct the signals in the T-type cell would affect the results obtained. Another item worth studying would be the effect of mixed electrolytes, for example, $H_2SO_4$ mixed with the $LiSO_4$, on the performance of a MXene based supercapacitor.

# Bibliography


[1] Wikipedia. Samsung Galaxy S series. https://en.wikipedia.org/wiki/Samsung_Galaxy_S_series, 2014.

[2] Martin Winter and Ralph J. Brodd. What are batteries, fuel cells, and supercapacitors? *Chemical Reviews*, 104(10):4245–4269, 2004.

[3] Sanliang Zhang and Ning Pan. Supercapacitors Performance Evaluation. pages 1–19, 2014.

[4] George Z. Chen. Understanding supercapacitors based on nano-hybrid materials with interfacial conjugation. *Progress in Natural Science: Materials International*, 23(3):245–255, 2013.

[5] Allen J Bard, Larry R Faulkner, Elizabeth Swain, and Charity Robey. *Fundamentals and Applications*.

[6] David C. Grahame. The electrical double layer and the theory of electrocapillarity. *Chemical Reviews*, 41(3):441–501, 1947.

[7] John. Kenneth McDonough. Onion-like Carbon for Electrochemical Capacitors. (June), 2014.

[8] B. E. Conway and W. G. Pell. Double-layer and pseudocapacitance types of electrochemical capacitors and their applications to the development of hybrid devices. *Journal of Solid State Electrochemistry*, 7(9):637–644, 2003.

[9] Faxing Wang, Xiongwei Wu, Xinhai Yuan, Zaichun Liu, Yi Zhang, Lijun Fu, Yusong Zhu, Qingming Zhou, Yuping Wu, and Wei Huang. Latest advances in supercapacitors: From new electrode materials to novel device designs. *Chemical Society Reviews*, 46(22):6816–6854, 2017.

[10] Marco Zeiger, Nicolas Jäckel, Vadym N. Mochalin, and Volker Presser. Review: Carbon onions for electrochemical energy storage. *Journal of Materials Chemistry A*, 4(9):3172–3196, 2016.

[11] Michael Naguib, Murat Kurtoglu, Volker Presser, Jun Lu, Junjie Niu, Min Heon, Lars Hultman, Yury Gogotsi, and Michel W. Barsoum. Two-dimensional nanocrystals produced by exfoliation of Ti3AlC2. *Advanced Materials*, 23(37):4248–4253, 2011.

[12] M. Naguib, Vadym N Mochalin, Michel W. Barsoum, and Yury Gogotsi. MXenes: A new family of 2D materials. *Advanced Materials*, 26:992–1004, 2014.

[13] M Amoretti, C Amsler, G Bonomi, A Bouchta, P Bowe, C Carraro, C L Cesar, M Charlton, M J T Collier, M Doser, V Filippini, K S Fine, A Fontana, M C Fujiwara, R Funakoshi, P Genova, J S Hangst, R S Hayano, M H Holzscheiter, L V Jørgensen, V Lagomarsino, R Landua, D Lindelöf, E Lodi Rizzini, M Macrì, N Madsen, G Manuzio, M Marchesotti, P Montagna, H Pruys, C Regenfus, P Riedler, J Rochet, A Rotondi, G Rouleau, G Testera, A Variola, T L Watson, and D P van der Werf. Production and detection of cold antihydrogen atoms. *Nature*, 419:456, sep 2002.

[14] Michael Ghidiu, Maria R. Lukatskaya, Meng Qiang Zhao, Yury Gogotsi, and Michel W. Barsoum. Conductive two-dimensional titanium carbide 'clay' with high volumetric capacitance. *Nature*, 516(7529):78–81, 2015.

[15] Babak Anasori, Maria R. Lukatskaya, and Yury Gogotsi. 2D metal carbides and nitrides (MXenes) for energy storage. *Nature Reviews Materials*, 2(2), 2017.

[16] Volker Presser, Michael Naguib, Laurent Chaput, Atsushi Togo, Gilles Hug, and Michel W. Barsoum. First-order Raman scattering of the MAX phases: Ti2AlN, Ti2AlC0.5N0.5, Ti2AlC,

(Ti0.5V0.5)2AlC, V2AlC, Ti3AlC2, and Ti3GeC2. *Journal of Raman Spectroscopy*, 43(1):168–172, 2012.

[17] Shen Lai, Jaeho Jeon, Sung Kyu Jang, Jiao Xu, Young Jin Choi, Jin Hong Park, Euyheon Hwang, and Sungjoo Lee. Surface group modification and carrier transport properties of layered transition metal carbides (Ti2CTx, T: -OH, -F and -O). *Nanoscale*, 7(46):19390–19396, 2015.

[18] Fanfan Liu, Aiguo Zhou, Jinfeng Chen, Heng Zhang, Jianliang Cao, Libo Wang, and Qianku Hu. Preparation and methane adsorption of two-dimensional carbide Ti2C. *Adsorption*, 22(7):915–922, 2016.

[19] Sharona A. Melchior, Kumar Raju, Innocent S. Ike, Rudolph M. Erasmus, Guy Kabongo, Iakovos Sigalas, Sunny E. Iyuke, and Kenneth I. Ozoemena. High-Voltage Symmetric Supercapacitor Based on 2D Titanium Carbide (MXene, Ti 2 CT x )/Carbon Nanosphere Composites in a Neutral Aqueous Electrolyte. *Journal of The Electrochemical Society*, 165(3):A501–A511, 2018.

[20] Peichao Lian, Yanfeng Dong, Zhong-Shuai Wu, Shuanghao Zheng, Xiaohui Wang, Sen Wang, Chenglin Sun, Jieqiong Qin, Xiaoyu Shi, and Xinhe Bao. Alkalized Ti 3 C 2[1] Lian P, Dong Y, Wu Z-S, et al. Alkalized Ti 3 C 2 MXene nanoribbons with expanded interlayer spacing for high-capacity sodium and potassium ion batteries. Nano Energy 2017;40:1–8. MXene nanoribbons with expanded interlayer spacing fo. *Nano Energy*, 40(July):1–8, 2017.

[21] Maria R Lukatskaya, Olha Mashtalir, Chang E Ren, Yohan Dall Agnese, Michel W Barsoum, and Yury Gogotsi. Cation Intercalation and High Volumetric Capacitance of Two-Dimensional Titanium Carbide. *Science*, 341(6153):1502–1505, 2013.

[22] Maria R. Lukatskaya, Seong Min Bak, Xiqian Yu, Xiao Qing Yang, Michel W. Barsoum, and Yury Gogotsi. Probing the Mechanism of High Capacitance in 2D Titanium Carbide Using in Situ X-Ray Absorption Spectroscopy. *Advanced Energy Materials*, 5(15):2–5, 2015.

[23] Zheng Ling, Chang E. Ren, Meng-Qiang Zhao, Jian Yang, James M. Giammarco, Jieshan Qiu, Michel W. Barsoum, and Yury Gogotsi. Flexible and conductive MXene films and nanocomposites with high capacitance. *Proceedings of the National Academy of Sciences*, 111(47):16676–16681, 2014.

[24] Raghavan Baby Rakhi, Bilal Ahmed, Dalaver Anjum, and Husam N. Alshareef. Direct Chemical Synthesis of MnO2Nanowhiskers on Transition-Metal Carbide Surfaces for Supercapacitor Applications. *ACS Applied Materials and Interfaces*, 8(29):18806–18814, 2016.

[25] Meryl D. Stoller and Rodney S. Ruoff. Best practice methods for determining an electrode material's performance for ultracapacitors. *Energy and Environmental Science*, 3(9):1294–1301, 2010.

[26] J. K. McDonough and Yury Gogotsi. Carbon Onions: Synthesis and Electrochemical Applications. *Interface magazine*, 22(3):61–66, 2013.

[27] Samuel David Littlejohn. *Electrical Properties of Graphite Nanoparticles in Silicone*. 2014.

[28] David Pech, Magali Brunet, Hugo Durou, Peihua Huang, Vadym Mochalin, Yury Gogotsi, Pierre Louis Taberna, and Patrice Simon. Ultrahigh-power micrometre-sized supercapacitors based on onion-like carbon. *Nature Nanotechnology*, 5(9):651–654, 2010.

[29] Meng Qiang Zhao, Chang E. Ren, Zheng Ling, Maria R. Lukatskaya, Chuanfang Zhang, Katherine L. Van Aken, Michel W. Barsoum, and Yury Gogotsi. Flexible MXene/carbon nanotube composite paper with high volumetric capacitance. *Advanced Materials*, 27(2):339–345, 2015.

[30] Darrell Henry, Nelson Eby, John Goodge, and David Mogk. X-ray reflection in accordance with Bragg's Law. https://serc.carleton.edu/research_education/geochemsheets/BraggsLaw.html.

[31] Oren D. Leaffer, Surojit Gupta, Michal W. Barsoum, and Jonathan E. Spanier. On Raman scattering from selected M2AC compounds. *Journal of Materials Research*, 22(10):2651–2654, 2007.

[32] Susan Swapp. Scanning Electron Microscopy (SEM). https://serc.carleton.edu/research_education/geochemsheets/te

[33] Stephen Brunauer, P H Emmett, and Edward Teller. Adsorption of Gases in Multimolecular Layers. *Journal of the American Chemical Society*, 60(2):309–319, feb 1938.

[34] S. A. Shah, T. Habib, H. Gao, P. Gao, W. Sun, M. J. Green, and M. Radovic. Template-free 3D titanium carbide (Ti3C2Tx) MXene particles crumpled by capillary forces. *Chemical Communications*, 53(2):400–403, 2017.

[35] Wentian Gu, Nicholas Peters, and Gleb Yushin. Functionalized carbon onions, detonation nanodiamond and mesoporous carbon as cathodes in Li-ion electrochemical energy storage devices. *Carbon*, 53:292–301, 2013.

[36] Jianmin Luo, Wenkui Zhang, Huadong Yuan, Chengbin Jin, Liyuan Zhang, Hui Huang, Chu Liang, Yang Xia, Jun Zhang, Yongping Gan, and Xinyong Tao. Pillared Structure Design of MXene with Ultralarge Interlayer Spacing for High-Performance Lithium-Ion Capacitors. *ACS Nano*, 11(3):2459–2469, 2017.

[37] Andrzej Lasia. Electrochemical impedance spectroscopy and its applications. *Electrochemical Impedance Spectroscopy and its Applications*, 9781461489:177–195, 2014.